Design and Advanced Manufacturing of Bio-inspired Optimal Microstructures using Machine Learning Method

Dissertation
der Mathematisch-Naturwissenschaftlichen Fakultät
der Eberhard Karls Universität Tübingen
zur Erlangung des Grades eines
Doktors der Naturwissenschaften
(Dr. rer. nat.)

vorgelegt von
M.Sc. Cem Balda DAYAN
aus Istanbul, Türkei

Tübingen 2023

Gedruckt mit Genehmigung der Mathematisch-Naturwissenschaftlichen Fakultät der Eberhard Karls Universität Tübingen.

Tag der mündlichen Qualifikation: 13.06.2023

Dekan:	Prof. Dr. Thilo Stehle
1. Berichterstatter:	Prof. Dr. Metin Sitti
2. Berichterstatter:	Prof. Dr. Martin Giese

“Our true mentor in life is science.”

- Mustafa Kemal Atatürk

To my family

Acknowledgments

Firstly, I would like to thank and express my gratitude to my supervisor, Professor Metin Sitti, for accepting me to work in the Physical Intelligence Department at the Max Planck Institute for Intelligent Systems and for his helpful guidance, support, and valuable advice through my doctoral study in all sense. It was a great experience and pleasure for me to work with a pioneer scientist, professor, and director in this field. I have been impressed by his curiosity about new subjects, enthusiasm for science, ambition, and broad knowledge of many different topics. Additionally, I would like to thank Professor Martin Giese for his insightful suggestions, for evaluating my thesis, and especially for helping and supporting me with university procedures.

I would like to thank International Max Planck Research School for Intelligent Systems (IMPRS-IS) for supporting me during my Ph.D. study. I especially

would like to thank Leila Masri, Sara Sorce, and all IMPRS-IS members for their support in all sense during my study. Also, I want to thank Max Planck Society for its funding support.

I would like to thank my group members, especially Dirk-Michael Drotlef, Ville Liimatainen, Donghoon Son, Amirreza Aghakhani, Dongha Tahk, Sungwoo Chun, Muhammad Yunusa, Anastasia Koivikko for our discussions and their great help. Also, I want to thank my external collaborators Christopher T. Mitchell and Professor Alyssa Y. Stark from Villanova University in the USA for our excellent collaboration with successful results.

This study would not be possible without working with enjoyable and supportive people around me. I want to thank Nihal Olcay Dogan for her endless support during my study. I would like to thank Eylul Suadiye, Gul Dogan, Cansu Kursun, Pelin Erkoc Erik, Sinan Ozgun Demir, Musab Cagri Ugurlu, Saadet Baltaci, and Mehmet Efe Tiryaki. I

shared my memorable moments with all of them, including very cheerful and very sad ones. Also, I appreciated them being my second family during my Ph.D. and never leaving me alone.

I would sincerely like to thank Patricia Martinez, Janina Schwartz, Eugenia Komnik, Nagaraj Krishna-Subbaiah, Anitha Shiva, Devin Sheehan, Jack Saud, Martina Schneider, Anna-Maria Wild, Yan Yu, Jelena Zinnanti, Gerd Hoerner, Maritta Dudek for their administrative and technical support.

I would like to thank the rest of my group members in alphabetic order with their last names, Mukrime Birgul Akolpoglu, Yunus Alapan, Asli Aydin, Xianqiang Bao, Aarushi Bhargava, Ugur Bozuyuk, Junghwan Byun, Hakan Ceylan, Pouria Esmaeili-Dokht, Zeynep Izlen Erenoglu, Wei Feng, Gaurav Gardi, Chantal Goethler, Jie Han, Mertcan Han, Siyeon Jang, Wenbin Kang, Selin Kanyas, Alp Can Karacakol, Selcan Karaz, Muhammad Turab Ali Khan, Dong Wook Kim, Hyun Gyu Kim, Jongkuk Ko,

Yunwoo Lee, Mingtong Li, Jiahe Liao, Zemin Liu, Xianglong Lyu, Nima Mahkam, Rut Martinez Miras, Barbara Nessiem, Aniket Pal, Abdon Pena-Francesch, Martin Phelan, Ziyu Ren, Aybike Reyhanli, Ren Hao Soon, Varun Sridhar, Savas Tasoglu, Zhikai Tu, Halim Ugurlu, Chunxiang Wang, Fan Wang, Tianlu Wang, Paul Wrede, Yingdan Wu, Yingbo Yan, Oncay Yasa, Immihan Ceren Yasa, Berk Yigit, Erdost Yildiz, Hongchuan Zhang, Jianhua Zhang, Mingchao Zhang, Rongjing Zhang, Zhiqiang Zheng.

I would like to express my gratitude with all my heart to my mom; Nuray Dayan, and my dad; Levent Dayan, for their endless and unconditional support, endless love, and encouragement throughout my whole life. Besides being my parents, they are also my best friends.

Cem Balda DAYAN
Stuttgart, Germany

Abstract

Bioinspired fibrillar structures have been promising for various disruptive adhesive applications. Especially micro/nanofibrillar structures on gecko toes can have strong and controllable adhesion and friction on a wide range of surfaces with residual-free, repeatable, self-cleaning, and other unique features. Also, in some environmental conditions (*e.g.*, relative humidity, temperature), their adhesion performance increases according to literature[1,2]. These findings can be integrated to design high-performance synthetic structural adhesives such as composite-based synthetic gecko-inspired adhesives. Additionally, there are some debates and theories about the reason for the increase of gecko adhesion in different environmental conditions. The related theories can be examined by studying them systematically. This investigation requires live geckos' and gecko-inspired synthetic adhesives' performance comparison in various environmental conditions. These findings can explore why

adhesion increases and helps to design high-performance synthetic structural adhesives. Moreover, gecko-inspired synthetic adhesives' adhesion performance highly depends on their fabrication method. Due to fabrication limitations, the desired complex fibril designs sometimes cannot be fabricated. Advanced fabrication techniques can be integrated to minimize fabrication limitations and fabricate the desired designs almost freely. As a result, a two-photon-lithography-based three-dimensional printing technique can be used with an elastomeric material to manufacture more advanced free-body design fibrils. After all these findings, we can try to explore the outperformance of optimal designs for gecko-inspired synthetic adhesives. Previously, synthetic dry fibrillar adhesives inspired by such biological fibrils have been optimized in different approaches to increase their performance. Previous fibril designs for shear optimization are limited by pre-defined standard shapes in a narrow range primarily based on human intuition, which restricts their maximum performance. In this aspect,

we can combine the Bayesian optimization and finite-element-method-based shear mechanics simulations to find shear-optimized fibril designs automatically. In addition, fabrication limitations can be integrated into the simulations to have more experimentally relevant results. The computationally discovered shear-optimized structures are fabricated, experimentally validated, and compared with the simulations. Both experimental and simulation results show that the shear-optimized fibrils perform better than the pre-defined standard fibril designs. This design optimization method can be used in future real-world shear-based gripping or non-slip surface applications, such as robotic pick-and-place grippers, climbing robots, gloves, electronic devices, and medical and wearable devices.

Zusammenfassung

Bioinspirierte fibrilläre Strukturen sind vielversprechend für verschiedene disruptive Klebstoffanwendungen. Insbesondere mikro-/nanofibrilläre Strukturen auf Geckozehen können eine starke und kontrollierbare Haftung und Reibung auf einer Vielzahl von Oberflächen mit rückstandsfreien, wiederholbaren, selbstreinigenden und anderen einzigartigen Eigenschaften aufweisen. Außerdem erhöht sich laut Literatur[1,2] unter bestimmten Umgebungsbedingungen (z. B. relative Luftfeuchtigkeit, Temperatur) ihre Haftfähigkeit. Diese Erkenntnisse können in die Entwicklung leistungsstarker synthetischer Strukturklebstoffe einfließen, wie z. B. synthetische Klebstoffe auf Verbundstoffbasis, die von Geckos inspiriert sind. Darüber hinaus gibt es einige Debatten und Theorien über den Grund für den Anstieg der Gecko-Haftung unter verschiedenen Umweltbedingungen. Die entsprechenden Theorien können durch

systemische Studien untersucht werden. Diese Studien erfordern einen Leistungsvergleich zwischen den Eigenschaften von lebenden Geckos und von Geckos inspirierten synthetischen Klebstoffen unter verschiedenen Umweltbedingungen. Diese Erkenntnisse können erforschen, warum die Adhäsion zunimmt und dazu beitragen, leistungsstarke synthetische Strukturklebstoffe zu entwickeln. Darüber hinaus hängt die Adhäsionsleistung von durch Geckos inspirierten synthetischen Klebstoffen stark von ihrer Herstellungsmethode ab. Aufgrund von Herstellungsbeschränkungen können die gewünschten komplexen Fibrillendesigns manchmal nicht hergestellt fabriziert werden. Die Herstellungsbeschränkungen können durch die Integration fortschrittlicher Fertigungstechniken minimiert werden und so zu einer nahezu freien Wahl des gewünschten Herstellungsdesigns führen. So kann eine auf Zwei-Photonen-Lithographie basierende dreidimensionale Drucktechnik mit einem elastomeren Material verwendet werden, um

fortschrittlichere Fibrillen im Freikörperdesign herzustellen. Basierend auf diesen Erkenntnissen können wir versuchen, optimale Designs für Gecko-inspirierte synthetische Klebstoffe zu erforschen. Bisher wurden fibilläre Klebstoffe, die von solchen biologischen Fibrillen inspiriert sind und synthetische, feste Eigenschaften aufweisen, mit verschiedenen Ansätzen optimiert, um ihre Leistung zu erhöhen. Bisherige Fibrillendesigns für die Scheroptimierung sind durch vordefinierte Standardformen in einem engen Bereich begrenzt, der hauptsächlich auf menschlicher Intuition beruht, was ihre maximale Leistung einschränkt. In diesem Zusammenhang können wir die Bayes'sche Optimierung und auf der Finite-Elemente-Methode basierende Schermechaniksimulationen kombinieren, um automatisch scheroptimierte Fibrillendesigns zu finden. Darüber hinaus können Herstellungsbeschränkungen in die Simulationen integriert werden, um experimentell relevantere Ergebnisse zu erhalten. Die ermittelten scheroptimierten Strukturen werden hergestellt,

experimentell validiert und mit den Simulationen verglichen. Sowohl die experimentellen als auch die Simulationsergebnisse zeigen, dass die scheroptimierten Fibrillen besser funktionieren als die vordefinierten Standardfibrillen. Diese Design-Optimierungsmethode kann in zukünftigen realen Anwendungen für scherbasiertes Greifen oder rutschfeste Oberflächen eingesetzt werden, wie z. B. bei robotischen Greifarmen, Kletterrobotern, Handschuhen, elektronischen Geräten sowie medizinischen und tragbaren Geräten.

Table of Contents

Acknowledgments ..... **i**

Abstract ..... **v**

Zusammenfassung ..... **ix**

Table of Contents ..... **xiii**

List of Figures ..... **xvii**

List of Symbols ..... **xxi**

List of Abbreviations ..... **xxiii**

1 List of Publications **1**

1.1 Manuscripts Ready for Submission and Relevant to This Thesis 1

1.2 Accepted Publications Relevant to This Thesis 1

1.3 Other Publications Not Relevant to This Thesis 2

1.4 Scientific Contributions 5

2 Introduction **7**

2.1 Gecko-inspired Synthetic Adhesives and Gecko-inspired Synthetic Composite Adhesives 10

2.2 Live Gecko and Gecko-inspired Synthetic Adhesives' Shear Adhesion under Different Environmental Conditions 11

2.3 Three-dimensional (3D) Printing of Elastomeric Bioinspired Complex Adhesive Microstructures 14

2.4 Machine Learning-based and Experimentally Validated Shear Optimal Fibril Adhesives 15

3 Motivation and Main Findings 21

4 Results and Discussion 25

4.1 Gecko-inspired Synthetic Adhesives and Gecko-inspired Synthetic Composite Adhesives 27

4.2 Live Gecko and Gecko-inspired Synthetic Adhesives' Shear Adhesion under Different Environmental Conditions 39

4.3 3D Printing of Elastomeric Bioinspired Complex Adhesive Microstructures 46

4.4 Machine Learning-based and Experimentally Validated Shear Optimal Fibril Adhesives 49

Appendix A. Bio-inspired Composite Microfibers for Strong and Reversible Adhesion on Smooth Surfaces 71

Appendix B. The Effect of Substrate Wettability and Modulus on Gecko and Gecko-inspired Synthetic Adhesion in Variable Temperature and Humidity 81

Appendix C. 3D Printing of Elastomeric Bioinspired Complex Adhesive Microstructures 99

Appendix D. Machine Learning-based and Experimentally Validated Shear Optimal Fibril Adhesives 123

References 141

List of Figures

Figure 4.1. The fabrication process of the GSA (VS mushroom) 29

Figure 4.2. The fabrication process of the gecko-inspired synthetic composite adhesives 31

Figure 4.3. Normal adhesion measurements of microfibers with various tip geometries and the mushroom composite microfibrillar adhesives..... 33

Figure 4.4. The height profiles and repeatability performances of mushroom composite microfibrillar adhesives. 36

Figure 4.5. Smooth and rough contact surface normal adhesion performance of DP-composite mushroom and a flat control. 38

Figure 4.6. Tokay gecko and gecko-inspired synthetic adhesive shear adhesion in variable relative humidity on hydrophilic and hydrophobic glass. 42

Figure 4.7. Tokay gecko and gecko-inspired synthetic adhesive shear adhesion in variable relative humidity and temperature. 45

Figure 4.8. Direct 3D printing-based approach for fabricating elastomeric bioinspired complex adhesives. 46

Figure 4.9. The SEM images of the fabricated elastomeric bioinspired complex adhesives. 48

Figure 4.10. Overall summary for investigating the Bayesian optimization-based shear-optimized microfibril designs..... 49

Figure 4.11. The fabrication procedure and an example SEM image of the optimal fibrils. 52

Figure 4.12. Normal stress distribution under different shear strains for an 80 µm tip diameter and AR 0.4 ML-found optimal design. 62

Figure 4.13. Shear stress distribution under different shear strains for an 80 µm tip diameter and AR 0.4 ML-found optimal design. 64

Figure 4.14. SEM images of the fabricated ML-found optimal elastomeric fibril structures for different tip diameters and ARs. 66

Figure 4.15. Shear adhesion results in FEM simulations and experiments for a single fibril using standard shapes (flat punch, wedge-shaped mushroom) and ML-based shear optimal designs. 69

List of Symbols

ºC	Degree Celsius
nm	Nanometer
µm	Micrometer
mm	Millimeter
N	Newton
mN	Milinewton
MPa	Megapascal
kPa	Kilopascal
R_a	Arithmetical Average Roughness
R_z	Mean Peak-to-valley Roughness
h	Hours
min	Minutes
s	Seconds

List of Abbreviations

2D	Two-dimensional
2PP	Two-photon-polymerization
3D	Three-dimensional
AR	Aspect Ratio
BO	Bayesian Optimization
DP	Double-printed
FEM	Finite Element Method
GP	Gaussian Process
GSA	Gecko-inspired Synthetic Adhesive
IPA	Isopropyl Alcohol
ML	Machine Learning
NA	Numerical Aperture
OTS-SAM	Octadecyl Trichloro Silane Self-assembled Monolayer
PDMS	Poly Di Methyl Siloxane
RH	Relative Humidity
RT	Room Temperature
SEM	Scanning Electron Microscope
Si	Silicon

S-PSA	Silicone-based Pressure Sensitive Adhesive
SP	Single-printed
VS	Vinyl Siloxane

1 List of Publications

1.1 Manuscripts Ready for Submission and Relevant to This Thesis

1. **Cem Balda Dayan,** Donghoon Son, Amirreza Aghakhani, Yingdan Wu, Sinan Ozgun Demir, and Metin Sitti, Machine learning-based and experimentally validated shear optimal fibril adhesives. ***unpublished***, 2023.

1.2 Accepted Publications Relevant to This Thesis

2. **Cem Balda Dayan**[*], Sungwoo Chun[*], Nagaraj Krishna-Subbaiah, Dirk-Michael Drotlef, Mukrime Birgul Akolpoglu, and Metin Sitti, 3D printing of elastomeric bioinspired complex adhesive microstructures. ***Advanced Materials***, 2021, doi: 10.1002/adma.202103826.

[*] Equally contributing co-first authors

3. Christopher T. Mitchell*, **Cem Balda Dayan***, Dirk-Michael Drotlef, Metin Sitti, and Alyssa Y. Stark, The effect of substrate wettability and modulus on gecko and gecko-inspired synthetic adhesion in variable temperature and humidity. ***Scientific Reports***, 2020, doi: 10.1038/s41598-020-76484-6.

4. Dirk-Michael Drotlef, **Cem Balda Dayan**, and Metin Sitti, Bio-inspired composite microfibers for strong and reversible adhesion on smooth surfaces. ***Integrative and Comparative Biology***, 2019, doi: 10.1093/icb/icz009.

1.3 Other Publications Not Relevant to This Thesis

5. Mehmet Efe Tiryaki, Fatih Dogangun, **Cem Balda Dayan**, Paul Wrede, and Metin Sitti, MRI-powered magnetic miniature capsule robot with HIFU-controlled on-demanding drug delivery. ***International Conference on Robotics and Automation (ICRA)***, 2023.

* Equally contributing co-first authors

6. Gul Dogan, Sinan Ozgun Demir, Rico Gutzler, Herbert Gruhn, **Cem Balda Dayan**, Umut Tuncay Sanli, Christian Silber, Utku Culha, Metin Sitti, Gisela Schutz, Corinne Grevent, and Kahraman Keskinbora, Bayesian machine learning for efficient minimization of defects in ALD passivation layers. ***ACS Applied Materials & Interfaces***, 2021, doi: 10.1021/acsami.1c14586.

7. Anastasia Koivikko, Dirk-Michael Drotlef, **Cem Balda Dayan**, Veikko Sariola, and Metin Sitti, 3D-Printed pneumatically controlled soft suction cups for gripping fragile, small, and rough objects. ***Advanced Intelligent Systems***, 2021, doi: 10.1002/aisy.202100034.

8. Julia Kröger, Alberto Jiménez-Solano, Gökcen Savasci, Petra Rovó, Igor Moudrakovski, Kathrin Küster, Hendrik Schlomberg, Hugo A. Vignolo-González, Viola Duppel, Lars Grunenberg, **Cem Balda Dayan**, Metin Sitti, Filip Podjaski, Christian Ochsenfeld, and Bettina V. Lotsch, Interfacial engineering for improved photocatalysis in a charge storing 2D carbon nitride: melamine functionalized poly(heptazine imide). ***Advanced Energy Materials***, 2021, doi: 10.1002/aenm.202003016.

9. Ajay Vikram Singh*, Mohammad Hasan Dad Ansari*, **Cem Balda Dayan**, Joshua Giltinan, Shuo Wang, Yan Yu, Vimal Kishore, Peter Laux, Andreas Luch, and Metin Sitti, Multifunctional magnetic hairbot for untethered osteogenesis, ultrasound contrast imaging and drug delivery. ***Biomaterials***, 2019, doi: 10.1016/j.biomaterials.2019.119394.

* Equally contributing co-first authors

1.4 Scientific Contributions

This work enables the development of high-performance gecko-inspired synthetic adhesives (GSAs) by combining a machine learning (ML) method, advanced manufacturing technique, and inspirations from nature. All these findings allow us to understand how GSAs' performance can be improved. The results will be helpful for real-world gripping or non-slip surface applications, such as robotic pick-and-place grippers[3], climbing robots[4], gloves[5], electronic devices[6], and medical and wearable devices[7].

Chapter 2 presents the mentioned subjects and issues individually, from initial problems and approaches to finding solutions. Moreover, four scientific publications are merged as the motivation of this study in Chapter 3. The findings and results are presented and discussed in Chapter 4, providing a broad understanding of high-performance GSAs by combining bioinspired approaches with advanced

manufacturing methods, as well as getting help from ML-based techniques.

2 Introduction

Several species in nature (*e.g.*, geckos, tree frogs, octopuses, and ants) can stick diverse surfaces with the intrinsic micro/nanostructures found in their bodies. Among them, geckos have hairy structures on their toes to adhere to various surfaces. These hairy adhesive structures have some branches and hierarchical patterns called *setae*. The setae have highly complex fibril geometries, including spatula- and mushroom-shaped tip endings[8]. The adhesion mechanism of geckos is based on intermolecular interactions, such as van der Waals forces[9,10]. As a result, gecko adhesion is highly repeatable and controllable without remaining any residual on the contact surface after detachment[11]. Such fibrillary adhesives are also studied for self-cleaning[12–15], contact mechanics[16,17], liquid repellency[18,19], friction[20–22], and adhesion[23] under different environmental conditions. These benefits have influenced many studies to fabricate synthetic bioinspired fibrillary adhesives for various

applications[18,20,24]. In some circumstances, synthetic adhesives performed even better than their biological peers on smooth surfaces[25,26].

Previous studies reported different designs for high-performance normal or shear adhesion. Due to that, they used various kinds of designs, including gecko-inspired angled[20], composite[25], and hierarchical[24] structural shape adhesives. In addition, live gecko's adhesion increases in some environmental conditions, and getting inspiration from these findings, composite adhesives have been developed[1,2], and to achieve high-performance GSAs, the development of composite adhesives is significantly crucial.

The live geckos' adhesion increases in specific environments. The adhesion increase of live geckos tried to be explained by two theories in the literature; material softening and capillary forces. Both theories should be examined systematically to understand

their contributions to live geckos' and GSAs' adhesion.

GSA fabrication is mainly depending on molding techniques. The molding-based fabrication limitations highly affect GSAs' shape complexity and performance. To overcome these limitations, advanced fabrication methods can be integrated to fabricate elastomeric complex GSAs with high performances.

Moreover, all these investigations should be combined to obtain high-performance shear-optimal GSAs. For doing that, an ML method can also be integrated for such exploration to find the optimal structure.

Considering all, the rest of this chapter is organized as follows. This thesis's content is research on the designing and advanced manufacturing of bio-inspired shear-optimal microstructures using an ML method. The GSA and

gecko-inspired synthetic composite adhesives for normal adhesion are discussed in Section 2.1. After that, live gecko and GSA shear adhesion performances are explored under different temperatures and relative humidities (RHs) in Section 2.2. Then, an advanced fabrication method for elastomeric complex adhesive microstructures is discussed in Section 2.3. Finally, all these findings, knowledge, and explorations are combined to find ML-based and experimentally validated shear-optimal fibril adhesives in Section 2.4.

2.1 Gecko-inspired Synthetic Adhesives and Gecko-inspired Synthetic Composite Adhesives

In the literature, some studies reported that setae soften in some environmental conditions (*e.g.*, relative humidity (RH)), which can improve Geckos' adhesion performance[1,2]. Getting inspiration from these findings, some researchers developed

composite microfibers with a continuous soft layer on the top of their tips (film-terminated fibers)[27], hard fiber core and soft shell[28], and microfibers with stiff fibers and soft tips[29,30]. Additionally, direct crosslinking of composite microfibers decorated with viscous tips on various surfaces can enhance adhesion[7]. However, reversible adhesion performance is still challenging in the literature for gecko-inspired synthetic composite adhesives.

2.2 Live Gecko and Gecko-inspired Synthetic Adhesives' Shear Adhesion under Different Environmental Conditions

Despite significant interest in the morphology, evolutionary history, and biomechanical principles of the gecko adhesive system, there is still uncertainty about the principal mechanism of gecko adhesion. Specifically, the potential roles of capillary adhesion and material softening on gecko adhesive performance in humid environments have often

been debated[1,2,31–33]. The habitat diversity of geckos suggests that geckos must maintain adhesion in various conditions, including hot and humid tropical environments[34–38]; thus, understanding the exact adhesive mechanism of geckos is highly essential.

Although a van der Waals-based adhesive system creates a robust and reversible adhesive force, common environmental factors may disrupt the functionality of the geckos' adhesion. For example, thin water layers can reduce van der Waals forces to zero when separating the setae of the geckos from a substrate by as little as 20 nm[39]. In addition, geckos' adhesion increases in rising RH conditions[1,31–33,40]. Two hypotheses have been proposed to explain the geckos' adhesion in increased RH environments: capillary adhesion and material softening. Gecko adhesion increases as the substrate becomes more hydrophilic, supporting the capillary adhesion hypothesis that capillary bridges between gecko setae and the water-attracting

substrate enhance adhesion[31–33]. Likewise, at high RH (> 70% RH), the setal material (primarily keratin-associated proteins and lipids[41–44]) softens, supporting the material softening hypothesis that soft setae increase the interfacial contact area and subsequently increase van der Waals forces[1,2]. The results of these studies are challenging to comprimise[40,45,46], and no one considers the possibility that both capillary adhesion and material softening can affect geckos' adhesion.

In addition to fluctuations in RH, other environmental factors may also alter gecko adhesive performance. Specifically, at low temperature (12 °C), gecko adhesion increases with increasing RH[40], supporting results from separated setae tested at room temperature[1,31]. However, at high temperature (32 °C), RH does not affect live gecko adhesion[40]. Nanoscale models attempted to explain the temperature effect on geckos' adhesion, but ultimately the coupled impacts of RH and

temperature on geckos' adhesion are still uninvestigated[46].

2.3 Three-dimensional (3D) Printing of Elastomeric Bioinspired Complex Adhesive Microstructures

Bioinspired elastomeric structural adhesives can provide reversible and controllable adhesion on dry/wet and synthetic/biological surfaces for a broad range of commercial applications. However, the previously proposed fabrication techniques, such as molding, limit the shape complexity and performance of the structural adhesives. More sophisticated and complex designs should be used to increase the performance of the current GSAs. However, molding techniques are mainly used for current structural adhesive fabrication, and consideration of the demolding process is the main reason that limits the shape of the developed structures and the capabilities of GSA structures.

Changing the manufacturing method with an advanced fabrication process will significantly improve the complexities and capabilities of the current GSAs. That way, combining multiple bio-inspirations with various functionalities and fabricating complex designs will be possible.

2.4 Machine Learning-based and Experimentally Validated Shear Optimal Fibril Adhesives

Many studies have investigated bioinspired non-directional vertical fibrillar adhesives with various geometries and materials[8]. Most studies have focused on maximizing the adhesion of these synthetic fibrillar adhesives using both analytical and advanced computational methods as a function of fiber stem and tip ending shape, fiber placement in an array, spacing, and material properties. Mushroom/wedge-shaped[47], T-shaped[48–50], and 3D-designed[51,52] fibrils have shown the most enhanced adhesion. However, no one has

investigated these fibrils regarding maximized shear properties using advanced computational methods. During shear, mushroom-shaped fibrils bend after a certain critical point and carry normal and shear stress on the tip of the fibril's circumference, and, as a result, the actual contact area decreases. It causes a reduction in shear force. Therefore, to obtain high shear properties, the fibril structures should initially have high contact area and adhesion with the contact surface[53]. Thus, the 3D shape of the fibril stem and tip ending needs to be optimized for obtaining maximum shear.

ML methods have been implemented in many different fields for optimizing the 3D design of structures in buildings[54], ships[55], aircraft[56], antennae[57], and materials[58,59]. Their computational power outperforms the conventional optimization methods and allows complicated problems to be improved[59]. In various application areas, ML methods effectively use the existing data to test new parameters that may produce novel results[59].

There are many examples of applying ML to optimize certain parameters. Most of these optimizations used neural networks or genetic algorithms. However, some approaches have significant disadvantages in requiring an extensive training data set with more computational time (e.g., genetic algorithm). There are more time-/data-effective alternatives for ML-based design optimization, such as Bayesian optimization (BO). The BO method employs a probabilistic model such as Gaussian processes (GPs) for representing an unknown function[60]. In that function's parameter space, this representation is updated sequentially by suggesting and testing new data points[61,62].

Configuration of BO can be changed between exploration of the unknown regions in the parameter space of the target function and concentration on a specified region of interest in the case of optimization tasks. In that sense, BO has a significant advantage compared to other optimization tools that require pre-defined models of the target processes. Finding

a solution with a few data points, needing a probabilistic model, and requiring a global optimization method makes the BO an effective alternative for optimization challenges[59].

Additionally, as shown in previous studies, ML can be implemented in fibril adhesive designs to maximize their adhesion[51,52]. However, no one has yet investigated shear-optimal 3D fibril designs using ML approaches.

Besides that, previous studies used pre-defined limited fibril shapes to investigate their shear performance. However, a more general and flexible approach is needed to reduce these limitations, which can be achieved by integrating free-body designs into our explorations for finding optimal fibril shapes with higher shear performances. Therefore, we propose an ML-based optimization method with finite element method (FEM)-based shear modeling to optimize the shear performance of 3D fibril designs. The 3D fibril designs are fabricated using

the two-photon-polymerization (2PP) technique to experimentally validate the results, where 2PP enables the manufacturing of free-body fibrils easier than previous fabrication methods. This method provides the advantage of searching a vast design space relatively faster than trial-error and other optimization methods[63]. In addition, the implemented BO framework is highly data-efficient, and the optimization framework requires 300 iteration runs for each design to find the optimal fibril design.

To conclude, the Bezier-curve-based free-body-shape computational modeling gives high flexibility for investigating the optimal fibril design compared to standard pre-defined shapes. In each iteration, the shear results can be estimated with the FEM simulations, and the Bayesian optimizer can suggest the most feasible and optimal fibril design according to the FEM-based shear estimated results. The proposed framework can save reasonable time during shear-optimal fibril design

investigation. Finally, the optimal fibril shapes can be fabricated with 2PP and experimentally validated.

3 Motivation and Main Findings

This chapter mentions motivation and open areas, including the papers I have authored and introduced in Chapter 2. These articles are accessible in Appendices A, B, C, and D.

For investigating high-performance GSAs, a fibril design should be based on free designs instead of pre-defined shapes to eliminate structural limitations. Additionally, the investigation method should be a global optimization method to explore all possible solutions and should not be only optimal for a specific range. Also, FEM simulation can be integrated by considering experimental limitations and parameters to estimate the performance of the microstructures.

To obtain that, first, the high-performance GSAs should be tried to be developed by inspiration from nature (*e.g.*, geckos' adhesion increases in some environmental conditions), such as gecko-

inspired composite adhesive microstructures. Moreover, geckos' and GSAs' adhesion performance should be compared and explored to understand the effects of possible theories. These findings will help to understand the development of high-performance GSAs and furthermore, to realize the possible influential theories behind these approaches.

After understanding the fundamentals, for designing and fabricating the free-body shear-optimal fibrils (not only restricted by pre-defined shapes), the fibril body can be defined by a Bezier curve with a controllable and flexible design simultaneously. As a fabrication method, advanced manufacturing techniques, such as 2PP, can be implemented to eliminate or decrease the fabrication-based limitations that highly affect and determine the fibrils' performance and design flexibility. Then, an ML method can be implemented for these investigations to explore the shear-optimal fibril designs effectively. The BO, an ML technique,

can be implemented as an efficient optimization method to investigate the desired shear-optimal structures for high performance. Additionally, FEM simulation can be integrated for estimating the shear performances of the generated fibril designs. Finally, all these findings are experimentally validated and compared with the well-known standard shapes in the literature.

4 Results and Discussion

In this chapter, the papers I have authored have been summarized and discussed in terms of motivation, methodology, and findings. These published papers are available in Appendices A, B, C, and D.

GSA (Vinyl Siloxane (VS) mushroom) and gecko-inspired synthetic composite adhesives' fabrication methods, normal adhesion performance including a comparison between different tip designs, and adhesion comparison between smooth and rough contact surfaces are introduced and discussed in Section 4.1.

Live gecko and GSA shear adhesion comparison under different environmental conditions are introduced and discussed in Section 4.2.

An advanced fabrication technique is proposed for adhesive microstructures. This technique

enables fabricating of complex adhesive microstructures with almost no fabrication limitations. It is based on a 3D printing technique called 2PP and uses a custom-made elastomeric resin material. These are proposed and discussed in Section 4.3.

Lastly, all these investigations, explorations, and advanced fabrication techniques have been combined to find ML-based shear optimal fibril adhesives. The found optimal structures have been compared with standard designs, and the results have been experimentally validated. These are introduced and discussed in Section 4.4.

4.1 Gecko-inspired Synthetic Adhesives and Gecko-inspired Synthetic Composite Adhesives

This section is based on paper 4 in Chapter 1, *Bio-inspired composite microfibers for strong and reversible adhesion on smooth surfaces*.

For obtaining reversible and strong normal adhesion by gecko-inspired synthetic composite adhesives, microfibrillar patterns were composed of polydimethylsiloxane (PDMS) fibers decorated with VS mushroom-shaped tips, which were additionally coated with a highly soft and thin terminal layer of silicone-based pressure sensitive adhesive (S-PSA).

For PDMS micropillar fabrication, they were produced by replicating SU-8 lithographic template. Sylgard 184 prepolymer and curing agent were mixed with a weight ratio of 10:1, then degassed and cast on the SU-8 mold. The prepared samples were

cured in a vacuum oven at 90 ºC for 1 hour and then demolded (Figure 4.1, Steps i–iv).

For VS mushroom (GSA) fabrication, a thin and homogeneous layer of the VS precursor solution with 25–30 µm thickness was coated over a glass plate by a film applicator. After partial crosslinking of the VS layer for 30–45 seconds, the prepared PDMS micropillars were manually inked onto the thin layer and placed on a perfluorinated silicon wafer. Within a few minutes, the viscous VS was crosslinked, peeled off, and mushroom-shaped microfibers were obtained (Figure 4.1, Steps v–vii).

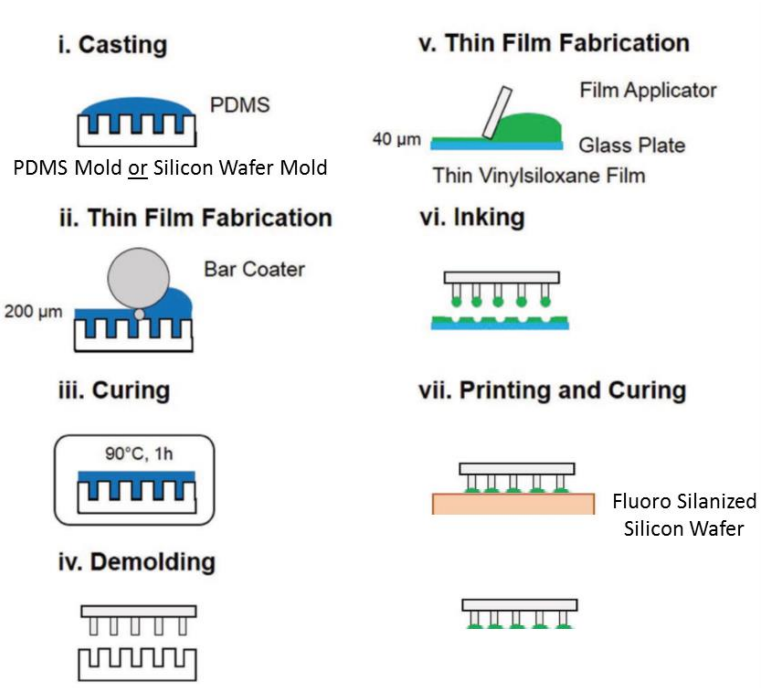

Figure 4.1. The fabrication process of the GSA (VS mushroom); fabrication of the PDMS microfiber film (Steps i–iv), inking and printing of microfibrillar patterns onto a silicon wafer (Steps v–vii), curing, and peeling-off (Step vii). This figure is modified from the literature [7].

The fabrication of gecko-inspired synthetic composite adhesives was based on soft molding techniques. The S-PSA precursor solution was cast on glass, and then desired homogeneous film thickness (~25-30 μm) was achieved by a film applicator (Figure 4.2, Step 1). The S-PSA layer was partially crosslinked for 15-20 minutes (Figure 4.2, Step 2), then the PDMS microfibers with VS mushroom-shaped tips (GSA) were manually inked onto the thin layer of S-PSA (Figure 4.2, Step 3).

For single-printed (SP) gecko-inspired synthetic composite adhesive mushroom fibers, VS mushroom structures coated with S-PSA were printed onto a perfluorinated silicon wafer and cured at room temperature for 12 hours (Figure 4.2, Step 6). Then, the SP gecko-inspired synthetic composite adhesive mushroom fibers were peeled off (Figure 4.2, Step 7).

For double-printed (DP) gecko-inspired synthetic composite adhesive mushroom fibers, VS

mushroom structures coated with S-PSA were printed onto a perfluorinated silicon wafer for 5 seconds (Figure 4.2, Step 4), peeled-off (Figure 4.2, Step 5), and printed on a pristine perfluorinated silicon wafer. The S-PSA was cured at room temperature for 12 hours (Figure 4.2, Step 6). Then, the DP gecko-inspired synthetic composite adhesive mushroom fibers were peeled off (Figure 4.2, Step 7).

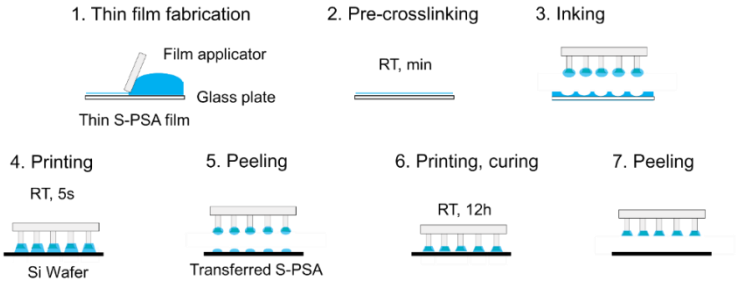

Figure 4.2. The fabrication process of the gecko-inspired synthetic composite adhesives; fabrication and pre-curing of the thin S-PSA film (Steps 1–2), inking and printing of microfibrillar patterns onto a silicon wafer (Steps 3–4), second printing process (double printed) on a pristine wafer, curing, and peeling (Steps 6–7).

To understand the effect of tip geometry on normal adhesion, PDMS micropillars with S-PSA decorated different tip shapes (spherical, mushroom, and film-terminated) were fabricated, including SP and DP gecko-inspired composite mushroom structures. Overall, DP gecko-inspired composite mushroom structures gave the highest normal adhesion compared to all other designs (Figure 4.3). The soft S-PSA layer was better supported by the stiffer mushroom tip (VS-included mushroom tip) than only S-PSA included tip designs (with no VS mushroom tip). This feature allowed homogenous fiber tips, helped keep the fibril's tip shape, and resulted in high normal adhesion performance.

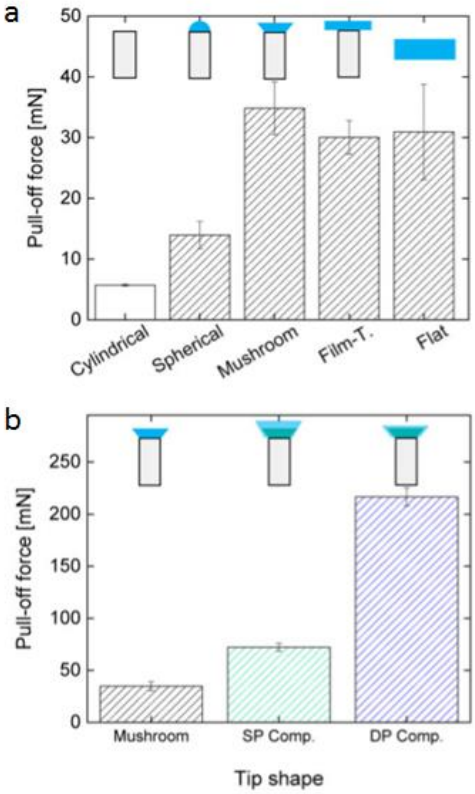

Figure 4.3. Normal adhesion measurements of microfibers with various tip geometries and the mushroom composite microfibrillar adhesives. a) Pull-off force of microfibers with different tip geometries and a flat S-PSA control, measured on a smooth substrate. b) Pull-off force of microfibers with S-PSA mushroom tips and SP and DP composite mushroom patterns, measured on a smooth substrate.

Compared to SP composite mushroom structures, DP composite mushroom structures had a thinner S-PSA layer on the fiber by removing the excess S-PSA layer during fabrication (Figure 4.4a). This property of the DP composite mushroom structures gave them high tip-shape stability and durability (Figure 4.3b, 4.4b). Additionally, on scanning electron microscope (SEM) images, DP composite mushroom structures had higher wedge angles (which means better tip sharpness) than SP composite mushroom structures. As a result, DP composite mushroom fibers had higher normal adhesion than SP composite mushroom fibers. This result agrees with the experimental and theoretical findings in the literature. The soft layer thickness affects normal adhesion performance[28,29,64].

The durability of DP and SP composite mushroom fibers was analyzed with cyclic normal adhesion experiments. DP composite mushroom fibers perform robust and high normal adhesion (Figure 4.4b). Rough surface adhesion experiments

were performed for DP composite mushroom fibrils and flat control, where the rough surface profile was measured with 3D laser scanning microscopy (Figure 4.5a). The results indicated that DP composite mushroom fibers perform better on rough surfaces than flat control (Figure 4.5b).

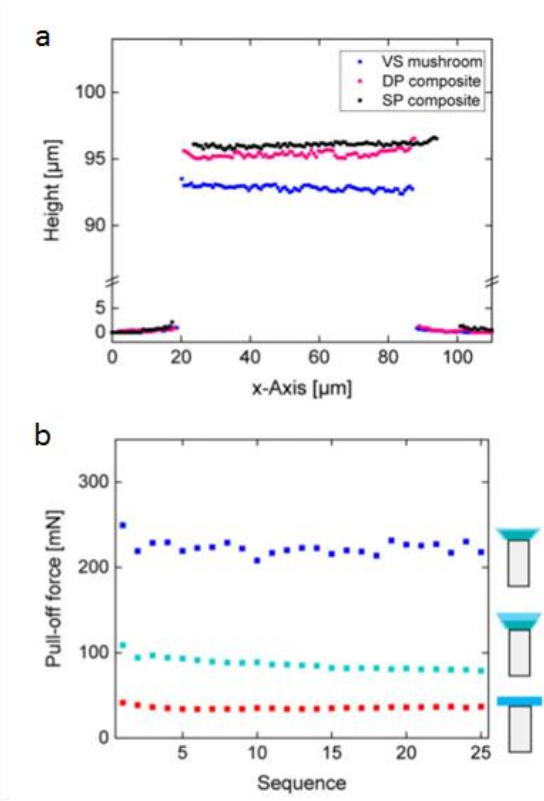

Figure 4.4. The height profiles and repeatability performances of mushroom composite microfibrillar adhesives. a) 3D laser-scanning microscope height profiles of mushroom patterns before (VS mushroom), after the SP or the DP process. b) Pull-off force of SP and DP composite mushroom fibers in a durability test over 25 adhesion cycles, compared with film-terminated microfibers.

These findings showed that the mushroom tips coated with S-PSA layers could enhance normal adhesion with optimal shape and improved load sharing. The high adhesive strength was reached after tailoring the tip geometry, tip composition, top layer thickness, and tip edge sharpness.

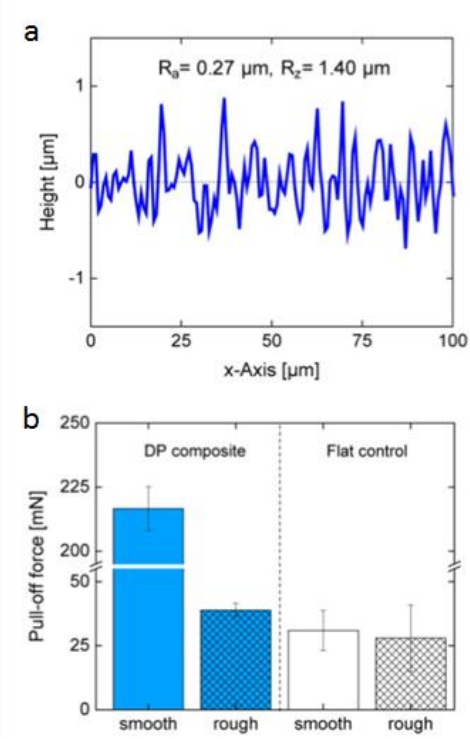

Figure 4.5. Smooth and rough contact surface normal adhesion performance of DP-composite mushroom and a flat control. a) Surface profile of the rough probe employed for adhesion characterizations with an arithmetical mean deviation (R_a) of 0,27 µm and mean peak-to-valley roughness (R_z) of 1.4 µm, obtained by 3D laser scanning microscopy. b) Pull-off force of DP composite fibers measured on smooth and rough surfaces, compared with a flat S-PSA control.

4.2 Live Gecko and Gecko-inspired Synthetic Adhesives' Shear Adhesion under Different Environmental Conditions

This section is based on paper 3 in Chapter 1, *The effect of substrate wettability and modulus on gecko and gecko-inspired synthetic adhesion in variable temperature and humidity*.

After previous investigations, live *Tokay geckos* (*Gekko geckos*) and GSAs were used to compare their shear adhesion performances and understand the roles of the two theories: capillary adhesion and material softening effects on gecko adhesive performance under various environmental conditions, such as different RHs, different temperatures, and different contact surface wettabilities. The rest of the study did not include gecko-inspired composite mushroom fibers to eliminate material-wise external contributions such as viscoelastic effects. In this section 4.2, the rest of the survey continued only with monolithic structures

(single material structures, that means *VS mushroom fibrils*) to have a fair comparison with live geckos.

Live geckos' and GSAs' shear adhesion were measured for different RHs (30%, 55%, 70%, 80%) and surface wettabilities (hydrophilic, hydrophobic). As a result, live geckos' and GSAs' adhesion increased on hydrophilic contact surfaces when the RH increased. This result is proof of capillary force contribution since capillary force can only happen between two hydrophilic surfaces. Then, the live gecko's shear adhesion was slightly enhanced when the RH increased on hydrophobic surfaces (octadecyl trichlorosilane self-assembled monolayer (OTS-SAM) coated glass). This finding proves the material softening contribution on live geckos by eliminating capillary force contribution due to hydrophobic contact surface. As the material softening theory states, when material softens (in this case, gecko's seta), the contact area increases; as a result, this improves the shear adhesion

performance of the live geckos. Additionally, no statistical difference was observed for GSA shear adhesion performances under different RHs on hydrophobic surfaces. This result showed the material-wise robustness of the GSA under different RHs. Thus, there were no material softening contribution for GSA adhesion under different RHs (Figure 4.6).

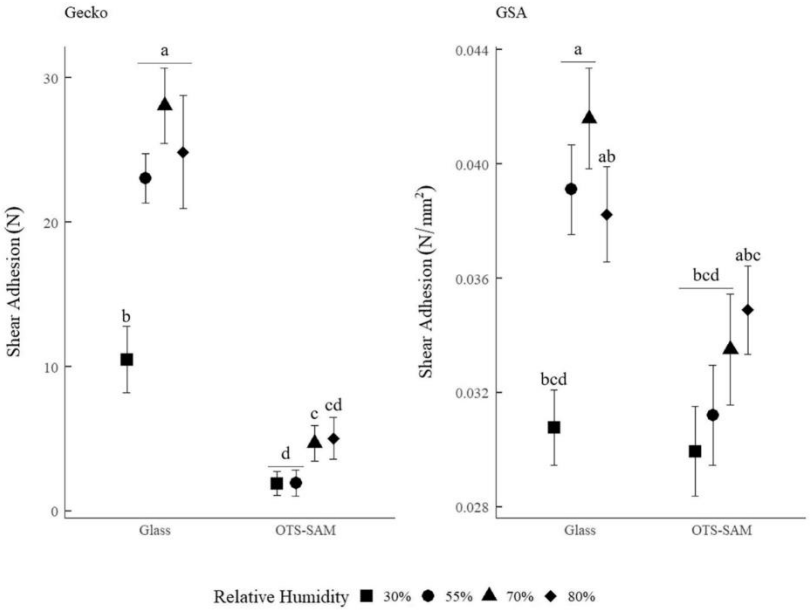

Figure 4.6. Tokay gecko and gecko-inspired synthetic adhesive shear adhesion in variable relative humidity on hydrophilic and hydrophobic glass. The shear adhesion of live geckos is measured as the maximum shear force resisted before sliding (N), and the shear adhesion of GSAs is calculated as the maximum shear force resisted while sliding per unit area (N/mm^2) (mean ± s.e.m.). The means of treatment groups denoted with the same letter are not statistically different, according to Tukey post hoc pairwise statistical tests. The s.e.m. (standard error of the mean) is calculated simply by dividing the standard deviation by the sample size's square root.

Then, live geckos' and GSAs' shear adhesion were measured for different temperatures (12 ºC and 32 ºC) and RHs (30%, 55%, 70%, 80%). At low temperature (12 ºC), when RH increases, there is a high chance of condensation on the contact surface, which contributes to the capillary force for adhesion. At high temperature (32 ºC), when RH increases, there is a low chance of creating condensation on the contact surface, which eliminates the capillary force. Therefore, it makes the material softening contribution more detectable for adhesion. Live geckos' and GSAs' shear adhesion increased at low temperatures when the RH increased due to capillary force contribution. After that, live geckos' adhesion increased at high temperatures when the RH was increased due to the material softening effect. As the material softening theory states, when material softens (in this case, gecko's seta), the contact area increases; as a result, this improves the shear adhesion performance of the live geckos. On the other hand, there were no statistical differences in adhesion for GSA between different RHs at high

temperatures due to the material-wise robustness of the GSA. This result proved no material softening contribution to GSA adhesion (Figure 4.7).

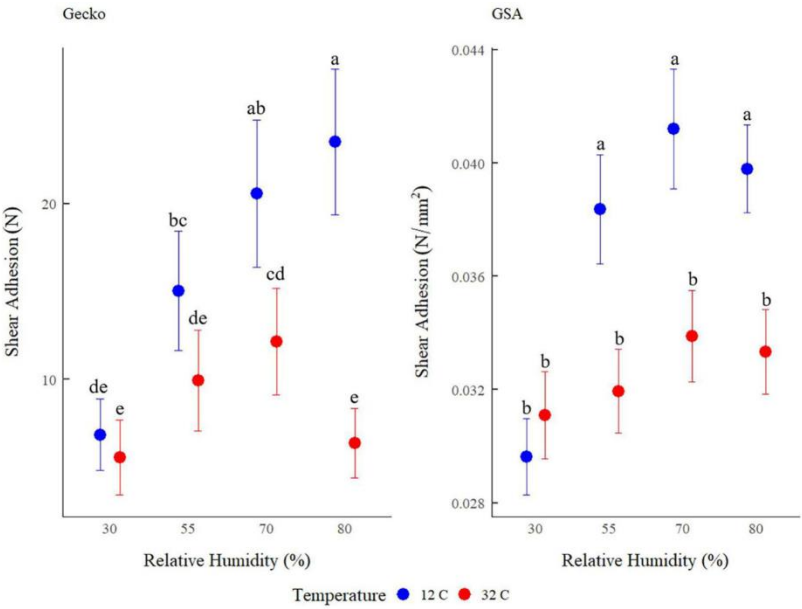

Figure 4.7. Tokay gecko and gecko-inspired synthetic adhesive shear adhesion in variable relative humidity and temperature. The shear adhesion of live geckos is measured as the maximum shear force resisted before sliding (N), and the shear adhesion of GSAs is measured as the maximum shear force resisted while sliding per unit area (N/mm^2) (mean ± s.e.m.). The means of treatment groups denoted with the same letter are not statistically different, according to Tukey post hoc pairwise statistical tests. The s.e.m. (standard error of the mean) is calculated simply by dividing the standard deviation by the sample size's square root.

4.3 3D Printing of Elastomeric Bioinspired Complex Adhesive Microstructures

This section is based on paper 2 in Chapter 1, *3D printing of elastomeric bioinspired complex adhesive microstructures*.

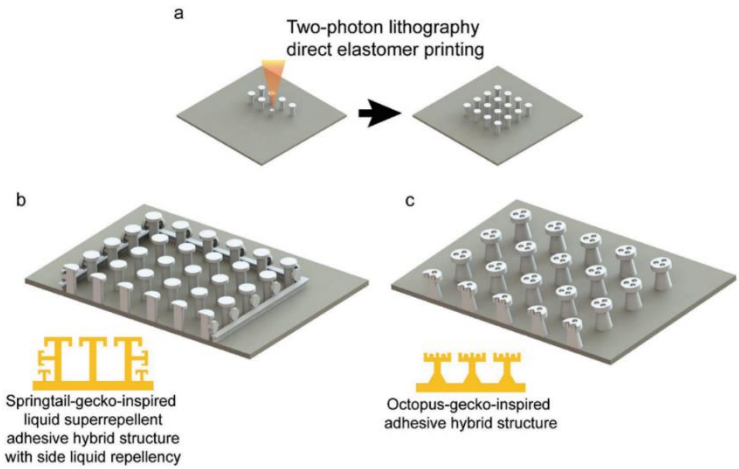

Figure 4.8. Direct 3D printing-based approach for fabricating elastomeric bioinspired complex adhesives. a) Schematics of the fabrication process. 2PP-based direct 3D printing of the structures using a custom elastomeric resin. b, c) Inspiration sources and designs of two hybrid bioinspired adhesives. b) Springtail- and gecko-

inspired adhesive hybrid structures with side-surface liquid repellency. c) Octopus- and gecko-inspired adhesive hybrid structures with strong underwater and dry adhesion.

The shape and performance of the existing adhesive microstructures highly depend on fabrication techniques such as molding. To overcome these limitations, a 3D elastomeric microstructure fabrication technique was implemented using 2PP-based 3D printing (Figure 4.8a). This fabrication approach could produce many other 3D complex elastomeric structural adhesives for future real-world applications. To demonstrate this approach's capability, two unsolved issues for gecko-inspired adhesives were focused on as challenging tasks. As the first challenging task, side-surface liquid repellency, top-surface liquid repellency, and dry adhesion features were combined in the same design (Figure 4.8b). The underwater adhesion of gecko-inspired elastomeric structures was shown as a second challenging task

(Figure 4.8c). For the first challenge, springtail-gecko-inspired, and for the second task, octopus-gecko-inspired elastomeric adhesive microstructures were fabricated with the proposed approach (Figure 4.9).

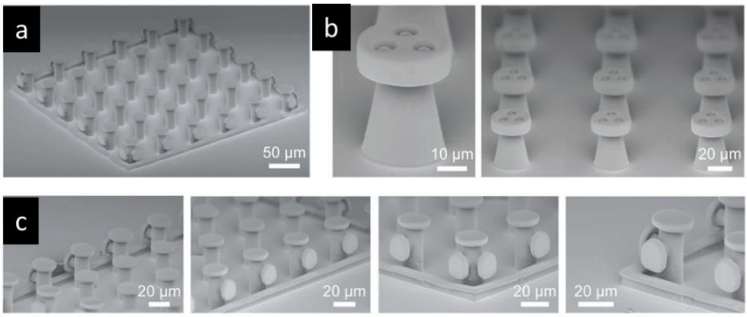

Figure 4.9. The SEM images of the fabricated elastomeric bioinspired complex adhesives. a) A full array of double re-entrant structures with side-surface liquid repellency. b) A single and an array of octopus–gecko-inspired adhesive microstructures. c) Zoomed SEM images of the side and vertex structures of the springtail–gecko-inspired adhesive structure array.

4.4 Machine Learning-based and Experimentally Validated Shear Optimal Fibril Adhesives

This section is based on paper 1 in Chapter 1, *Machine learning-based and experimentally validated shear optimal fibril adhesives*.

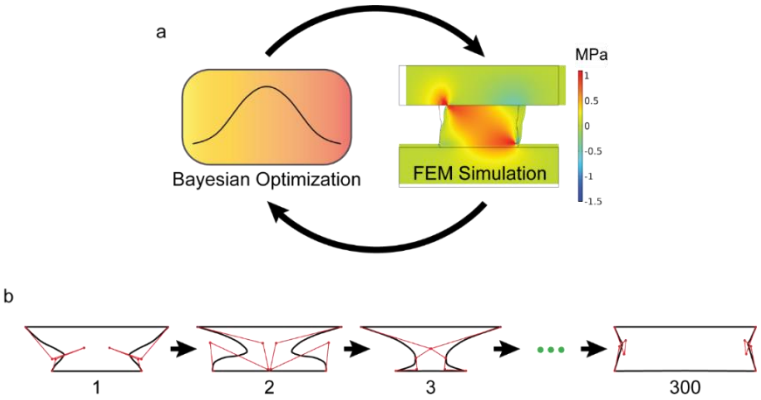

Figure 4.10. Overall summary for investigating the Bayesian optimization-based shear-optimized microfibril designs. a) Optimization framework for investigating the ML-based optimal microfibril designs. b) Starting from a random shape, the fibril design changes in each iteration until obtaining the maximum shear force.

After all previous investigations, explorations, and the development of advanced fabrication techniques for adhesive fibrils, we want to explore further more about their potential performance. The previous sections' findings were necessary for fabricating, investigating, developing, pushing the limits, and improving the current performance of gecko-inspired adhesives. In this section, an ML method, FEM simulation, and Bezier curve-based free-form design approach were integrated into our exploration. Free-body design (Bezier curve-based design) was used instead of pre-defined shapes for a broad range of investigation of optimal structures.

FEM-based shear simulation and the BO (an ML method) were integrated to investigate shear optimal fibril adhesives to find the optimal solution iteratively (Figure 4.10a). To design fibrils freely, the body shape of the fibrils was defined with a Bezier curve (Figure 4.10b). FEM simulation was used for shear force estimation, and the BO was used for investigating the optimal estimated design (Figure

4.10a). BO suggested design parameters (Bezier curve control points) to evaluate the estimated shear force for the simulation. This iterative process continued until the iteration limit (300 iterations) was achieved, which gave us, the optimal fibril design. The iteration limits have been decided based on saturation to the optimal value (Figure 4.10).

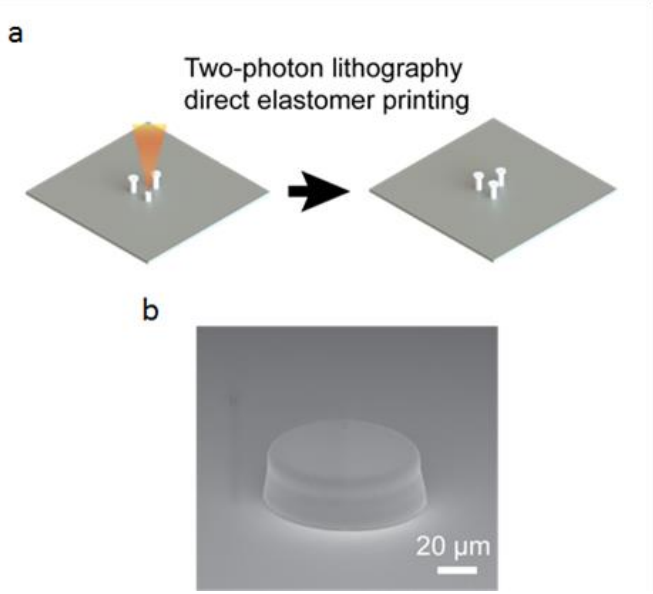

Figure 4.11. The fabrication procedure and an example SEM image of the optimal fibrils. a) Fabrication procedure of the optimal fibrils using the 2PP technique using an elastomeric resin material. b) The SEM image of a sample fabricated optimal microfibril with an 80 µm tip diameter and 0.4 aspect ratio (AR).

For simulations, commercial FEM software (COMSOL Multiphysics 5.6, COMSOL Inc.) was used. The simulations were implemented to estimate shear force for the standard (pre-defined) and

optimal fibril shapes. In simulations, the fibril base was fixed on the substrate, and the top part of the fibril tip end was in contact with the contact surface. At the beginning of the simulation, the contact surface iteratively translated and compressed the fibril on the *y*-axis until reaching ~600kPa. After that, the fibril substrate moved on the *x*-axis until the fibril tip stress reached the critical interfacial normal stress. The simulation ended after reaching critical interfacial normal stress, and the shear force was calculated. The shear force of the fibril design was calculated by integrating the shear stress on the fibril tip line, leading to unit force per length (N/m). After taking the line integral of the shear stress on the tip (results in “force divided by the length” unit because of two-dimensional (2D) simulation), the resulting unit force was divided by the measured tip diameter of the fibril to find shear stress. Then, the result was multiplied by the tip area of the fibril to find the total shear force.

Some material characterizations have been done experimentally for simulations. First, standard designs (flat-punch pillar and wedge mushroom) were fabricated by the 2PP method. As a resin material, commercially available IP-PDMS elastomeric resin was used. The SEM images were used for defining the geometrical fabrication limitations; the minimum tip-edge fillet radius. These fabrication limitations were also included in simulations. For the hyperelastic model in simulations, Mooney-Rivlin two parameters were used. The normal adhesion measurements were conducted to find the Mooney-Rivlin parameters. For finding the theoretical critical stress values, shear characterizations were realized for all standard fibrils (flat-punch pillar and wedge mushroom). The shear adhesion measurements were matched with the shear simulations for all standard shapes and categories (tip diameters and ARs) by minimizing the root-mean-squared relative error to find each AR's theoretical critical stress. For each AR, there were different theoretical critical stresses. The critical

stress values for ARs 1, 0.6, and 0.4 were -264.0 kPa, -14.5 kPa, and 362.9 kPa, respectively.

The design of the fibrils includes fixed and optimizable parameters. The fixed parameters include the minimum edge fillet radius, tip diameter (for each category), AR (for each category), Mooney-Rivlin parameters, and theoretical critical stress (for each AR). The optimizable parameters include the 4^{th} degree of Bezier-curve control points with three Bezier-curve control points and a fibril base diameter. Each simulation was 2D, including more than 10,000 free triangular elements as meshes. Significantly, the meshes were extremely fine toward the tip of the fibril to catch the theoretical critical stress for detachment precisely.

The FEM simulation was built in 2D for all shapes. The contact surface was assumed as smooth and locally flat. The side profile of the 3D fibril was modeled using a Bezier curve. Three different ARs (1, 0.6, 0.4) and three different tip

diameters (40, 60, 80 μm) were considered to explore the fibril size effects. In addition, 2PP-based 3D fibril fabrication limitation, such as the minimum achievable fillet radius of 2.7 μm at the tip of the fibrils, was integrated into the simulations.

The shear performance of a fibril was simulated with its nonlinear deformation using the Mooney-Rivlin hyperelastic model[65,66]. At the beginning of the simulations, all the fibrils were compressed with a locally flat probe with a constant preload pressure. After compression, the fibril base was moved to the right side with small step sizes to create shear on the fibril. After reaching the preload pressure and after the shear starts, the *z*-position is kept fixed during measurements. It means that the applied normal pressure was not kept constant after shearing started, so it was not controlled by any feedback mechanism to keep it at the same value during measurements. During the shear, if the interfacial theoretical critical stress value[67,68] was reached on

any fibril's tip surface region, then the simulation assumed that the fibril detached from the surface.

As an optimizer, the BO method was used and connected to the FEM simulation. One of the main advantages of this method was keeping the iteration number as low as possible. This optimization method could help decrease the number of simulation runs and increase our approach's efficiency. The fixed parameters were the minimum fillet radius due to the fibril fabrication limitations, the fibril tip diameter, and the fibril height for corresponding categories. In each iteration, the optimization framework considered the Bezier-curve control points as optimizable variables and suggested the optimal design (Figure 4.10). Our method aimed to maximize the shear force. Here, all fibril designs were directly fabricated by a 2PP process with an elastomeric resin material (Figure 4.11). Before starting the optimization process, the essential parameters were experimentally measured and included in the simulations, such as the

hyperelastic model parameters, the minimum fillet radius due to fabrication limitations, and the theoretical interfacial critical stress.

The BO was implemented using a pre-built function called “bayesopt.m” on MATLAB (MATLAB R2018a, The MathWorks, Inc.). As an acquisition function, expected improvement was used. The number of iterations was set to 300. The Bayesian optimizer (implemented in MATLAB) was linked with COMSOL FEM simulation via LiveLink. In each iteration, the Bayesian optimizer’s suggested design was sent to FEM simulation. The FEM simulation ran and calculated the estimated shear force. Afterward, the estimated shear force was returned to the Bayesian optimizer to decide which design point should be evaluated next. All process took approximately 5 hours to find the optimal design for one specific tip diameter and AR. This framework was implemented on a desktop computer with an Intel Xeon CPU with 20 cores (E5-2680 v2, 2.80

GHz), 192 GB RAM, and an NVIDIA Quadro K5000 graphics card.

For each standard and optimal fibril design, the computer-aided design was implemented by Solidworks, and then a stereolithography file (.stl) was created. The generated files were uploaded into the Nanoscribe software (Photonic Professional GT2, Nanoscribe GmbH, Germany). The 2PP system was used in DiLL mode. In this mode, the elastomeric resin material (IP-PDMS, Nanoscribe GmbH, Germany) was placed between the substrate glass and the objective. As the objective lens, 25x, 0.8 numerical aperture (NA) objective was used. After the printing of desired fibril structures, the post-process was applied. The fabricated fibrils were immersed in a beaker containing isopropyl alcohol (IPA) for 15 min. Next, the samples were immersed in another beaker containing fresh IPA for 2 min. Young's modulus of the material was 15.3 MPa. For material behavior on a small scale, a T-shape fibril's stress-strain curve on a smooth spherical glass was

used for Mooney-Rivlin's second-order model fitting. The computed Mooney-Rivlin second-order model fitting parameters were used in all simulations. These values were C10 = 1.01e+6 Pa and C01 = 5.96e+5 Pa.

A custom-made shear-adhesion setup was used for shear and normal force measurements. To visualize the measurements, a video camera (Grasshopper3, Point Grey Research Inc.) was mounted on an inverted optical microscope (Axio Observer A1, Zeiss). For *z*-direction and *y*-direction, a computer-controlled high-precision stage (LPS-65 2", Physik Instrumente GmbH & Co. KG) was attached to the microscope. Two load cells (*y*-axis: LSB200, 100g, JR S-Beam, FUTEK, and *z*-axis: GSO-25, Transducer Technique LLC) were mounted on the stage in an orientation to measure the forces on the *y*-axis and *z*-axis. The motion of the piezo stages was controlled, and a custom-made program processed the data acquisition by a LabVIEW (National Instruments, Austin, TX, USA). A smooth

spherical glass probe with a 10 mm diameter was used as a contact surface. The load-drag tests were done for shear. Before applying shear, the normal pressure (~600 kPa) was exerted on the fibril. After reaching the desired preload, 60 seconds of relaxation time waited. Tangential displacement was applied for 1 mm after relaxation time. During the measurements, all speeds (approaching speed on the *z*-axis, shear speed on the *y*-axis, and retraction speed on the *z*-axis) were set to 5 μm s^{-1}. Each measurement was repeated five times.

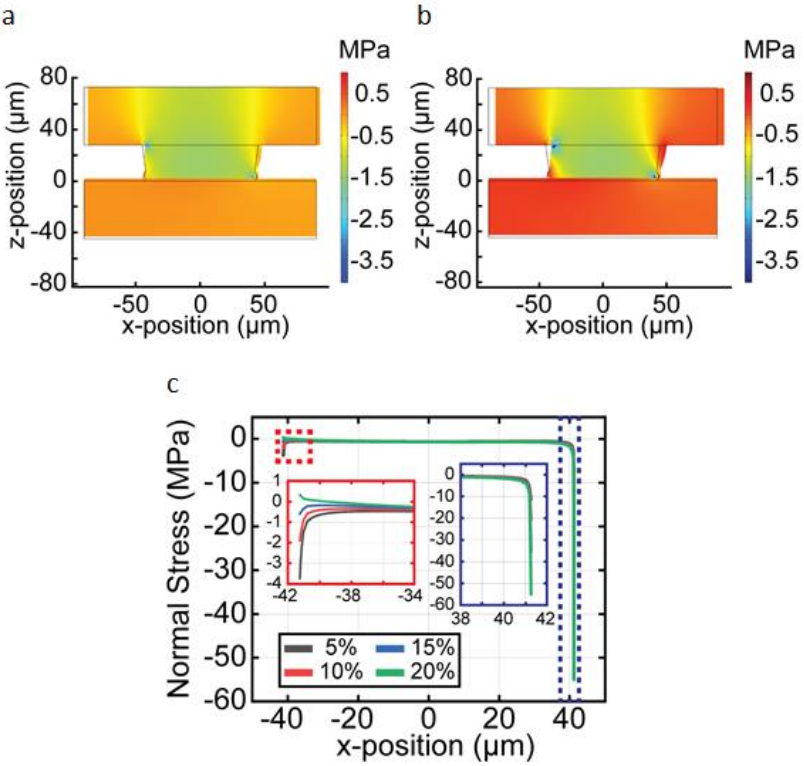

Figure 4.12. Normal stress distribution under different shear strains for an 80 μm tip diameter and AR 0.4 ML-found optimal design. Normal stress distribution a) under 10% shear strain, b) under 20% shear strain, c) on a tip-contact surface interface for four different shear strains (5%, 10%, 15%, 20%) for 80 μm tip diameter and AR 0.4 ML-found optimal design are shown, respectively.

During shear, the interfacial stress of the optimal fibril showed that the stress distributions were changing along the fibril tip contact surface area (Figure 4.12, 4.13). The normal stress distribution of the fibril showed that the opposite side of the shear direction of the fibril edge's interfacial stress distribution values increased during shear. After reaching the critical interfacial stress, the opposite side of the shear direction of the fibril edge's interfacial stress distribution was assumed to be detached from the surface. As a result, the detachment started from the critical interfacial stress-reached part of the fibril and continued as a crack propagation to the other end of the fibril (Figures 4.12). During shear, the interfacial shear stress distribution of the fibril also changed. The shear stress values increased along the fibril interface during shear. Especially, both ends of the fibril's interfacial stress values increased drastically (Figure 4.13).

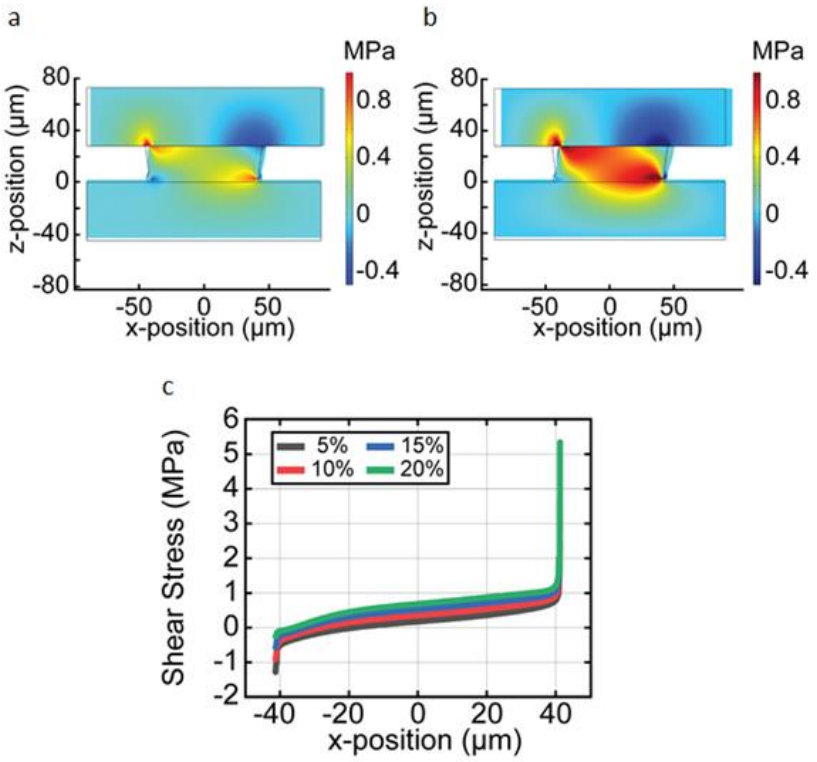

Figure 4.13. Shear stress distribution under different shear strains for an 80 μm tip diameter and AR 0.4 ML-found optimal design. Shear stress distribution a) under 10% shear strain, b) under 20% shear strain, c) on a tip-contact surface interface for four different shear strains (5%, 10%, 15%, 20%) for 80 μm tip diameter and AR 0.4 ML-found optimal design are shown, respectively.

The optimized fibrils with various tip diameters and ARs were found with the proposed optimization framework. The fibrils' three different tip diameters (40, 60, and 80 μm) were optimized for three different ARs (1, 0.6, and 0.4). All of the nine optimal fibril designs are shown in Figure 4.14. For high AR (AR equals to 1) fibril designs, the stiffness of the fibrils was tried to be increased by maximizing the Bezier curve control points to obtain higher shear force.

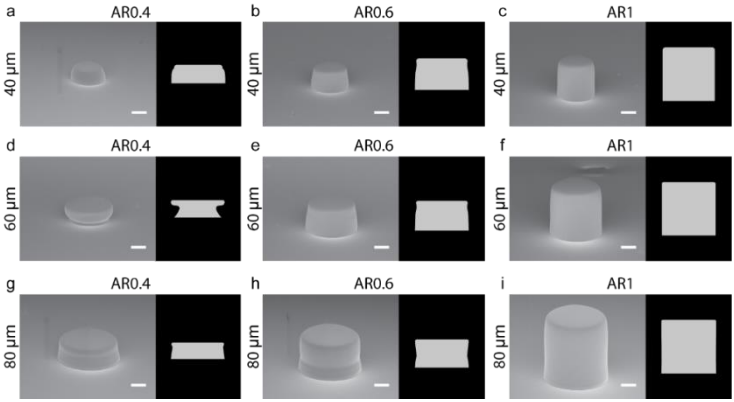

Figure 4.14. SEM images of the fabricated ML-found optimal elastomeric fibril structures for different tip diameters and ARs. The tip diameter 40 µm, 60 µm, and 80 µm designs are [a), b) and c)], [d), e) and f)], [g), h), and i)], respectively. The AR 0.4, 0.6, and 1 designs are [a), d) and g)], [b), e) and h)], [c), f), and i)], respectively. All scale bars are 20 µm.

The shear performance of the fabricated optimal fibrils was characterized by a hemispherical-smooth glass probe with a 10 mm diameter. Since the tip diameters of the fibrils were much smaller than the smooth glass probe, flat-flat contact geometry can be assumed between the fibrils and

the contact probe during measurements. All 40 µm tip diameter fibril designs were printed as a tripod with three structures for measurements. The rest of the tip diameter designs (60 and 80 µm) were fabricated as a single structure. Standard shapes (flat-punch and wedge-shaped mushroom fibrils) were also fabricated and considered as a control in this study. These structures were widely known and commonly used for high adhesion and shear in the literature.

Shear performance comparison among all possible fibril designs was shown in Figure 4.15 with experimental and simulation results. In all cases, ML-based optimal fibril designs performed better than the standard shapes in simulations and experiments. Moreover, the simulation-based prediction of shear forces showed agreement with the experiments in all fibril designs and categories. The results show that if the fibril's tip diameter increases, the fibril's shear force increases for a single structure. This phenomenon also applies to

AR. If the AR decreases, the fibril's shear force increases for a single fibril. This trend is related to the stiffness of the fibrils. If the stiffness of the fibril rises, then its shear performance also increases. However, there should be a limit to increasing the stiffness of the structures. If the stiffness of the made of material of the fibrils increases, then after a certain point, the conformal contact between the fibril tips and the contact surface worsens, which would reduce the shear performance.

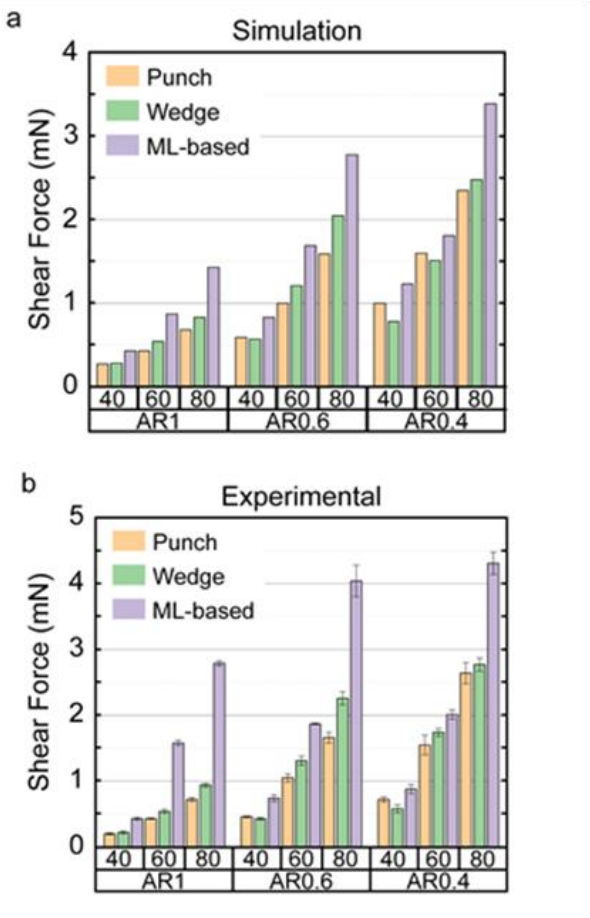

Figure 4.15. Shear adhesion results in FEM simulations and experiments for a single fibril using standard shapes (flat punch, wedge-shaped mushroom) and ML-based shear optimal designs. a) The FEM simulation results show that ML-based optimal designs have better shear

performance than the standard flat punch and wedge-shaped fibril designs. b) The experimental results agree with the FEM simulation results, proving that the ML-found designs give higher shear forces than the standard shapes in all cases.

Appendix A. Bio-inspired Composite Microfibers for Strong and Reversible Adhesion on Smooth Surfaces

This appendix includes the following publication:

1. Dirk-Michael Drotlef, **Cem Balda Dayan**, and Metin Sitti, Bio-inspired composite microfibers for strong and reversible adhesion on smooth surfaces. *Integrative and Comparative Biology*, 2019, doi: 10.1093/icb/icz009.

Integrative and Comparative Biology
Integrative and Comparative Biology, volume 59, number 1, pp. 227–235
doi:10.1093/icb/icz009
Society for Integrative and Comparative Biology

SYMPOSIUM

Bio-inspired Composite Microfibers for Strong and Reversible Adhesion on Smooth Surfaces

D.-M. Drotlef*, C. B. Dayan* and M. Sitti[1]

*Physical Intelligence Department, Max Planck Institute for Intelligent Systems, Stuttgart 70569, Germany

From the symposium "The path less traveled: Reciprocal illumination of gecko adhesion by unifying material science, biomechanics, ecology, and evolution" presented at the annual meeting of the Society of Integrative and Comparative Biology, January 3–7, 2019 at Tampa, Florida.

[1]E-mail: sitti@is.mpg.de

Synopsis A novel approach for high-performance gecko-inspired adhesives for strong and reversible adhesion to smooth surfaces is proposed. The composite patterns comprising elastomeric mushroom-shaped microfibers decorated with an extremely soft and thin terminal layer of pressure sensitive adhesive. Through the optimal tip shape and improved load sharing, the adhesion performance was greatly enhanced. A high adhesion strength of 300 kPa together with superior durability on smooth surfaces are achieved, outperforming monolithic fibers by 35 times. Our concept of composite microfibrillar adhesives provides significant benefits for real world applications including wearable medical devices, transfer printing systems, and robotic manipulation.

Introduction

Nature offers inspiring strategies for strong and reversible adhesion to complex environments. For instance, geckos can reversibly adhere to various surfaces with their adhesive pads covered by dense array of fine curved setae decorated with spatula (Autumn et al. 2000, 2002; Autumn 2006). For the past decades, gecko-inspired adhesives have been extensively studied for adhesion to both smooth and rough surfaces. Their adhesion enhancement by contact splitting (Arzt et al. 2003), contact geometry (Kim and Sitti 2006; del Campo et al. 2007), or the mechanism of equal load sharing (Carbone and Pierro 2012; Aksak et al. 2014) are well understood. Consequently, artificial mimics demonstrate strong and reversible adhesion and even surpass the adhesion performance of the gecko on smooth surfaces (Ge et al. 2007; Murphy et al. 2009; Drotlef et al. 2014).

Recently, the composition of animals' setae has revealed their mechanically graded structure (Peisker et al. 2013). Additionally, it has been reported that softening of the setae upon variations in environmental conditions (e.g., humidity) can improve the adhesion performance (Puthoff et al. 2010; Prowse et al. 2011). Inspired from these recent findings, composite microfibers with a continuous soft layer on the top of their tips (film-terminated fibers) (Shahsavan and Zhao 2014), hard fiber cores and soft shell (Minsky and Turner 2015), and microfibers with hard fibers and soft tips (Fischer et al. 2017; Gorumlu and Aksak 2017) have been demonstrated. Recently, we have shown that direct cross-linking of composite microfibers decorated with viscous tips on various surfaces can greatly boost the adhesion (Drotlef et al. 2017). However, the reversible adhesion performance of these composite architectures is still challenging.

Here, we propose bio-inspired composite microfibers for strong and reversible adhesion to smooth surfaces. The proposed microfibrillar patterns are composed of polydimethylsiloxane (PDMS) fibers decorated with vinylsiloxane (VS) mushroom-shaped tips, which are additionally coated with an extremely soft and thin terminal layer of silicone-based pressure sensitive adhesive (S-PSA). We demonstrate that mushroom tips coated with thin S-PSA terminal layers can greatly enhance the adhesion

Advance Access publication April 27, 2019

through their optimal shape and enhanced load sharing. A high adhesive strength of 300 kPa together with superior reversibility on planar surfaces are achieved after tailoring the tip geometry, tip composition and terminal layer thickness, and tip edge sharpness.

Results and discussion

The fabrication process of composite micropatterns is illustrated in Fig. 1 (see the "Materials and Methods" section for details). Composite micropatterns with various tip geometries and tip compositions were obtained by employing soft molding techniques (del Campo et al. 2007; Drotlef et al. 2013). Briefly, the S-PSA precursor solution was first cast onto a glass plate and a thin and homogeneous film was obtained by a film applicator (Step 1). After partial crosslinking of the S-PSA layer (Step 2), the PDMS microfibers with VS mushroom-shaped tips were manually inked onto the thin layer, leading to the selective transfer of the viscous S-PSA onto microfiber tips (Step 3). The microfibers coated with S-PSA were then printed onto a salinized silicon wafer (Step 4), peeled-off (Step 5), printed a second time on a pristine wafer, and cured at room temperature for 12 h (Step 6). Finally, the patterns were carefully peeled-off from wafer and homogeneous composite micropatterns with a diameter of 67 µm, spacing of 33 µm, and height of 95 µm were fabricated (Step 7).

We selected S-PSA as our tip coating material due to its several key characteristics. First, S-PSA is much softer than PDMS and has a Young's modulus of ca. 75 kPa, enabling superior conformation to various surfaces or skin. The Young's modulus was determined from load–displacement curves (Greiner et al. 2007). Second, its suitable viscosity enables efficient inking and printing process. Third, it belongs to the family of silicone polymers and allows covalent bonding with the PDMS. Last, S-PSA is developed and approved for biomedical applications and may be suited for skin related applications.

To optimize the shape and layer thickness of multilayer composite microfibers, we prepared fibers with different tip geometries by varying the inking and printing process, the layer thickness of the S-PSA, and the pre-crosslinking duration. Consequently, we evaluated the surface topography of all adhesive patterns, the quality of the coated tips (Fig. 2), and finally their adhesion performance (Fig. 3).

Inspired by fine hairs of various animals comprising different tips geometries (e.g., flat, hemispherical, conical, toroidal, filament-, band-, and suction cup-like shapes; Spolenak et al. 2005), together with modification of previously reported soft molding techniques (del Campo et al. 2007), microfibers with hemispherical tips, S-PSA mushroom fibers, film-terminated fibers (Fig. 2A), composite mushroom fibers with different S-PSA terminal layer thickness, tip wedge angles, and tip sharp edges were obtained.

As shown in Fig. 2B, S-PSA films with layer thickness ranging from 25 to 30 µm resulted in homogeneous and medium sized mushroom-shaped tips. For thinner layers, however, the transferred S-PSA to the microfiber tips was small and formed small mushroom tips. On the other hand, microfibers were fully immersed in S-PSA when the layer thickness approached or surpassed the fiber height.

Further, we found that 7–9 min was the ideal pre-crosslinking time range for mushroom patterns with medium sized and homogeneous tips. For shorter pre-crosslinking time, the initial viscosity was low and the amount of the transferred S-PSA to the tip of microfibers was large, leading to film-terminated, inhomogeneous, and connected microfiber tips. Moreover, the viscosity was high for long pre-crosslinking duration and thus a small amount of S-PSA was transferred to tips.

Next, homogeneous and large composite mushroom-shaped tips with 2 µm thin S-PSA layers were formed when mushroom patterns with VS tips were inked after 14–15 min pre-crosslinking time (see Fig. 2C). In contrast, connected and island-like microfiber tips were formed for shorter pre-crosslinking durations (see the "Materials and Methods" section for details).

Finally, composite mushroom patterns with sharp tip edges and a tip wedge angle of 57° were obtained by the double printing (DP) process, while composite mushroom patterns with rounded tip edges and a tip wedge angle of 52° were obtained by the single printing process (see Fig. 2D). Notably, VS mushroom patterns have sharp tip edges and a tip wedge angle of 61° prior the inking and printing process.

To investigate the effect of tip geometry on adhesion, the force–displacement curves were measured by a customized adhesion setup (see the "Materials and Methods" section for details). Figure 3A illustrates the adhesion of microfibrillar adhesives with different tip geometries. The maximum adhesion force of 35 mN was achieved by homogeneous and large mushroom-shaped S-PSA tips, while smaller and deformed tips exhibit a lower adhesion performance. Furthermore, patterns with planar PDMS fibers, spherical, film-terminated tips, and a flat S-PSA control showed 6, 14, 30, and 31 mN, respectively. In comparison to patterns with cylindrical uncoated tips, mushroom

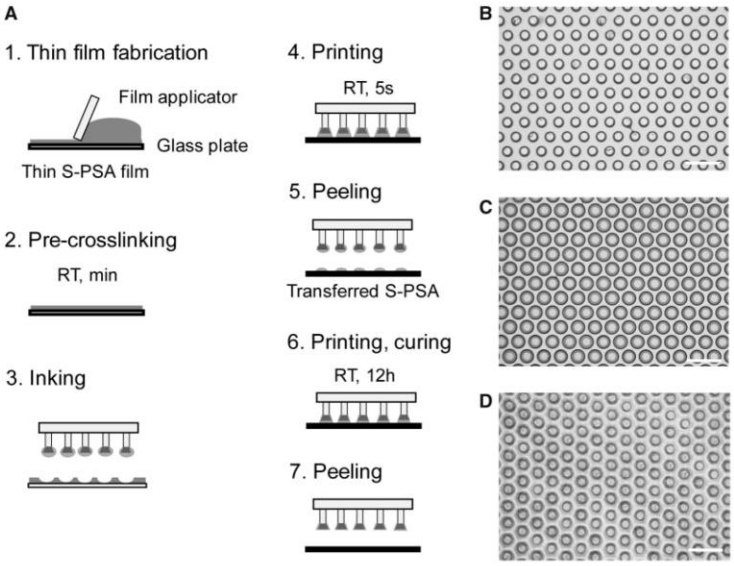

Fig. 1 Fabrication process of the microfibrillar mushroom patterns (**A**); fabrication and precuring of the thin S-PSA film (Steps 1–2), inking and printing of microfibrillar patterns onto a silicon wafer (Steps 3–4), second printing process (double printed) on a pristine wafer, curing, and peeling (Steps 6–7). Microscopy images of the fabricated patterns with S-PSA mushroom tip (**B**), double printed composite mushroom fibers with optimally shaped tips (**C**), and film-terminated patterns (**D**). Scale bars: 200 μm.

patterns show a six-fold increase of the adhesive strength.

Similar observations were reported in previous studies, demonstrating the superior adhesion of mushroom fiber over other tip geometries (del Campo et al. 2007; Drotlef et al. 2013). However, our results prove that the same behavior applies for composite mushroom fibers. The superior adhesion performance of mushroom-shaped fibers originates from the more uniform stress distribution at the fiber tip interfaces (Kim and Sitti 2006; Carbone and Pierro 2012). The higher adhesion performance of larger mushroom tips is attributed to their optimized geometry and subsequent improved load sharing (Carbone and Pierro 2012; Marvi et al. 2015).

At this point, it is of interest to compare our S-PSA mushroom micropatterns to related composite adhesives in literature. In a macroscopic approach, a stiff fiber core with 1.25 mm diameter was covered by a compliant PDMS shell with varying tip layer thickness between 100 and 1500 µm (Minsky and Turner 2015). By introducing of a stiff core, an adhesion enhancement by the factor of 3 compared with monolithic soft sample was observed. In another work, a 2 mm diameter stiff fiber stalk with a softer tip layer varying between 20 and 500 µm thickness was studied (Fischer et al. 2017). It was found that composite pillars improved the adhesion to the smooth substrates by a factor 2–3 compared with conventional pillar structures made from monolithic material.

In our experiments, we found a similar improvement by a factor of 2 for fibers with a hemispherical S-PSA tip compared with monolithic PDMS fibers. However, when we tested mushroom fibers with S-PSA tips, a six-fold enhancement was observed largely due to optimal tip shape and improved load sharing.

Although our S-PSA mushroom fibers demonstrated enhanced performance, the size and shape of the tip could not be further altered without causing folding of the thin mushroom rim or fiber coalescence. To overcome these limitations, instead of solely cylindrical fibers, mushroom fibers with VS tips were employed in the inking and printing process. Thereby, large and homogeneous composite mushroom fibers with a thin S-PSA terminal layer were obtained. The stiffer mushroom tip supports soft S-PSA layer, allowing homogeneous and robust

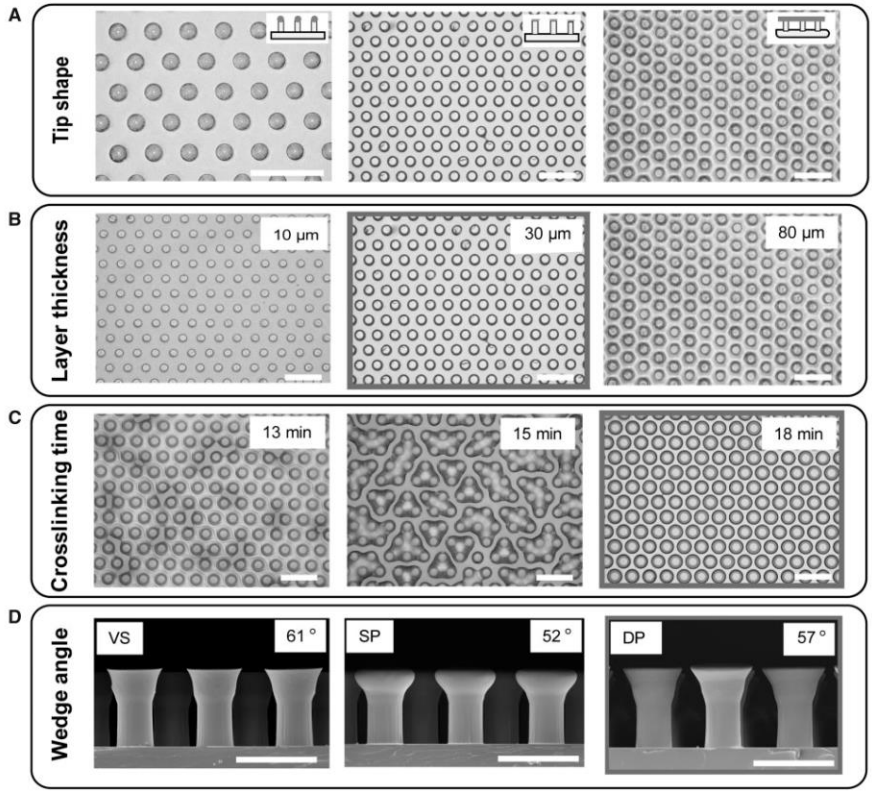

Fig. 2 Optimization of the process parameters, including microfibrillar tip shape, layer thickness, pre-crosslinking duration, and wedge angle. Optical microscopy images of patterns with different tip geometry (**A**). Microscopy images of microfibrillar patterns with small and medium S-PSA mushroom tips and micropatterns fully embedded in S-PSA, after inked onto S-PSA films with different thickness (**B**). Microscopy images of composite mushroom microfibers inked into S-PSA films after different pre-crosslinking durations (**C**). Cross-sectional SEM images of mushroom patterns before (VS), after the single (SP) and the DP process, showing fiber tip geometries with varying wedge angles and wedge sharpness **(D)**. Optimal process parameters are indicated with gray borders. Scale bars: (A–C) 200 µm and (D) 100 µm.

tips, suppressing the folding of the delicate rim. These multilayered composite fibers exhibit an improve adhesion force of 70 mN which is 2 and 12 times higher than S-PSA mushroom and monolithic PDMS patterns, respectively (Fig. 3C).

Although these patterns demonstrate enhanced adhesion, the overall quality and homogeneity of the patterns were further improved by employing a double-printing (DP) process. Here, the S-PSA-coated VS mushroom patterns were peeled-off directly after the first printing process, before the S-PSA polymerized. Thereby S-PSA precursor solution was transferred from the fiber tip to the substrate, resulting in a reduced S-PSA layer thickness on the fiber after printing on a pristine substrate.

Laser scanning microscope characterizations revealed that the thickness of the S-PSA layer on the VS mushrooms patterns was reduced from 2 to 1 µm through the DP process (Fig. 3B). Further, cross-sectional SEM characterization of mushroom patterns showed that mushroom fiber tips of the DP composite patterns have sharp edges and a wedge angle of 57°, while SP composite patterns have rounded tip edges and a tip wedge angle of 52°.

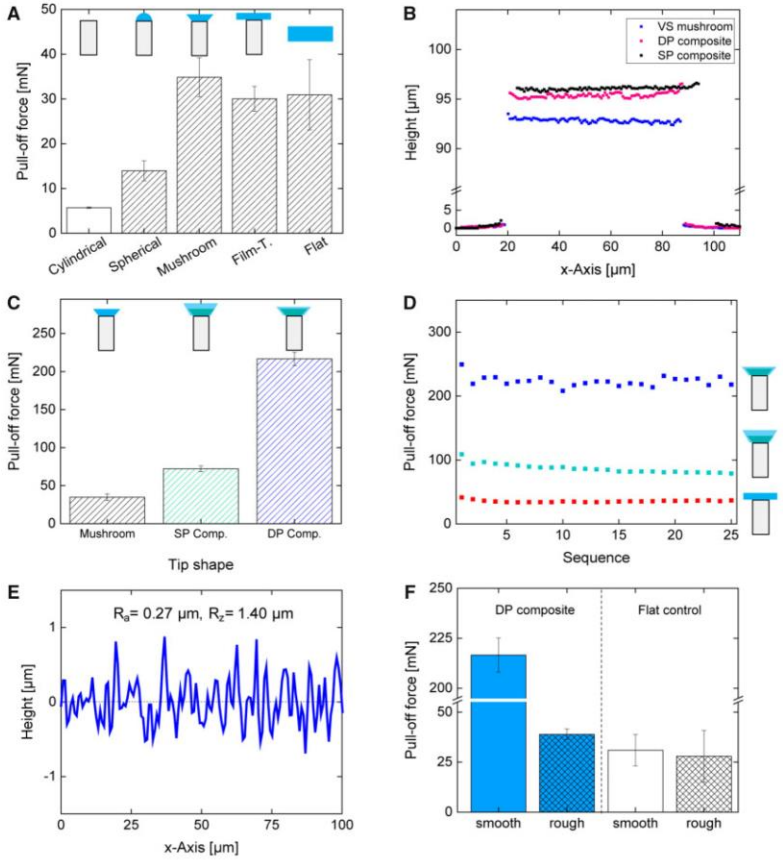

Fig. 3 Adhesion measurements of microfibers with various tip geometries and the mushroom composite microfibrillar adhesives with height profiles measured with a 3D laser-scanning microscope. Pull-off force of microfibers with different tip geometries and a flat S-PSA control, measured on a smooth substrate (**A**). 3D laser-scanning microscope height profiles of mushroom patterns before (VS mushroom), after the SP or the DP process (**B**). Pull-off force of microfibers with S-PSA mushroom tips and SP- and double-printed composite mushroom patterns (**C**). Pull-off force of SP and double printed composite mushroom fibers in a durability test over 25 adhesion cycles, compared with film-terminated microfibers (**D**). Surface profile of the rough probe employed for adhesion characterizations with an arithmetical mean deviation (R_a) of 0, 27 µm and mean peak-to-valley roughness (R_z) of 1.4 µm, obtained by 3D laser scanning microscopy (**E**). Pull-off force of double printed composite fibers measured on smooth and rough surfaces, compared with a flat S-PSA control (**F**).

This led to an extremely high adhesion force of 200 mN due to the optimal and very homogeneous shape of the composite mushroom patterns, leading to 7 and 35 times further adhesion improvement compared with S-PSA mushroom and monolithic PDMS fibers, respectively (Fig. 3C). Notably, the combination of a thin S-PSA terminal layer together with sharp tip edges of the composite fibers is more beneficial than a thicker S-PSA terminal layer with rounded tip edges.

Our results show a three-fold adhesion increase for the DP composite fibers with 1 µm layer thickness which is in agreement with experimental and theoretical findings, where the effect of layer

thickness on the adhesion performance was investigated. For example, it was shown that the pull-off stress increased with decreasing the S-PSA film thickness; particularly, a two-fold increase of the pull-off stress was obtained for 50 µm thin films compared with 230 µm films (Fischer et al. 2017).

In other works, it was theoretically predicted that for very thin films, the critical pull-off stress scales with $(E/t)^{1/2}$, where E is the Young's modulus and t the thickness of the thin film. Therefore, the pull-off force is maximized for a thin layer with a low modulus (Chung and Chaudhury 2005). Similar results have been reported by employing finite element modeling. The pull off force increased when the thickness of a soft layer on a stiffer post decreased (Minsky and Turner 2015).

To compare the adhesion performance of our composite fibers to adhesives reported in literature, the adhesion stress of our DP composite mushroom fibers was calculated to be ca. 300 kPa. Recently, in a microscopic approach stiff mushroom fibers (diameter ca. 70–80, height 85–90µm) with a soft terminal layer of 4 and 7 µm thickness were studied and compared with the monolithic stiff fibers (Gorumlu and Aksak 2017). However, no significant difference on smooth surfaces was observed, since the adhesion decayed after the first measurement due to non-reversible fiber rupturing. Therefore, average adhesion values with ca. 77, 61, and 81 kPa were obtained for the monolithic, thin, and thick layer-coated mushroom patterns, respectively.

Finally, experiments were conducted to investigate the durability of our composite micropatterns. Both single printed (SP) and double printed composite fibers were subjected to cyclic adhesion experiments. The DP composite patterns exhibit a robust and high adhesion over more than 25 adhesion cycles, while the SP patterns show a decreased performance from 109 to 79 mN. Both composite patterns, SP and DP micropatterns, outperformed the film-terminated sample by two and seven times, respectively. Indeed, the adhesion of the DP patterns scattered slightly during the experiments. However, no gradual decrease could be observed and the adhesion performance recover within a few cycles. Microscopic observation showed that some fibers contacted each other upon strong stretching and quick releasing during the retraction of an adhesion cycle. However, the attachment was of temporary nature and fibers separated again within a few cycles and the adhesion performance was fully restored.

The gecko, our biological source of inspiration, showed a shear performance with two feet of ca. 90 kPa on a smooth surface (Irschick et al. 1996). Notably, the adhesion of the gecko foot-hairs is strongly coupled with an initial shear motion in order to reorient and align the adhesive tip-endings. Therefore, we compare our adhesives to the adhesion performance of the gecko under its optimal condition. Although our composite micropatterns surpass the performance of the gecko by three times on smooth surfaces, it is obvious that biological adhesive systems are developed for real world surfaces and enable animals to locomote over almost any surface, including rough surfaces. Initial experiments indicate that our composite micropatterns adhere to rough surfaces. Although the adhesion of DP composite fiber decreased from 217 to 39 mN, they outperform a flat S-PSA control sample with 28 mN on a rough surface (Fig. 3E and F). However, more experiments and detailed characterization need to be performed in the future.

In conclusion, we presented a novel approach for high-performance gecko-inspired adhesives. We demonstrated that microfibers with S-PSA mushroom tips outperform patterns with various tip geometries. The high adhesion strength of the composite microfibers was found to be due to the very thin S-PSA terminal tip layer and sharp tip edges, and thus improved load sharing. The optimal tip geometry and layer thickness, together with the covalent bonding enable high adhesion performance on smooth and rough surfaces with durability and repeatability, without any decay or irreversible deformation or fiber rupturing. Our concept of composite microfibrillar adhesives can provide significant benefits for a broad range of adhesion applications requiring high adhesion on various surfaces with different topographies. This includes wearable medical devices (Amjadi et al. 2016; Drotlef et al. 2017) enabling biocompatible and reversible adhesion to skin or other surfaces together with amplified signal transfer, transfer printing systems (Mengüç et al. 2012), and robotic manipulation (Song et al. 2017) capable of handling a wide range of complex and deformable objects.

Materials and methods

Fabrication of cylindrical microfibers decorated with different tip shapes

Cylindrical fibers

PDMS microfibers were obtained by replicating SU-8 lithographic templates as previously reported (del Campo et al. 2007). Sylgard 184 prepolymer and curing agent with weight ratio of 10:1 were mixed, degassed, and cast onto the SU-8 mold. The samples were cured in a vacuum oven at 90°C for 1 h and

then demolded. Micropatterns with 45 µm tip diameter, 55 µm spacing, and 89 µm height were obtained.

Microfibers decorated with hemispherical S-PSA tips

Skin adhesive MG 7-9900 (Dow Corning) prepolymer and curing agent with weight ratio of 1:1 were mixed and degassed for 2 min. Next, a thin and homogeneous layer of S-PSA precursor solution with 25–30 µm thickness was coated over a glass plate by a film applicator (Multicator 411, Erichsen GmbH & Co. KG). After partial crosslinking (pre-crosslinking) of the S-PSA layer for 8 min, the micropatterned PDMS was manually inked onto the thin layer and placed upside down in a petri dish. The S-PSA was fully crosslinked after 12 h at room temperature and micropatterns with 45 µm tip diameter, 55 µm spacing, and 101 µm height with hemispherical tips were obtained.

S-PSA mushroom fibers

A thin and homogeneous layer of S-PSA precursor solution with 25–30 µm thickness was coated over a glass plate by a film applicator. After partial crosslinking of the S-PSA layer for 8 min, the micropatterned PDMS was manually inked onto the thin layer and placed on a perfluorinated silicon wafer. The S-PSA was fully crosslinked after 12 h at room temperature and peeled-off. Mushroom-shaped microfibers with 62 µm tip diameter, 31 µm spacing, and 92 µm height were obtained.

Film-terminated microfibers decorated with S-PSA

A thin and homogeneous layer of S-PSA precursor solution with 25–30 µm thickness was coated over a PET film by a film applicator. The micropatterned PDMS was manually inked onto the thin layer, crosslinked for 12 h at room temperature, and peeled-off. Film-terminated micropatterns with 99 µm height were obtained. Please note that the PET film is required in order to facilitate the detachment of the cured film-terminated patterns.

VS mushroom fibers

A thin and homogeneous layer of the VS precursor solution with 25–30 µm thickness was coated over a glass plate by a film applicator. After partial crosslinking of the VS layer for 30–45 s, the micropatterned PDMS was manually inked onto the thin layer and placed on a perfluorinated silicon wafer. Within a few minutes, the viscous VS was crosslinked, peeled-off, and mushroom-shaped microfibers with ca. 65 µm tip diameter, 35 µm spacing, and 93 µm height were obtained.

It should be noted that we employed VS for the fabrication of the mushroom fiber tips due to its fast crosslinking kinetics and facile processing, enabling PDMS microstructures with optimal and homogenous mushroom fiber tips. The slow crosslinking kinetics and high temperature curing of the PDMS may cause imperfect mushroom tips, leading to inhomogeneous patterns.

SP composite mushroom fibers

A thin and homogeneous layer of S-PSA precursor solution with 25–30 µm thickness was coated over a glass plate by a film applicator. After partial crosslinking of the S-PSA layer for ca. 15–20 min, the VS mushroom pattern was manually inked onto the thin layer and printed on a perfluorinated silicon wafer. The S-PSA was fully crosslinked after 12 h at room temperature and peeled-off. Composite mushroom-shaped microfibers with 70 µm tip diameter, 30 µm spacing, and 96 µm height were obtained.

Double printed composite mushroom fibers

VS mushroom patterns were manually inked onto the thin layer of S-PSA as described before, printed on a perfluorinated silicon wafer for 5 s, peeled-off, and printed on a pristine perfluorinated silicon wafer. The S-PSA was fully crosslinked after 12 h at room temperature and peeled-off. Please note that after the first printing and peeling process, S-PSA material was transferred from the fiber tips to the silicon wafer resulting in a reduced terminal layer thickness of the composite fibers. Composite mushroom-shaped microfibers with 67 µm tip diameter, 33 µm spacing, and 95 µm height were obtained.

Flat S-PSA control

A thin and homogeneous layer of S-PSA precursor solution with 500 µm thickness was coated over a glass plate by a film applicator and fully crosslinked for 12 h at room temperature.

Experimental setup

A customized adhesion setup was built onto an inverted optical microscope (Axio Observer A1, Zeiss) with a video camera (Grasshopper®3, Point Grey Research Inc.) to visualize and record the contact interface. The adhesion force was recorded by a sensitive load cell (GSO-25, Transducer Techniques®) attached to a computer-controlled high-precision piezo motion stage (LPS-65 2″, Physik Instrumente GmbH & Co. KG) in *z*-direction. Fine positioning in *x*- and *y*-direction was done by a manual *xy*-stage (NFP-2462CC, Positionierungstechnik Dr Meierling) and tilt correction was adjusted by two goniometers

(M-GON65-U, Newport). Motion control of the piezo stages and the data acquisition were achieved by a customized Linux code (Ubuntu™, Canonical Ltd). The program allowed to control preloads, velocities, displacements in *x*- and *z*-directions, and contacting time.

Experimental procedure

Micropatterned samples were placed under a spherical glass probe with 4 mm radius. During the adhesion testing the indenter approached the sample surface at 50 µm/s and was first brought in contact with a preload of 50 mN. After a contact time of 10 s, the indenter was retracted at a speed of 50 µm/s until the probe was detached from the sample. The spherical indenter was cleaned after each measurement cycle with a particle-free tissue and isopropanol. The experiments were conducted in a temperature and humidity controlled lab and were in the range of 20–25°C and 25–35%, respectively. For each data point three samples with a minimum of five measurements were performed.

Acknowledgments

The authors thank Hamed Shahsavan for his fruitful discussions, Morteza Amjadi for reviewing the manuscript, Arda Soykal for helping with the fabrication, and Robert Radsziwill and Biesterfeld Spezialchemie GmbH (Hamburg, Germany) for providing the S-PSA and discussions. C.B.D. thanks the International Max Planck Research School for Intelligent Systems (IMPRS-IS) for his PhD fellowship.

Funding

This work was funded by the Max Planck Society.

References

Aksak B, Sahin K, Sitti M. 2014. The optimal shape of elastomer mushroom-like fibers for high and robust adhesion. Beilstein J Nanotechnol 5:630–8.

Amjadi M, Turan M, Clementson C, Sitti M. 2016. Parallel microcracks-based ultrasensitive and highly stretchable strain sensors. ACS Appl Mater Interfaces 8:5618–26.

Arzt E, Gorb S, Spolenak R. 2003. From micro to nano contacts in biological attachment devices. Proc Natl Acad Sci U S A 100:10603–6.

Autumn K, Liang YA, Hsieh ST, Zesch W, Chan WP, Kenny TW, Fearing R, Full RJ. 2000. Adhesive force of a single gecko foot-hair. Nature 405:681–5.

Autumn K, Sitti M, Liang YA, Peattie A, Hansen W, Sponberg S, Kenny T, Fearing R, Israelachvili J, Full RJ. 2002. Evidence for van der Waals attachment for geckos. Proc Natl Acad Sci U S A 99:12252–6.

Autumn K. 2006. In: Smith AM, Callow JA, editors. Properties, principles, and parameters of the gecko adhesive system. Biological adhesives. Berlin: Springer. p. 225.

Carbone G, Pierro E. 2012. Sticky bio-inspired micropillars: finding the best shape. Small 8:1449–54.

Chung JY, Chaudhury MK. 2005. Soft and Hard Adhesion. J Adhes 81:1119–45.

del Campo A, Greiner C, Álvarez I, Arzt E. 2007. Patterned surfaces with pillars with controlled 3D tip geometry mimicking bioattachment devices. Adv Mater 19:1973–7.

Del Campo A, Greiner C, Arzt E. 2007. Contact shape controls adhesion of bioinspired fibrillar surfaces. Langmuir 23:10235–43.

Drotlef DM, Amjadi M, Yunusa M, Sitti M. 2017. Bioinspired composite microfibers for skin adhesion and signal amplification of wearable sensors. Adv Mater 29:1701353–61.

Drotlef DM, Stepien L, Kappl M, Barnes J, Butt HJ, del Campo A. 2013. Insights into the adhesive mechanisms of tree frogs using artificial mimics. Adv Funct Mater 23:1137–46.

Drotlef DM, Blümler P, del Campo A. 2014. Magnetically actuated patterns for bioinspired reversible adhesion (dry and wet). Adv Mater 26:775–9.

Fischer SCL, Arzt E, Hensel R. 2017. Composite pillars with a tunable interface for adhesion to rough substrates. ACS Appl Mater Interfaces 9:1036–44.

Fischer SCL, Kruttwig K, Bandmann V, Hensel R, Arzt E. 2017. Adhesion and cellular compatibility of silicone-based skin adhesives. Macromol Mater Eng 302:1600526–11.

Ge L, Sethi S, Ci L, Ajayan PM, Dhinojwala A. 2007. Carbon nanotube-based synthetic gecko tapes. Proc Natl Acad Sci U S A 104:10792–5.

Gorumlu S, Aksak B. 2017. Sticking to rough surfaces using functionally graded bio-inspired microfibres. R Soc Open Sci 4:161105.

Greiner C, del Campo A, Arzt E. 2007. Adhesion of bioinspired micropatterned surfaces: effects of pillar radius, aspect ratio, and preload. Langmuir 23:3495–502.

Irschick DJ, Austin CC, Petren K, Fisher RN, Losos JB, Ellers O. 1996. A comparative analysis of clinging ability among pad-bearing lizards. Biol J Linn Soc 59:21–35.

Kim S, Sitti M. 2006. Biologically inspired polymer microfibers with spatulate tips as repeatable fibrillar adhesives. Appl Phys Lett 89:261911–3.

Marvi H, Song S, Sitti M. 2015. Experimental investigation of optimal adhesion of mushroomlike elastomer microfibrillar adhesives. Langmuir 31:10119–24.

Mengüç Y, Yang SY, Kim S, Rogers JA, Sitti M. 2012. Gecko-inspired controllable adhesive structures applied to micromanipulation. Adv Funct Mater 22:1246–54.

Minsky HK, Turner KT. 2015. Achieving enhanced and tunable adhesion via composite posts. Appl Phys Lett 106:201604.

Murphy MP, Aksak B, Sitti M. 2009. Gecko-inspired directional and controllable adhesion. Small 5:170–5.

Peisker H, Michels J, Gorb SN. 2013. Evidence for a material gradient in the adhesive tarsal setae of the ladybird beetle *Coccinella septempunctata*. Nat Commun 4:1661–7.

Prowse MS, Wilkinson M, Puthoff JB, Mayer G, Autumn K. 2011. Effects of humidity on the mechanical properties of gecko setae. Acta Biomater 7:733–8.

Puthoff JB, Prowse MS, Wilkinson M, Autumn K. 2010. Changes in materials properties explain the effects of humidity on gecko adhesion. J Exp Biol 213:3699–704.

Shahsavan H, Zhao B. 2014. Bioinspired functionally graded adhesive materials: synergetic interplay of top viscous-elastic layers with base micropillars. Macromolecules 47:353–64.

Song S, Drotlef DM, Majidi C, Sitti M. 2017. Controllable load sharing for soft adhesive interfaces on three-dimensional surfaces. Proc Natl Acad Sci U S A 114:E4344–53.

Spolenak R, Gorb S, Gao HJ, Arzt E. 2005. Effects of contact shape on the scaling of biological attachments. Proc R Soc Lond Ser A 461:305–19.

Appendix B. The Effect of Substrate Wettability and Modulus on Gecko and Gecko-inspired Synthetic Adhesion in Variable Temperature and Humidity

This appendix includes the following publication:

1. Christopher T. Mitchell*, **Cem Balda Dayan***, Dirk-Michael Drotlef, Metin Sitti, and Alyssa Y. Stark, The effect of substrate wettability and modulus on gecko and gecko-inspired synthetic adhesion in variable temperature and humidity. *Scientific Reports*, 2020, doi: 10.1038/s41598-020-76484-6.

* Equally contributing co-first authors

scientific reports

Check for updates

OPEN

The effect of substrate wettability and modulus on gecko and gecko-inspired synthetic adhesion in variable temperature and humidity

Christopher T. Mitchell[1,3], Cem Balda Dayan[2,3], Dirk-M. Drotlef[2], Metin Sitti[2] & Alyssa Y. Stark[1]✉

Gecko adhesive performance increases as relative humidity increases. Two primary mechanisms can explain this result: capillary adhesion and increased contact area via material softening. Both hypotheses consider variable relative humidity, but neither fully explains the interactive effects of temperature and relative humidity on live gecko adhesion. In this study, we used live tokay geckos (*Gekko gecko*) and a gecko-inspired synthetic adhesive to investigate the roles of capillary adhesion and material softening on gecko adhesive performance. The results of our study suggest that both capillary adhesion and material softening contribute to overall gecko adhesion, but the relative contribution of each depends on the environmental context. Specifically, capillary adhesion dominates on hydrophilic substrates, and material softening dominates on hydrophobic substrates. At low temperature (12 °C), both capillary adhesion and material softening likely produce high adhesion across a range of relative humidity values. At high temperature (32 °C), material softening plays a dominant role in adhesive performance at an intermediate relative humidity (i.e., 70% RH).

The gecko adhesive system has sparked intense research and innovation for more than two decades[1–15]. However, despite significant interest in the morphology, evolutionary history, and biomechanical principles of the gecko adhesive system, there is still uncertainty about the governing mechanisms of gecko adhesion. Specifically, the potential roles of capillary adhesion and material softening on gecko adhesive performance in humid environments have often been debated[16–20]. Habitat diversity of geckos suggests that geckos must maintain adhesion in a variety of contexts, including hot and humid tropical environments[21–25], thus understanding the adhesive mechanism in these conditions may be key to understanding diversification of the gecko adhesive system.

Geckos use microscopic, hair-like structures (setae) to amplify attractive van der Waals forces of the superhydrophobic adhesive toe pads[1,26–32]. Although a van der Waals-based adhesive system creates a robust and reversible adhesive force, common environmental factors may disrupt the functionality of the system. For example, thin water layers have the potential to reduce van der Waals forces to zero when separating setae from a substrate by as a little as 20 nm[33]. Despite this, gecko adhesion increases as thin water layer thickness from ambient relative humidity (RH) increases[16–19,34]. Two hypotheses have been proposed to explain this result: capillary adhesion and material softening. Gecko adhesion increases as the substrate becomes more hydrophilic, supporting the hypothesis that capillary bridges between gecko setae and the water-attracting substrate enhance adhesion[16–18]. Likewise, at high humidity (> 70% RH) the setal material (primarily keratin associated proteins and lipids[35–38]) softens, supporting the hypothesis that soft setae increase the interfacial contact area and subsequently increase van der Waals forces[19,20]. The results of these studies are difficult to reconcile[14,34,39], and none consider the possibility that capillary adhesion and material softening are not mutually exclusive.

In addition to fluctuations in RH, other environmental factors may also alter gecko adhesive performance. For instance, ectothermic geckos may be particularly susceptible to variation in temperature due to potential limitations on muscle and kinematic performance[40–42]. However, body temperature independently has no effect

[1]Department of Biology, Villanova University, 800 E. Lancaster Ave., Villanova, PA 19085, USA. [2]Physical Intelligence Department, Max Planck Institute for Intelligent Systems, 70569 Stuttgart, Germany. [3]These authors contributed equally: Christopher T. Mitchell and Cem Balda Dayan. ✉email: alyssa.stark@villanova.edu

on live gecko adhesion[43,44]. Instead, gecko adhesive performance is strongly related to ambient temperature when tested across a range of RH[34,39]. Specifically, at low temperature (12 °C), gecko adhesion increases with increasing RH[34], supporting results from separated setae tested at room temperature[16,19]. However, at high temperature (32 °C), RH has no effect on live gecko adhesion[34]. A nanoscopic length scale model attempted to explain the temperature dependency of this relationship, but ultimately the coupled effects of RH and temperature on gecko adhesion are still undetermined[39].

Live gecko adhesion results and setal adhesion models in variable temperature and RH do not fully support either of the current hypotheses that explain gecko adhesion in variable RH (i.e., capillary adhesion, material softening). The purpose of this study is to decouple these hypotheses by testing the adhesive performance of live geckos and a gecko-inspired synthetic adhesive (GSA) model in variable temperature and RH conditions, and to consider that these hypotheses may not be mutually exclusive. To test our hypothesis, we used live geckos and GSAs because live gecko setal surface chemistry and modulus change in wet environments[20,35,45], and GSA surface chemistry and modulus remains relatively constant. Thus, the qualitative comparison between live gecko and GSA adhesive performance in the same conditions allows us to explore the influence of capillary adhesion and material softening with and without confounding factors innate to the live animal system. We hypothesize that both capillary adhesion and material softening play a role in live gecko and GSA performance (i.e., are not mutually exclusive), and that these roles change dominance depending on environmental conditions (i.e., substrate wettability, adhesive material modulus, temperature, RH).

To test for an effect of capillary adhesion on gecko adhesive performance, we measured shear adhesive performance of live geckos and GSAs in variable temperature and RH conditions on hydrophobic [octadecyltrichlorosilane-self assembled monolayer (OTS-SAM) coated glass] and hydrophilic (untreated glass) substrates, which limit or support capillary adhesion, respectively. To explore the role of setal stiffness on gecko adhesive performance in variable temperature and RH conditions, we replicated our live gecko and GSA experiments with two additional GSAs that were either soft or stiff. Here, we compared adhesive performance of the model GSAs with artificially defined stalk modulus (soft, medium, stiff) across varying conditions (i.e., temperature, RH, substrate wettability). The results of this study improve our understanding of the gecko adhesive mechanism and gecko ecology related to the interaction of adhesive performance and relevant abiotic environmental conditions like temperature, RH, and substrate wettability.

Results

Shear adhesion of live geckos and GSAs differed in response to temperature, RH, substrate wettability, and modulus (GSAs only). Of all possible interactions for each system (live gecko, GSA), only four two-way statistical interactions were significant. These are discussed below. All statistical results [i.e., F values (F), degrees of freedom (subscript numerical values), p value (p); Tables S1 and S2] and model considerations (i.e., tests for homogeneity of variance; Tables S3 and S4) are reported below and in the Supplementary Material. Means of the treatment groups were deemed different from one another only when the p value calculated from the statistical model was $p \leq 0.05$.

Effect of relative humidity and substrate wettability. Gecko and GSA shear adhesion differed in response to the interaction between RH and substrate wettability ($F_{3,90} = 5.096$, $p = 0.0026$; $F_{3,180} = 5.638$, $p = 0.0010$, respectively; Tables S1 and S2). On the hydrophilic untreated glass, live gecko and GSA shear adhesion increased between 30 and 55% RH. Gecko and GSA shear adhesion remained constant on glass at > 55% RH (Fig. 1). On the hydrophobic OTS-SAM coated glass, live gecko shear adhesion increased at ≥ 70% RH, while GSA adhesion was unaffected by RH (Fig. 1).

Effect of relative humidity and temperature. Gecko and GSA shear adhesion differed in response to the interaction between RH and temperature ($F_{3,90} = 10.190$, $p < 0.0001$; $F_{3,180} = 5.828$, $p = 0.0008$, respectively; Tables S1 and S2). In general, at low temperature (12 °C), gecko shear adhesion increased as RH increased. Similarly, GSA shear adhesion increased as RH increased, except that the increase occurred between 30 and 55% RH, and shear adhesion of all subsequent set points did not differ (Fig. 2). At high temperature (32 °C), gecko shear adhesion showed a slight peak at 70% RH, while GSA adhesion was unaffected by RH at 32 °C (Fig. 2).

Effect of modulus and substrate wettability. Shear adhesion of GSAs with artificially defined stalk modulus (soft, medium, stiff) differed in response to the interaction between GSA pillar stiffness and substrate wettability ($F_{2,180} = 24.610$, $p < 0.0001$; Table S2). On the hydrophilic glass, modulus had no effect on GSA shear adhesion. However, on the hydrophobic OTS-SAM coated glass, shear adhesion of the medium modulus GSA was higher than the stiff and soft modulus GSAs (Fig. 3).

Effect of temperature and substrate wettability. Shear adhesion of live geckos differed in response to the interaction between temperature and substrate wettability ($F_{1,90} = 32.040$, $p < 0.0001$; Table S1). On the hydrophilic glass, gecko shear adhesion at 12 °C was 60% higher than shear adhesion at 32 °C. On the hydrophobic OTS-SAM coated glass, gecko shear adhesion at 12 °C was only 12% higher than shear adhesion at 32 °C (Fig. S1). Overall, gecko shear adhesion on the OTS-SAM coated glass was lower than shear adhesion on untreated glass.

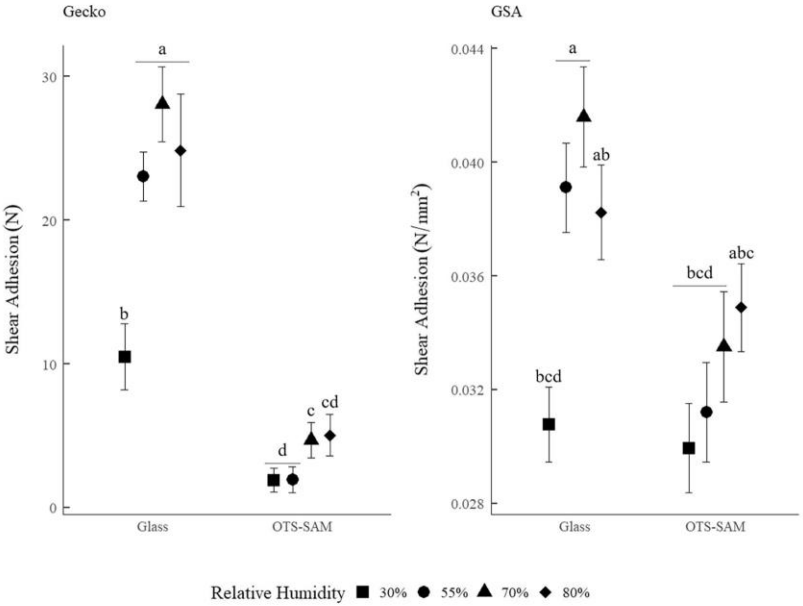

Figure 1. Tokay gecko (*Gekko gecko*; sample size = 7; left panel) and gecko-inspired synthetic adhesive (GSA; sample size = 5; right panel) shear adhesion (mean ± s.e.m.) in variable relative humidity (30%, 55%, 70%, and 80%) on hydrophilic (ca. 50° water contact angle) glass and hydrophobic (ca. 100° water contact angle) octadecyltrichlorosilane self-assembled monolayer (OTS-SAM) coated glass. Shear adhesion of live geckos is measured as maximum shear force resisted before sliding (N) and shear adhesion of GSAs is measured as maximum shear force resisted while sliding per unit area (N/mm^2), matching previous work[34,47]. The means of treatment groups denoted with the same letter are not statistically different from one another according to Tukey post hoc pairwise statistical tests (see Tables S1 and S2 for a detailed explanation of statistical analysis and the model output).

Discussion

Geckos are extremely diverse (i.e., > 1800 species[13]) and live in a multitude of habitats with a wide variety of environmental conditions (e.g., hot, humid, cool, dry). Despite significant interest in geckos, it is unclear how the gecko adhesive system simultaneously manages variation in ambient temperature and RH. Specifically, experimental results and computational models of single seta and setal array adhesion in variable RH suggest that either capillary adhesion or material softening explain gecko adhesive performance[16–20]. However, neither of these hypotheses fully explain gecko adhesion in variable RH and temperature, and they are not necessarily mutually exclusive[34,39]. Indeed, the results of this study suggest that in variable RH and temperature, both capillary adhesion and material softening influence gecko adhesion. Our results highlight several key interactions among temperature, RH, substrate wettability, and modulus in live gecko and GSA systems. These interactions are discussed below.

Effect of relative humidity and substrate wettability. On hydrophilic glass, gecko adhesion and GSA adhesion are consistent and match adhesion behavior of other polymer GSAs in variable RH[46–48]. Using a GSA as a control for material softening and surface chemistry (i.e., GSAs experience little relative change in modulus and surface chemistry as function of water[49]), it is clear both systems are significantly influenced by capillary adhesion on hydrophilic glass (i.e., adhesion is higher at 70% RH than at 30% RH), similar to studies testing single setae and setal tips (spatula)[16,17]. On hydrophobic OTS-SAM coated glass, where we expect RH-induced water layers and thus capillary adhesion to be limited, GSA adhesion is unaffected by RH. Conversely, gecko adhesion generally increased at higher RH (70% and 80% RH; Fig. 1). This discontinuity highlights likely interactive effects of capillary adhesion and material softening in the gecko adhesive system. Specifically, the softening of gecko setae (material softening hypothesis) occurs on both hydrophilic and hydrophobic substrates at high RH (i.e., gecko setae soften at > 70% RH regardless of substrate[19,20]). However, the measurable increase in live gecko adhesion due to increased contact area from material softening (though changes in setal surface

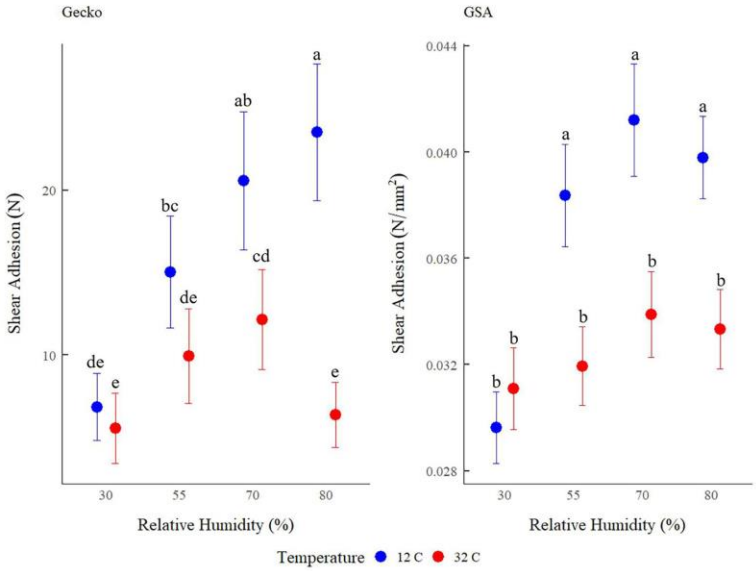

Figure 2. Tokay gecko (*Gekko gecko*; sample size = 7; left panel) and gecko-inspired synthetic adhesive (GSA; sample size = 5; right panel) shear adhesion (mean ± s.e.m.) in variable relative humidity (30%, 55%, 70%, and 80%) and temperature (12 °C and 32 °C). Shear adhesion of live geckos is measured as maximum shear force resisted before sliding (N) and shear adhesion of GSAs is measured as maximum shear force resisted while sliding per unit area (N/mm²), matching previous work[34,47]. The means of treatment groups denoted with the same letter are not statistically different from one another according to Tukey post hoc pairwise statistical tests (see Tables S1 and S2 for a detailed explanation of statistical analysis and the model output).

chemistry cannot be ruled out) at high RH appears to only be detectable when capillary adhesion is discouraged by substrate wettability (i.e., OTS-SAM coated glass).

Effect of relative humidity and temperature. In general, at low temperature (12 °C), gecko and GSA adhesive performance increases as RH increases[34,47]. Because the GSA is not significantly affected by changes in modulus or surface chemistry, capillary adhesion appears to drive this response in low temperature. However, at high temperature (32 °C), gecko adhesion peaks at 70% RH, which was not detected previously[34] and not observed in the GSA system (Fig. 2). Thus, the difference between gecko adhesive performance and GSA adhesive performance at high temperature likely signifies that either changes in setal surface chemistry or modulus are responsible for the observed enhancement of live gecko adhesion at high temperature and intermediately high RH (Fig. 2).

Effect of modulus and substrate wettability. On hydrophilic glass, there is no statistical difference in GSA adhesive performance as a function of stalk modulus. However, the pairwise comparisons of adhesion on glass between soft and stiffer GSAs is nearly different in one instance (i.e., soft-medium GSA comparison p value is nearly $p \leq 0.05$; soft-stiff: $p = 0.1068$; soft-medium: $p = 0.0958$). On hydrophobic OTS-SAM coated glass, shear adhesion of the medium GSA is higher than the soft and the stiff GSAs, suggesting that when capillary adhesion is ineffective (i.e., highly reduced water layers), stalk modulus significantly impacts adhesive performance and moderately soft stalks perform better. The difference in shear adhesive performance between the medium and stiff GSAs on hydrophobic OTS-SAM coated glass, but not hydrophilic glass, is significant given similarities between the GSA and gecko adhesive systems. Specifically, the modulus of gecko setae in humid conditions (i.e., 80% RH) is ca. 40% lower than the modulus of gecko setae in dry conditions[20]. In this experiment, we matched GSA modulus to live gecko modulus changes such that the modulus of the medium GSA is 40% lower than the modulus of the stiff GSA. Thus, the results of the GSA experiment support our observations in live geckos, and both systems are likely optimized for higher adhesion with moderately stiff stalks on hydrophobic but not hydrophilic substrates. This result highlights the importance of material properties on hydrophobic substrates that limit capillary adhesion.

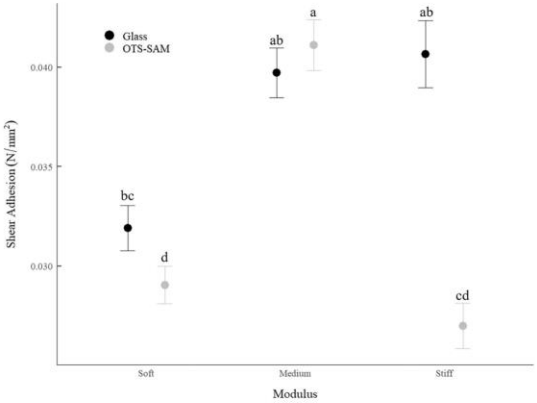

Figure 3. Shear adhesion (mean ± s.e.m.) of three gecko-inspired synthetic adhesives (GSAs; sample size = 5) with different modulus values (soft = 0.093 ± 0.0047 (s.d.) MPa; medium = 0.83 ± 0.020 (s.d.) MPa; stiff = 1.91 ± 0.140 (s.d.) MPa) on hydrophilic (ca. 50° water contact angle) glass and hydrophobic (ca. 100° water contact angle) octadecyltrichlorosilane self-assembled monolayer (OTS-SAM) coated glass. The means of treatment groups denoted with the same letter are not statistically different from one another according to Tukey post hoc pairwise statistical tests (see Table S2 for a detailed explanation of statistical analysis and the model output).

On both hydrophobic and hydrophilic substrates, it is likely the slightly lower shear adhesion of the soft GSA is related to contact mechanics. Specifically, maximum shear adhesion of the stiff GSA is followed by a rapid decrease in tip contact, whereas maximum shear adhesion of the soft GSA is achieved incrementally as pillars buckle and slide. This suggests that very stiff stalks are "stiction" dominated (i.e. pillar adhesion drives overall shear adhesive performance), and very soft stalks are friction dominated (i.e. pillar adhesion is insignificant in comparison to the friction created by buckled stalks)[27]. The difference in shear adhesive performance between soft and stiff stalks is likely why gecko setae are not soft (i.e., avoid buckling, higher adhesive performance)[19,20].

Conclusion

The results of this study suggest that when geckos interact with environmental substrates that facilitate the formation of RH-induced water layers (i.e., hydrophilic substrates), capillary adhesion enhances adhesion (between 30–80% RH). When geckos interact with environmental substrates that do not facilitate the formation of RH-induced water layers (i.e., hydrophobic substrates), material softening enhances adhesion. Likewise, at low temperature, capillary adhesion influences gecko and GSA adhesive performance, but at high temperature material softening plays an important role. Taken together, these results show that capillary adhesion and material softening are important, highly contextual and non-mutually exclusive mechanisms geckos experience to enhance adhesion in particular circumstances. Although capillary adhesion appears to play a more dominate role in adhesive performance, few natural substrates are as hydrophilic as glass. Thus, functionally, it is likely geckos moving on hydrophobic leaves in high temperature and RH take advantage of slightly softer, more compliant setae that enhance adhesion at 32 °C, 70% RH, which are common climatic conditions in the tropics. Future work should explore adhesive performance of geckos native to drier and/or cooler climates to determine if this optimal peak is only found in tropical-dwelling geckos like the Tokay gecko (*Gekko gecko*) tested here. Likewise, the effect of setal surface chemistry is poorly understood, and may be an additional mechanism that geckos from multiple climates utilize to vary adhesive performance in complex environmental conditions.

Materials and methods

Experimental conditions. All gecko and GSA adhesion tests were conducted in a walk-in environmental chamber (Hotpack SP Scientific; Warminster, Pennsylvania, USA) with temperature and RH control (maintained at ± 2.0 °C and ± 5.0% RH of the set point). Two temperature and four RH set points (temperature: 12 °C and 32 °C; RH: 30%, 55%, 70%, and 80%) were used to create eight different experimental set point combinations, matching previous studies[34,47]. Experimental substrates and GSA samples were exposed to temperature and RH set points for 30 min prior to testing. Live geckos were acclimated for one hour to temperature and RH set points.

Experimental substrates. Geckos and GSAs were tested on hydrophilic glass and hydrophobic octadecyltrichlorosilane-self assembled monolayer (OTS-SAM) coated glass (advancing contact angle = 100.1° ± 2.40 (s.d.), receding contact angle = 79.8° ± 1.58 (s.d.) for deionized water; s.d. = standard deviation). The OTS-SAM coated glass was made using a glass panel or a glass block (for GSA experiment) that was washed multiple times with deionized water and isopropyl alcohol. The glass was dried with nitrogen gas between each rinse. After preliminary rinses, the glass was soaked in a base bath for 3 h, rinsed with deionized water, and dried with nitrogen gas. The glass was then fully immersed in the OTS solution (1 mM of OTS in toluene) for 30 min. The container holding the solution and immersed glass was sealed to minimize atmospheric contact. After removing the substrate, a series of consecutive rinses were completed with toluene, acetone, chloroform, and isopropyl alcohol. Nitrogen gas was used to dry the substrate between each rinse. Finally, the substrates were left in a vacuum oven (ca. 150 °C) overnight to anneal. This process is described in more detail elsewhere (see SI Section 1 in[50]).

Live animal adhesion experiments. Seven adult Tokay geckos (*G. gecko*) (body mass = 82.1 ± 17.35 g s.e.m.; s.e.m. = standard error mean) were obtained from California Zoological Supply and housed in the laboratory. Detailed husbandry and experimentation procedure has been reported previously[34]. Briefly, geckos were induced to securely position each foot on hydrophilic glass (56 × 33 cm panel) or hydrophobic OTS-SAM coated glass (25 × 15 cm panel) so that each toe pad was in full adhesive contact. We measured maximum shear adhesion, defined as the maximum shear adhesive force (N) a gecko can withstand before sliding. To measure maximum shear adhesion, geckos were harnessed around the pelvis with a thin flexible harness attached to a force sensor (Nidec Shimpo FGV-XY 100 N force gauge; Itasca, Illinois, USA) supported by a custom-built motorized apparatus (see[34] for an example schematic). Geckos were pulled parallel to the vertical substrate at a constant rate (1.8 mm s^{-1}) until all four feet begin to slide. The point where all four feet slip was logged as maximum shear adhesion and the trial was concluded. Maximum shear adhesion was measured three consecutive times for all geckos, however only the maximum shear adhesive force of the three trials was used in data analysis. In some trials, shear adhesive force was high and resulted in detachment of setae from the animal. If this occurred, all subsequent trials were discontinued, and the highest shear adhesive force value was used for analysis. After each adhesion test the substrate was cleaned with ethanol, then deionized water, and dried using a Kimtech wipe. Geckos were tested at a single environmental set point (temperature, RH) on a single substrate (hydrophilic or hydrophobic) per day. Geckos were given a minimum of 48 h to rest between trials. All geckos were randomly tested on each of the two types of substrates (hydrophilic and hydrophobic) at all eight experimental set points. A total of 112 data points were collected for live gecko experiments. Experimental procedure and housing of live geckos was in accordance with IACUC-1874 and IACUC-1878 (issued by Villanova University Institutional Animal Care and Use Committee). All methods were carried out in accordance with relevant guidelines and regulations.

GSA fabrication and characterization. Mushroom GSAs (70 µm tip diameter, 50 µm stalk diameter, 50 µm stalk spacing, 100 µm pitch distance, 60 µm stalk height) were fabricated using a combination of soft molding techniques described elsewhere[51]. Samples with three characteristic stalk modulus states were obtained: soft, medium, and stiff. The soft GSA microfiber stalks were made with Ecoflex-00-30 and SU-8 lithographic templates. The prepolymer and curing agent were mixed (weight ratio of 1A:1B), degassed, and cast onto the SU-8 mold. The samples were cured at room temperature (23 °C) for 4 h and then demolded. Modulus of the soft GSA stalk material was 0.093 ± 0.0047 (s.d.) MPa and the static contact angle of the flat, non-structured cured Ecoflex-00-30 was 103.3° ± 2.13 (s.d.; using DI water). The medium GSA microfiber stalks were made with a mixture of PDMS (polydimethylsiloxane, Sylgard 184; weight ratio of 10:1) and Ecoflex-00-30 (weight ratio of 1A:1B; 80% and 20% by weight respectively). The mixture was degassed and cast onto the SU-8 lithographic templates. The samples were cured at 65 °C for 24 h and then demolded. The medium GSA stalk material modulus was 0.83 ± 0.020 (s.d.) MPa and the static contact angle of the flat, non-structured cured PDMS-Ecoflex mixture was 105.1° ± 2.35 (s.d.; using DI water). Finally, the stiff GSA microfiber stalks were made with PDMS and SU-8 lithographic templates. The pre-polymer and curing agent were mixed (weight ratio of 10:1), degassed, and cast onto the SU-8 mold. The samples were cured in a vacuum oven at 90 °C for 1 h and then demolded. The modulus of the stiff GSA stalk material was 1.91 ± 0.140 (s.d.) MPa and the static contact angle of the flat, non-structured cured PDMS was 105.0° ± 0.47 (s.d.; using DI water).

Mushroom-tip fabrication was identical for all three GSA stalk moduli used in this experiment. Specifically, a thin, homogeneous layer of vinyl siloxane (VS; Kulzer, Flexitime Medium Flow) precursor solution was coated over a glass plate by a film applicator (25–30 µm thickness). After partial crosslinking of the VS layer for 30–45 s, the micropatterned fibrillar patch (described above) was manually inked onto the thin layer and placed on a perfluorinated silicon wafer. Within a few minutes the viscous VS was crosslinked, peeled-off, and mushroom-shaped microfibers were created. DI water static contact angle of flat, non-structured VS was 13.5° ± 2.97 (s.d.). Although stalk modulus differed among GSA samples, the mushroom tips of the pillars were all made of VS and stiffer (modulus = 2.4 ± 0.09 (s.d.) MPa) than the stalk modulus of all three sample types. This ensured that the surface chemistry and contact mechanics of the adhesive contact interface did not change among samples[52], nor were there additional contact mechanic consequences from different modulus gradients along the tip and stalks (i.e. the tips were always stiffer than the stalks)[53,54]. Varying only stalk modulus explores the mechanical consequences of the material softening hypothesis at the scale of the setal stalk, rather than the contact interface.

GSA fabrication and target moduli were achieved in accordance with previous work[55]. All modulus characterizations were measured using ISO527-2-type5b standards[55,56]. Stress–strain measurements were conducted with an Instron 5942 universal tensile tester (Norwood, MA, USA) set at a velocity of 200 µm s^{-1}. Mechanical characterization was also measured on materials aged 2 months in the laboratory to test for an effect of aging

on PDMS 10:1, Ecoflex 00–30, and PDMS—Ecoflex 00-30 mixture. There was no difference in the modulus of samples measured 1 day and 2 months after fabrication (Fig. S2).

Sessile drop measurements using a Krüss DSA100S goniometer (Hamburg, Germany) were used to measure the static water contact angle of experimental and sample substrates. In these characterizations, a ca. 2 µL deionized water droplet was deposited on the surface using a flat end needle (Sterican, 0.40 × 25 mm, Blunt Gauge 27). The DI water droplet was kept on the surface for 60 s. During this time, the images and measurements of the droplet were taken at 10 frames per seconds (fps) using a side-mounted camera. The average of the static contact angles was measured and calculated by goniometer software. For each sample, at least 10 different measurements were collected. Mechanical and static contact angle characterizations were conducted at room temperature (ca. 23 °C).

GSA adhesion experiments. Square soft, medium, and stiff GSA samples (14.4 ± 1.89 (s.e.m.) mm^2) were cut with a fine scalpel and glued to a clean glass microscope slide using silicon-based glue (Sil-Poxy; Macungie, Pennsylvania, USA). Samples were visually inspected using a dissecting microscope to ensure glue did not cover any part of the sample. Samples were dried for at least 24 h. Adhesion tests were conducted on the custom-built motorized apparatus described above with a force sensor (Nidec Shimpo XY 5 N force gauge; Itasca, Illinois, USA). The sample slide was attached to the experimental platform using double sided tape. A 106 g, 8 × 5 cm glass block or OTS-SAM coated glass block was placed on top of the sample, connected to the force gauge with a nylon string, and pulled in the shear direction at a constant rate (1.8 mm s^{-1}), similar to previous studies[27,47]. Only the maximum shear force (N) recorded over a single 3 cm shear slide was used for data analysis. Maximum shear force of GSAs was then divided by individual sample area (N/mm^2), in accordance with the previous work[27,47]. After each trial, the experimental substrate blocks were cleaned with ethanol, then deionized water, and dried using a Kimtech wipe. We tested shear adhesion of GSAs on each of the two types of substrates (hydrophilic and hydrophobic) at all eight temperature and RH set points. Five samples were used for each of the three modulus values (i.e., 15 total samples). Each sample was tested 16 times which generated 240 data points. Samples were tested between 3 and 16 months post fabrication. Sample test order and treatment was randomized to account for potential effects of PDMS ageing[57]. However, due to experimental constraints, all GSA trials conducted at 12 °C and 30% RH were tested last (i.e., sample order but not treatment order was randomized).

Statistical analysis. We used a generalized linear mixed model (GLMM) to test the effect of temperature, RH, and substrate wettability on live gecko adhesive performance. Individual gecko identification number was used as a random factor. Bartlett's test for homogeneity of variance on all explanatory variables (Table S3) showed heterogeneity between the two substrate wettability levels (hydrophilic and hydrophobic; $K^2 = 7.351$, $p = 0.006073$). Therefore, we included a variance structure (*varIndent*) that allows for differences in the variances of adhesion of the two substrates. Data were natural log transformed to normalize the residuals of the model (Shapiro–Wilk test: $W = 0.9847$, $p = 0.2298$).

We also used a GLMM to test the effect of temperature, RH, substrate wettability, and modulus on adhesive performance of GSAs. Individual GSA sample identification number was included as a random factor. Bartlett's test for homogeneity of variance on all explanatory variables (Table S4) showed heterogeneity between the three modulus levels (soft, medium, and stiff; $K^2 = 28.94$, $p < 0.0001$). Therefore, we included a variance structure (*varIndent*) that allows for differences in the variances of soft, medium, and stiff GSA adhesion. Adhesion data were natural log transformed to normalize the residuals of the model (Shapiro–Wilk test: $W = 0.9930$, $p = 0.3130$).

GLMM models and HSD Tukey pairwise comparisons were carried out using the R packages *nlme*[58] and *emmeans* respectively[59]. Statistical analyses and graphs were executed in *R*[60].

Data availability

All data generated and analyzed for this study are included in this published article and its Supplementary Material files.

Received: 14 July 2020; Accepted: 28 October 2020
Published online: 12 November 2020

References

1. Autumn, K. *et al.* Evidence for van der Waals adhesion in gecko setae. *Proc. Natl. Acad. Sci. US* **99**, 12252–12256 (2002).
2. Autumn, K., Niewiarowski, P. H. & Puthoff, J. B. Gecko adhesion as a model system for integrative biology, interdisciplinary science, and bioinspired engineering. *Annu. Rev. Ecol. Evol. Syst.* **45**, 445–470 (2014).
3. Sitti, M. & Fearing, R. S. Synthetic gecko foot-hair micro/nano-structures as dry adhesives. *J. Adhes. Sci. Technol.* **17**, 1055–1073 (2003).
4. Kim, S. & Sitti, M. Biologically inspired polymer microfibers with spatulate tips as repeatable fibrillar adhesives. *Appl. Phys. Lett.* **89**, 261911 (2006).
5. Murphy, M. P., Aksak, B. & Sitti, M. Gecko-inspired directional and controllable adhesion. *Small* **5**, 170–175 (2009).
6. Murphy, M. P., Kim, S. & Sitti, M. Enhanced adhesion by gecko-inspired hierarchical fibrillar adhesives. *ACS Appl. Mater. Interfaces* **1**, 849–855 (2009).
7. Glass, P., Chung, H., Washburn, N. R. & Sitti, M. Enhanced wet adhesion of elastomeric micro-fiber arrays with mushroom tip geometry and a photopolymerized p(DMA-co-MEA) tip coating. *Langmuir* **26**, 17357–17362 (2010).
8. Mengüç, Y., Röhrig, M., Abusomwan, U., Hölscher, H. & Sitti, M. Staying sticky: Contact self-cleaning of gecko-inspired adhesives. *J. R. Soc. Interface* **11**, 20131205 (2014).
9. Song, S. & Sitti, M. Soft grippers using micro-fibrillar adhesives for transfer printing. *Adv. Mater.* **26**, 4901–4906 (2014).
10. Niewiarowski, P. H., Stark, A. Y. & Dhinojwala, A. Sticking to the story: Outstanding challenges in gecko-inspired adhesives. *J. Exp. Biol.* **219**, 912–919 (2016).

11. Drotlef, D.-M., Amjadi, M., Yunusa, M. & Sitti, M. Bioinspired composite microfibers for skin adhesion and signal amplification of wearable sensors. *Adv. Mater.* **29**, 1701353 (2017).
12. Song, S., Drotlef, D.-M., Majidi, C. & Sitti, M. Controllable load sharing for soft adhesive interfaces on three-dimensional surfaces. *Proc. Natl. Acad. Sci.* **114**, E4344–E4353 (2017).
13. Russell, A. P., Stark, A. Y. & Higham, T. E. The integrative biology of gecko adhesion: Historical review, current understanding, and grand challenges. *Integr. Comp. Biol.* **59**, 101–116 (2019).
14. Stark, A. Y. & Mitchell, C. T. Stick or slip: Adhesive performance of geckos and gecko-inspired synthetics in wet environments. *Integr. Comp. Biol.* **59**, 214–226 (2019).
15. Liimatainen, V., Drotlef, D.-M., Son, D. & Sitti, M. Liquid-superrepellent bioinspired fibrillar adhesives. *Adv. Mater.* **32**, 2000497 (2020).
16. Huber, G. *et al.* Evidence for capillarity contributions to gecko adhesion from single spatula nanomechanical measurements. *Proc. Natl. Acad. Sci. US* **102**, 16293–16296 (2005).
17. Sun, W., Neuzil, P., Kustandi, T. S., Oh, S. & Samper, V. D. The nature of the gecko lizard adhesive force. *Biophys. J.* **89**, L14–L17 (2005).
18. Kim, T. W. & Bhushan, B. The adhesion model considering capillarity for gecko attachment system. *J. R. Soc. Interface* **5**, 319–327 (2008).
19. Puthoff, J. B., Prowse, M. S., Wilkinson, M. & Autumn, K. Changes in materials properties explain the effects of humidity on gecko adhesion. *J. Exp. Biol.* **213**, 3699–3704 (2010).
20. Prowse, M. S., Wilkinson, M., Puthoff, J. B., Mayer, G. & Autumn, K. Effects of humidity on the mechanical properties of gecko setae. *Acta Biomater.* **7**, 733–738 (2011).
21. Bauer, A. M. & Good, D. A. Phylogenetic systematics of the day geckos, genus, Rhoptropus (Reptilia: Gekkonidae), of south-western Africa. *J. Zool.* **238**, 635–663 (1996).
22. Pianka, E. R. & Vitt, L. J. *Lizards: Windows to the Evolution of Diversity* (University of California Press, Berkeley, 2003).
23. Lamb, T. & Bauer, A. M. Footprints in the sand: Independent reduction of subdigital lamellae in the Namib–Kalahari burrowing geckos. *Proc. R. Soc. B Biol. Sci.* **273**, 855–864 (2006).
24. Gamble, T., Greenbaum, E., Jackman, T. R., Russell, A. P. & Bauer, A. M. Repeated origin and loss of adhesive toepads in geckos. *PLoS ONE* **7**, e39429 (2012).
25. Collins, C. E., Russell, A. P. & Higham, T. E. Subdigital adhesive pad morphology varies in relation to structural habitat use in the Namib Day Gecko. *Funct. Ecol.* **29**, 66–77 (2015).
26. Autumn, K. & Hansen, W. Ultrahydrophobicity indicates a non-adhesive default state in gecko setae. *J. Comp. Physiol. A* **192**, 1205 (2006).
27. Badge, I., Stark, A. Y., Paoloni, E. L., Niewiarowski, P. H. & Dhinojwala, A. The role of surface chemistry in adhesion and wetting of gecko toe pads. *Sci. Rep.* **4**, 6643 (2014).
28. Maderson, P. F. A. Keratinized epidermal derivatives as an aid to climbing in gekkonid lizards. *Nature* **203**, 780–781 (1964).
29. Ruibal, R. & Ernst, V. The structure of the digital setae of lizards. *J. Morphol.* **117**, 271–293 (1965).
30. Williams, E. E. & Peterson, J. A. Convergent and alternative designs in the digital adhesive pads of scincid lizards. *Science* **215**, 1509–1511 (1982).
31. Autumn, K. *et al.* Adhesive force of a single gecko foot-hair. *Nature* **405**, 681–685 (2000).
32. Autumn, K. & Peattie, A. M. Mechanisms of adhesion in geckos. *Integr. Comp. Biol.* **42**, 1081–1090 (2002).
33. Israelachvili, J. N. & Tabor, D. The measurement of van der Waals dispersion forces in the range 1.5 to 130 nm. *Proc. R. Soc. Lond. Math. Phys. Sci.* **331**, 19–38 (1972).
34. Niewiarowski, P. H., Lopez, S., Ge, L., Hagan, E. & Dhinojwala, A. Sticky gecko feet: The role of temperature and humidity. *PLoS ONE* **3**, e2192 (2008).
35. Hsu, P. Y. *et al.* Direct evidence of phospholipids in gecko footprints and spatula–substrate contact interface detected using surface-sensitive spectroscopy. *J. R. Soc. Interface* **9**, 657–664 (2012).
36. Jain, D., Stark, A. Y., Niewiarowski, P. H., Miyoshi, T. & Dhinojwala, A. NMR spectroscopy reveals the presence and association of lipids and keratin in adhesive gecko setae. *Sci. Rep.* **5**, 9594 (2015).
37. Alibardi, L. Immunolocalization of keratin-associated beta-proteins (beta-keratins) in the regenerating lizard epidermis indicates a new process for the differentiation of the epidermis in lepidosaurians. *J. Morphol.* **273**, 1272–1279 (2012).
38. Alibardi, L. Immunolocalization of keratin-associated beta-proteins (beta-keratins) in pad lamellae of geckos suggest that glycine–cysteine-rich proteins contribute to their flexibility and adhesiveness. *J. Exp. Zool. Part Ecol. Genet. Physiol.* **319**, 166–178 (2013).
39. Peng, Z., Yang, Y. & Chen, S. Coupled effects of the temperature and the relative humidity on gecko adhesion. *J. Phys. Appl. Phys.* **50**, 315402 (2017).
40. Huey, R. B. & Kingsolver, J. G. Evolution of thermal sensitivity of ectotherm performance. *Trends Ecol. Evol.* **4**, 131–135 (1989).
41. Huey, R. B., Niewiarowski, P. H., Kaufmann, J. & Herron, J. C. Thermal biology of nocturnal ectotherms: Is sprint performance of geckos maximal at low body temperatures?. *Physiol. Zool.* **62**, 488–504 (1989).
42. Bergmann, P. & Irschick, D. J. Effects of temperature on maximum acceleration, deceleration and power output during vertical running in geckos. *J. Exp. Biol.* **209**, 1404–1412 (2006).
43. Losos, J. B. Thermal sensitivity of sprinting and clinging performance in the tokay gecko (*Gekko gecko*). *Asiat. Herpetol. Res.* **3**, 54–59 (1990).
44. Bergmann, P. J. & Irschick, D. J. Effects of temperature on maximum clinging ability in a diurnal gecko: Evidence for a passive clinging mechanism?. *J. Exp. Zool. A Comp. Exp. Biol.* **303A**, 785–791 (2005).
45. Pesika, N. S. *et al.* Gecko adhesion pad: A smart surface?. *J. Phys. Condens. Matter* **21**, 464132 (2009).
46. Grewal, S. H., Piao, S., Cho, I.-J., Jhang, K.-Y. & Yoon, E.-S. Nanotribological and wetting performance of hierarchical patterns. *Soft Matter* **12**, 859–866 (2016).
47. Stark, A. Y., Klittich, M. R., Sitti, M., Niewiarowski, P. H. & Dhinojwala, A. The effect of temperature and humidity on adhesion of a gecko-inspired adhesive: Implications for the natural system. *Sci. Rep.* **6**, 30936 (2016).
48. Cadirov, N., Booth, J. A., Turner, K. L. & Israelachvili, J. N. Influence of humidity on grip and release adhesion mechanisms for gecko-inspired microfibrillar surfaces. *ACS Appl. Mater. Interfaces* **9**, 14497–14505 (2017).
49. Ceseracciu, L., Heredia-Guerrero, J. A., Dante, S., Athanassiou, A. & Bayer, I. S. Robust and biodegradable elastomers based on corn starch and polydimethylsiloxane (PDMS). *ACS Appl. Mater. Interfaces* **7**, 3742–3753 (2015).
50. Stark, A. Y. *et al.* Surface wettability plays a significant role in gecko adhesion underwater. *Proc. Natl. Acad. Sci. US*. https://doi.org/10.1073/pnas.1219317110 (2013).
51. Drotlef, D.-M., Dayan, C. B. & Sitti, M. Bio-inspired composite microfibers for strong and reversible adhesion on smooth surfaces. *Integr. Comp. Biol.* **59**, 227–235 (2019).
52. Tan, D. *et al.* Humidity-modulated core–shell nanopillars for enhancement of gecko-inspired adhesion. *ACS Appl. Nano Mater.* **3**, 3596–3603 (2020).
53. Geikowsky, E., Gorumlu, S. & Aksak, B. The effect of flexible joint-like elements on the adhesive performance of nature-inspired bent mushroom-like fibers. *Beilstein J. Nanotechnol.* **9**, 2893–2905 (2018).
54. Wang, Z. Slanted functional gradient micropillars for optimal bioinspired dry adhesion. *ACS Nano* **12**, 1273–1284 (2018).

55. Moser, R. *et al.* From playroom to lab: Tough stretchable electronics analyzed with a tabletop tensile tester made from toy-bricks. *Adv. Sci.* **3**, 1500396 (2016).
56. BS EN ISO 527-2 Plastics-Determination of tensile properties. *Br. Stand. BSI* (1996).
57. Kurian, A., Prasad, S. & Dhinojwala, A. Unusual surface aging of poly(dimethylsiloxane) elastomers. *Macromolecules* **43**, 2438–2443 (2010).
58. Pinheiro, J., Bates, D., Debroy, S. & Sarkar, D. *nlme: Linear and Nonlinear Mixed Effects Models*. R Core Team, R package version 3.1-137 (2018).
59. Lenth, R. *emmeans: Estimated Marginal Means, Aka Least-Squares Means*. R Core Team, R package version 1.3.4 (2019).
60. Core Team. *R: A Language and Environment for Statistical Computing* (Core Team, Vienna, 2019).

Acknowledgements
We thank Susannah Sapp, Grace Field, Catherine Implicito, Kaitlyn Naughton, Tessa Fanning, Erin Bogacki, and Ana Sofia Rive for experimental GSA sample preparation, and Ana Sofia Rive for help with live animal trials. We also thank Carla A. Narvaez for help with statistical analysis, Saranshu Singla for help with the OTS-SAM coated glass procedure, and Burak Aksak, Aaron Bauer, and Saranshu Singla for insightful discussions of this work. Finally, we thank Brad Thorstensen for the design and fabrication of the experimental apparatus. Cem Balda Dayan thanks the International Max Planck Research School for Intelligent Systems (IMPRS-IS) for his PhD fellowship. This work was funded by Villanova University and Max Planck Society.

Author contributions
C.T.M. performed all gecko and GSA adhesion experiments. C.B.D. fabricated the GSAs, and characterized the GSAs and experimental substrates. C.T.M. conducted the statistical analysis, and C.T.M, C.B.D., D.M.D., and A.Y.S. analyzed the data. C.T.M. and C.B.D. conceived and drove much of the project, however all authors helped conceive the experiments and discussed the results. A.Y.S. and M.S. supervised the research. C.T.M. drafted the manuscript, and C.B.D., D.M.D, A.Y.S., and M.S. added to and commented on the draft.

Competing interests
The authors declare no competing interests.

Additional information
Supplementary information is available for this paper at https://doi.org/10.1038/s41598-020-76484-6.

Correspondence and requests for materials should be addressed to A.Y.S.

Reprints and permissions information is available at www.nature.com/reprints.

Publisher's note Springer Nature remains neutral with regard to jurisdictional claims in published maps and institutional affiliations.

The effect of substrate wettability and modulus on gecko and gecko-inspired synthetic adhesion in variable temperature and humidity

Christopher T. Mitchell[1,†], Cem Balda Dayan[2,†], Dirk-M. Drotlef[2], Metin Sitti[2], and Alyssa Y. Stark[1,*]

[1] Department of Biology, Villanova University, 800 E. Lancaster Ave., Villanova, Pennsylvania, USA 19085

[2] Physical Intelligence Department, Max Planck Institute for Intelligent Systems, Stuttgart, Germany 70569

† Contributed equally

* Correspondence to: alyssa.stark@villanova.edu

Supplementary Material

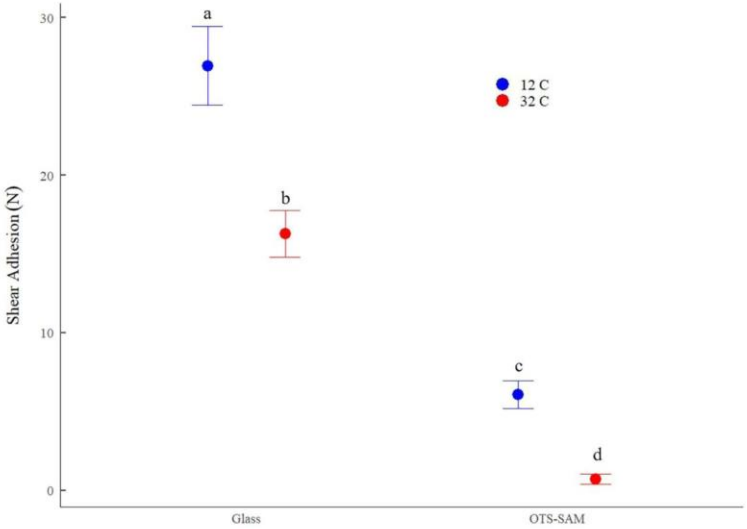

Figure S1. Shear adhesion (mean ± s.e.m.) of seven Tokay geckos (*Gekko gecko*) on hydrophilic (ca. 50° water contact angle) glass and hydrophobic (ca. 100° water contact angle) octadecyltrichlorosilane self-assembled monolayer (OTS-SAM) coated glass at two temperatures (12°C and 32°C). The means of treatment groups denoted with the same letter are not statistically different from one another according to Tukey post hoc pairwise statistical tests (see Table S1 for a detailed explanation of statistical analysis and the model output).

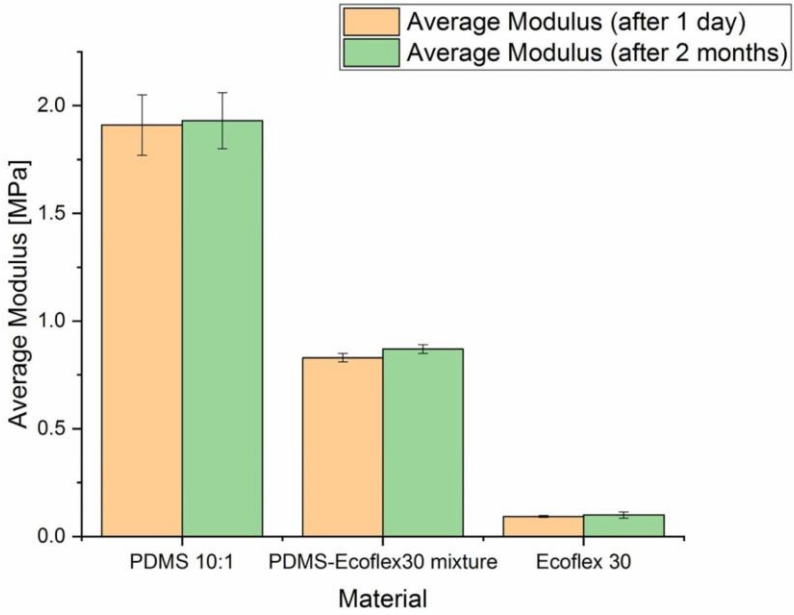

Figure S2. Aging test for modulus of PDMS 10:1, PDMS – Ecoflex 00-30 mixture (80 wt% and 20 wt%, respectively), and Ecoflex 00-30. There is no difference in Young's modulus between samples aged 1 day and 2 months post-fabrication for PDMS 10:1, PDMS 10:1 and Ecoflex 00-30 mixture, and Ecoflex 00-30.

Table S1. GLMM model output of adhesive performance (natural log transformed) of seven Tokay geckos (*Gekko gecko*) tested in variable temperature (12°C, 32°C), humidity (30, 55, 70, 80% RH), and substrate wettability (hydrophobic, hydrophilic). All single factor and interaction test statistics are included. Statistically significant differences are in bold (i.e., $p \leq 0.05$). A factor or interaction has at least one statistically significantly different mean if the corresponding p-value is $p \leq 0.05$. This criteria means that there is at least a 95% probability that the given factor or interaction contributed to differences among means within the data.

Model	Numerator degrees of freedom	Denominator degrees of freedom	F-value	p-value
Relative Humidity	**3**	**90**	**26.5410**	**<0.0001**
Temperature	**1**	**90**	**74.3186**	**<0.0001**
Substrate	**1**	**90**	**476.3889**	**<0.0001**
Relative Humidity: Temperature	**3**	**90**	**10.1904**	**<0.0001**
Relative Humidity: Substrate	**3**	**90**	**5.0961**	**0.0026**
Temperature: Substrate	**1**	**90**	**32.0404**	**<0.0001**
Relative Humidity: Temperature: Substrate	3	90	0.7167	0.5446

Table S2. GLMM model output of GSA adhesive performance (natural log transformed) tested in variable temperature (12°C, 32°C), humidity (30, 55, 70, 80% RH), substrate wettability (hydrophobic, hydrophilic), and constructed with different stalk moduli (soft, medium, stiff). All single factor and interaction test statistics are included. Statistically significant differences are in bold (i.e., $p \leq 0.05$). A factor or interaction has at least one statistically significantly different mean if the corresponding p-value is $p \leq 0.05$. This criteria means that there is at least a 95% probability that the given factor or interaction contributed to differences among means within the data.

Model	Numerator degrees of freedom	Denominator degrees of freedom	F-value	p-value
Relative Humidity	**3**	**180**	**15.032**	**<0.0001**
Temperature	**1**	**180**	**43.365**	**<0.0001**
Substrate	**1**	**180**	**23.565**	**<0.0001**
Modulus	**2**	**180**	**8.303**	**0.0054**
Relative Humidity: Temperature	**3**	**180**	**5.828**	**0.0008**
Relative Humidity: Substrate	**3**	**180**	**5.638**	**0.0010**
Temperature: Substrate	1	180	3.094	0.0803
Relative Humidity: Modulus	6	180	1.237	0.2894
Temperature: Modulus	2	180	0.006	0.9936
Substrate: Modulus	**2**	**180**	**24.610**	**<0.0001**
Relative Humidity: Temperature: Substrate	3	180	0.700	0.5532
Relative Humidity: Temperature: Modulus	6	180	0.724	0.6304
Relative Humidity: Substrate: Modulus	6	180	0.456	0.8401
Temperature: Substrate: Modulus	2	180	0.089	0.9145
Relative Humidity: Temperature: Substrate: Modulus	6	180	0.538	0.7790

Table S3. Bartlett's test for homogeneity of variance on all explanatory variables (natural log transformed) of seven Tokay geckos (*Gekko gecko*) tested in variable temperature (12°C, 32°C), humidity (30, 55, 70, 80% RH), and substrate wettability (hydrophobic, hydrophilic). Statistically significant tests are in bold (i.e., $p \leq 0.05$). Significant tests indicate that the levels within the significant factor (i.e., substrate) have different variances, and therefore require additional consideration in a statistical model (i.e., a GLMM with *varIndent* function must be used).

Explanatory variable	Bartlett's K^2	Degrees of freedom	p-value
Relative Humidity	2.0078	3	0.5708
Temperature	3.0884	1	0.07885
Substrate	**7.3509**	**1**	**0.006703**

Table S4. Bartlett's test for homogeneity of variance on all explanatory variables (natural log transformed) of GSA adhesive performance tested in variable temperature (12°C, 32°C), humidity (30, 55, 70, 80% RH), substrate wettability (hydrophobic, hydrophilic), and constructed with different stalk moduli (soft, medium, stiff). Statistically significant tests are in bold (i.e., $p \leq 0.05$). Significant tests indicate that the levels within the significant factor (i.e. modulus) have different variances, and therefore require additional consideration in a statistical model (i.e., a GLMM with *varIndent* function must be used).

Explanatory variable	Bartlett's K^2	Degrees of freedom	p-value
Relative Humidity	1.5078	3	0.6805
Temperature	0.55574	1	0.456
Substrate	1.5664	1	0.2107
Modulus	**28.936**	**2**	**<0.0001**

Appendix C. 3D Printing of Elastomeric Bioinspired Complex Adhesive Microstructures

This appendix includes the following publication:

1. **Cem Balda Dayan**[*], Sungwoo Chun[*], Nagaraj Krishna-Subbaiah, Dirk-Michael Drotlef, Mukrime Birgul Akolpoglu, and Metin Sitti, 3D printing of elastomeric bioinspired complex adhesive microstructures. *Advanced Materials*, 2021,
   doi: 10.1002/adma.202103826.

[*] Equally contributing co-first authors

ADVANCED MATERIALS
www.advmat.de

3D Printing of Elastomeric Bioinspired Complex Adhesive Microstructures

*Cem Balda Dayan, Sungwoo Chun, Nagaraj Krishna-Subbaiah, Dirk-Michael Drotlef, Mukrime Birgul Akolpoglu, and Metin Sitti**

Bioinspired elastomeric structural adhesives can provide reversible and controllable adhesion on dry/wet and synthetic/biological surfaces for a broad range of commercial applications. Shape complexity and performance of the existing structural adhesives are limited by the used specific fabrication technique, such as molding. To overcome these limitations by proposing complex 3D microstructured adhesive designs, a 3D elastomeric microstructure fabrication approach is implemented using two-photon-polymerization-based 3D printing. A custom aliphatic urethane-acrylate-based elastomer is used as the 3D printing material. Two designs are demonstrated with two combined biological inspirations to show the advanced capabilities enabled by the proposed fabrication approach and custom elastomer. The first design focuses on springtail- and gecko-inspired hybrid microfiber adhesive, which has the multifunctionalities of side-surface liquid super-repellency, top-surface liquid super-repellency, and strong reversible adhesion features in a single fiber array. The second design primarily centers on octopus- and gecko-inspired hybrid adhesive, which exhibits the benefits of both octopus- and gecko-inspired microstructured adhesives for strong reversible adhesion on both wet and dry surfaces, such as skin. This fabrication approach could be used to produce many other 3D complex elastomeric structural adhesives for future real-world applications.

C. B. Dayan, Prof. S. Chun, N. Krishna-Subbaiah, Dr. D.-M. Drotlef, M. B. Akolpoglu, Prof. M. Sitti
Physical Intelligence Department
Max Planck Institute for Intelligent Systems
70569 Stuttgart, Germany
E-mail: sitti@is.mpg.de
Prof. S. Chun
Department of Electronics and Information Engineering
Korea University
Sejong 30019, Republic of Korea
Prof. M. Sitti
Institute for Biomedical Engineering
ETH Zürich
Zürich 8092, Switzerland
Prof. M. Sitti
School of Medicine and College of Engineering
Koç University
Istanbul 34450, Turkey
The ORCID identification number(s) for the author(s) of this article can be found under https://doi.org/10.1002/adma.202103826.

DOI: 10.1002/adma.202103826

1. Introduction

Many synthetic advanced functional micro/nanomaterials are inspired by micro/nanostructured biological materials in nature as one of the promising approaches.[1–3] These bioinspired functional micro/nanostructures have many different uses, such as dry adhesion,[4] wet adhesion,[5] liquid repellency,[6–9] and heat transfer.[10] One of the widely studied bioinspired synthetic structures has been gecko-foot-hairs-inspired dry fibrillar adhesives using majorly van der Waals forces to stick almost any smooth surface material.[11–18] These fibrillar repeatable and controllable adhesives have been well investigated in respect of contact mechanics,[19,20] adhesion and friction control,[16,21,22] and wet and dry self-cleaning.[23–26] Performance of these synthetic adhesives is even better than their biological counterparts source in some specific cases.[27,28] On the other hand, springtail-inspired microstructures have been investigated for their liquid repellency.[6] Springtail's skin can repel down to ≈25 mN m^{-1} surface tension liquids.[29] Inspired by these microstructures on the springtail skin, some synthetic double re-entrant microfibers were proposed to repel even fully wetting fluorinated liquids.[6] Morphology of the gecko-inspired T-shaped fiber adhesives and springtail-inspired double re-entrant microfibers is similar with a flat fiber tip surface. However, springtail-inspired structures have overhangs under their flat tip surfaces as different from the T-shaped adhesives. Current double re-entrant structures have been mostly made of rigid materials.[6–9] However, T-shaped fibers are made of soft elastomers to attain conformal contact for high adhesion. A recent study merged these two concepts and showed both dry adhesion and super liquid repellency on the fiber top surface using elastomeric double re-entrant microfibers with flat tips.[30] Nevertheless, these fibers are sensitive to side wetting due to lack of their side-surface liquid repellency.

Side-surface liquid repellency can be possible by various methods. First, continuous sidewalls can be used,[8,31–33] which have the fundamental drawback of having their receding contact angle converge to zero degree at the walls during aspiration (dewetting).[32–34] Here, the walls cannot repel the liquid after a

certain point, because of high pinning forces due to a large contact area.[8,31–34] Second, to overcome this problem, horizontal side double re-entrant microfibers on the side surfaces can be used.[7] As the main advantage of this method, the receding contact angle will be the same as the middle top-surface part of the fiber array, thanks to the individual fiber placement on the boundary of the array, which decreases the contact area between the liquid and fibers dramatically. Such complex 3D structures cannot be fabricated by the typically used molding techniques;[30] two-photon polymerization type of 3D microprinting methods are required instead.[7] Such horizontal side double re-entrant microfibers were already 3D-printed by rigid polymers so far for liquid repellency purposes only.[7] Such rigid microstructures[7,8,31] cannot be used as side liquid-repellent dry fibrillar adhesives, which require soft elastomeric structures.[35]

On the other hand, several studies have developed elastomeric microstructured patches for attaching to skin or other tissues for medical and wearable device applications recently.[36–39] Achieving a conformal contact between the adhesive patch and biological surfaces is critical for high adhesion performance for tissue adhesives.[40,41] Gecko-inspired fibrillar dry adhesives are one of the candidates for skin adhesion.[41,42] However, in wet, liquid-immersed conditions, their adhesion is reduced notably because of significantly reduced van der Waals forces.[43] On the other hand, octopus-suction-cup-inspired microscale dome-like protuberances adhere strongly in wet conditions on smooth surfaces.[5,44] But, they are not that effective in adhering to dry surfaces with compared to the gecko-inspired adhesives. Therefore, combining gecko- and octopus-inspired microstructured adhesives in the same elastomeric structures could be the most effective way to adhere strongly to wet and dry surfaces.

In this study, we used direct 3D printing of elastomeric microstructures using the two-photon lithography technique (**Figure 1**a) to enable two complex, 3D, and novel adhesive microstructure designs, which address the two open issues on side-surface (in addition to top-surface) liquid repellency (Figure 1b) and underwater adhesion of gecko-inspired elastomeric microfiber adhesives (Figure 1c). First, combining both springtail- and gecko-inspired microstructures into a hybrid structure (see Figure 1b,d,f) enabled side-surface liquid-repellent dry fibrillar adhesives. This microstructure design has three functionalities simultaneously: top-surface liquid super-repellency, side-surface liquid-repellency, and strong dry adhesion. Next, combining both octopus- and gecko-inspired microstructures into a hybrid structure, as illustrated in Figure 1c,e, enabled high adhesion on both underwater and dry conditions on synthetic skin replicas toward future medical applications, merging the strength of each bioinspired structure design.

2. Results

Top- and side-surface liquid repellency of the springtail- and gecko-inspired hybrid structure array was characterized using contact angle measurements. Diverse range of surface tension liquids was tested for advancing and receding contact angles. Surface tension of the liquids ranged between ≈14 and ≈72.80 mN m^{-1}. One of the highly wetting liquids (perfluorooctane) could be repelled and remained in the Cassie state on the structures (**Figure 2**a,b). Side-surface liquid repellency of the array was also tested. For only side-surface liquid repellency characterization, the top surface of the double-reentrant fibers was covered by a glass slide. The liquid was applied into the pool with the constant rate of 1 mL min^{-1}. As shown in Figure 2c, the fiber array repelled the deionized (DI) water from its side. In addition, top- and side-surface liquid repellency of the array was tested under full liquid immersion (Figure 2d,e). For this experiment, we used a confocal microscope (Leica SP8, Wetzlar, Germany) to prove and visualize the liquid repellency in full-immersion conditions. As shown in the confocal microscopy images in Figure 2f–h, the springtail- and gecko-inspired patch was able to repel liquid from its top surface and all side surfaces when it was fully immersed with DI water. During full immersion experiments, the rate of the applied liquid was 1 mL min^{-1}.

The hybrid structure array's adhesion performance was characterized with a uniaxial adhesion setup (**Figure 3**a). During these measurements, a smooth hemispherical glass (diameter 10 mm) was used to contact with the structure top surfaces. Approaching and retracting speeds were 25 μm s^{-1} during these tests. Initially, the saturation value of the preload was found for these structures (Figure S4, Supporting Information). The rest of the adhesion experiments were performed using the same saturation preload value (6 mN). For adhesion tests, hydrophobic and hydrophilic glass probes were used to investigate the effect of contact surface's wettability on adhesion in both dry and wet conditions. Initially, dry adhesion tests were performed for hydrophilic and hydrophobic probes. Both different wettability behavior probes resulted in almost the same adhesion performances in dry conditions (Figure 3b,c). For wet adhesion characterization (Figure 3d,e), we applied a 5 μL DI-water droplet on the top surface of the patch. Additionally, during hydrophobic and hydrophilic probe adhesion tests, droplet always stayed in the Cassie regime on the patch. The results showed that the hydrophobic probe was able to push the liquid to the side, before contacting the fiber tip surfaces (Figure 3f). Thus, a dry contact was possible with the double re-entrant fiber tips after pushing droplet out of the patch. As a result, in wet conditions, the hydrophobic probe performed the similar adhesion performance with dry conditions (Figure 3b,d).[30] The side liquid-repellent structures pushed away from the droplets and the liquid could not penetrate inside of the patch when they passed out of the patch area (Figure 3f).[7]

For wet adhesion experiments with the hydrophilic glass probe, while the probe was approaching the fibers, the complete droplet moved to the glass probe just after initial contact. Afterward, no liquid remained on the patch top surface (Figure 3e,g) due to the high wettability behavior of the hydrophilic probe and liquid super-repellency of the patch. The initial contact between the fiber tips and the probe occurred while the hydrophilic probe was carrying the droplet. At the end of the approaching state, the droplets got wider between the probe and fibers. During preloading, the droplets could not be pushed away completely due to high wettability of the hydrophilic probe. The droplets remained between the fibers and hydrophilic probe. Consequently, the hydrophilic probe resulted in relatively lower adhesion values compared to the dry case, due to the liquid layer between the two interfaces (Figure 3b,e,g). During

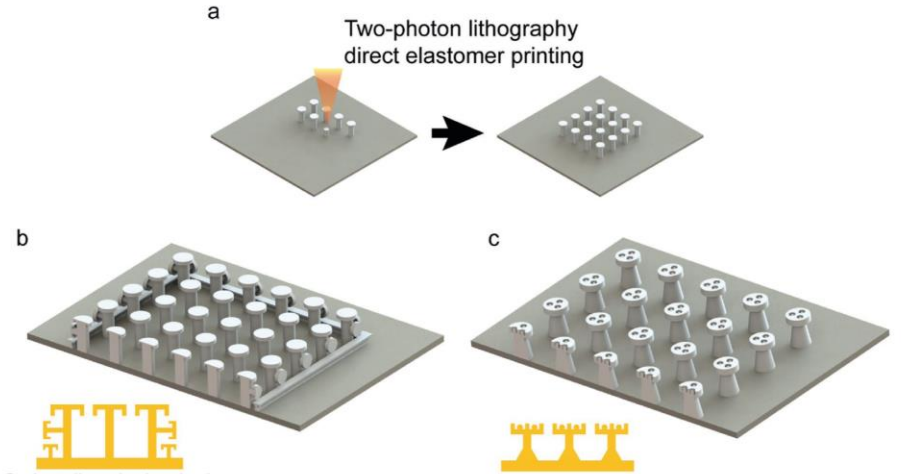

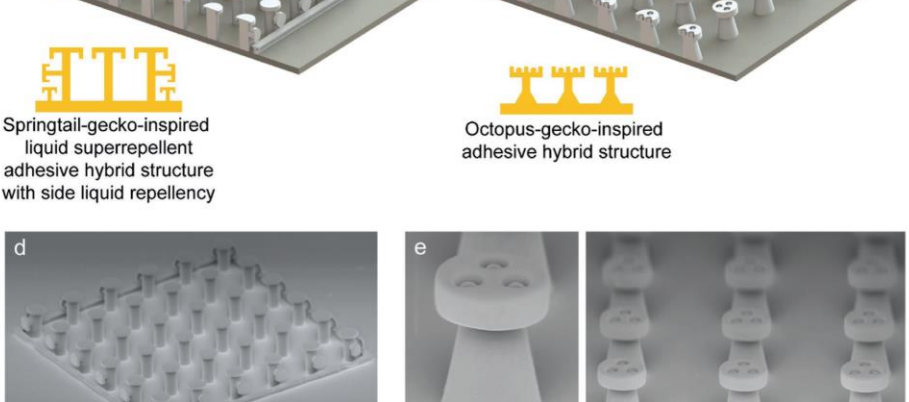

Figure 1. Direct-3D-printing-based approach for fabricating elastomeric complex 3D bioinspired adhesives. a) Schematics of the fabrication process. Two-photon-polymerization-based direct 3D printing of the structures using a custom elastomer resin. b,c) Inspiration sources and designs of two hybrid bioinspired adhesives. b) Springtail- and gecko-inspired adhesive hybrid structures with side-surface liquid repellency. c) Octopus- and gecko-inspired adhesive hybrid structures with strong wet and dry adhesion. d–f) Scanning electron microscopy (SEM) images of the fabricated bioinspired adhesives. d) A full array of double re-entrant structures with side-surface liquid repellency. e) A single and an array of octopus–gecko-inspired adhesive structures. f) Zoomed SEM images of the side and vertex structures of the springtail–gecko-inspired adhesive structure array.

these experiments, similar to the hydrophobic probe adhesion tests, pushed-out liquid droplets did not penetrate into the patch because of the side liquid-repellent structures (Figure 3g). In these tests, we observed the advantage of having all three features (top-surface liquid repellency, side-surface liquid repellency, and strong adhesion) at the same time.

To compare these adhesion performance results with the literature, the researchers reported that biological gecko foot hairs have around 10 kPa normal and 100 kPa shear adhesive strength on smooth glass surfaces.[4,45] As single-material-based synthetic high-performance gecko-inspired adhesives, different groups[13,14] reported elastomeric gecko-inspired mushroom

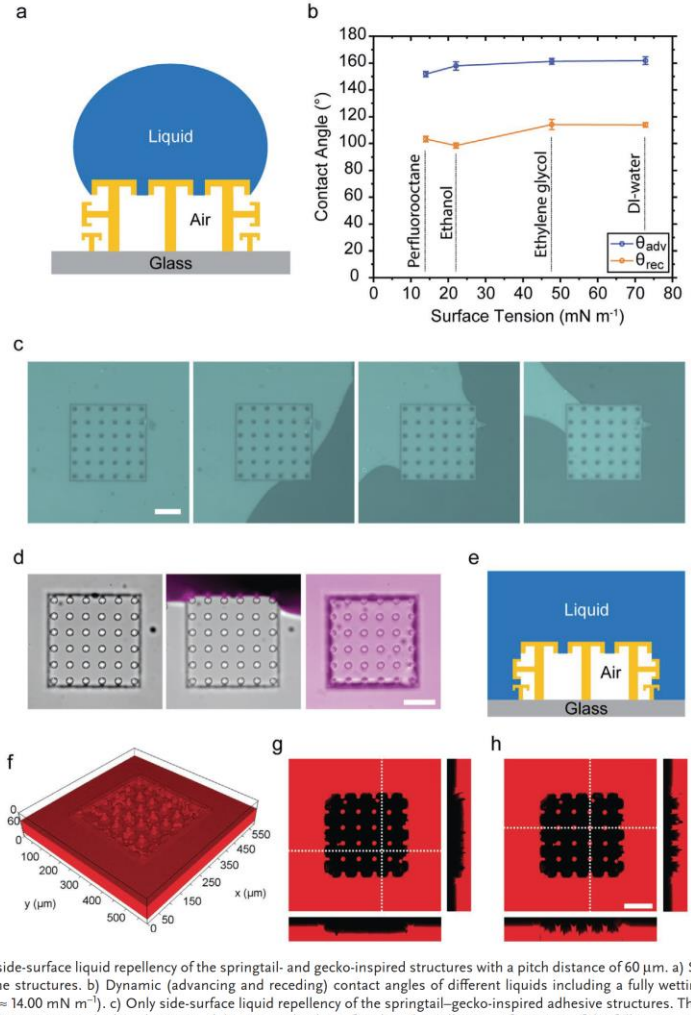

Figure 2. Top- and side-surface liquid repellency of the springtail- and gecko-inspired structures with a pitch distance of 60 μm. a) Schematic of a liquid droplet on top of the structures. b) Dynamic (advancing and receding) contact angles of different liquids including a fully wetting fluorinated liquid (perfluorooctane, $\gamma \approx 14.00$ mN m^{-1}). c) Only side-surface liquid repellency of the springtail–gecko-inspired adhesive structures. The green sections are the air and the black sections are the liquid regions. d–h) Top- and side-surface liquid repellency performance of the full structure array in full immersion. d) The video snapshots while liquid approaches and covers all sides of the patch. e) Side-view schematic of the patch in the full liquid immersion condition. f) 3D confocal optical microscopy image of these structures (upside-down image to show the air cavity: the red section is the liquid part and the empty section is the air gap part) and g,h) 2D confocal microscopy cross-section images of the array in full immersion. In confocal images, the red sections are the liquid and the black sections are the air parts. The repellent pillars are in contact with the red dye mixed inside the liquid. They reflect dye color; therefore, their stamp color is also red. Scale bars: 100 μm.

structures, which had 100–180 kPa adhesion strength on a dry smooth glass substrate. Recently, another study showed that liquid-repellent adhesive structures had ≈100 kPa adhesive strength.[30] In this study, we showed that our springtail- and gecko-inspired adhesive structures had contact area with ≈200 μm contact radius after contacting to a smooth glass hemisphere. The full contact area was 0.124 (± 0.015) mm^2. The average dry adhesion force was measured as 14.3 (± 0.5) mN.

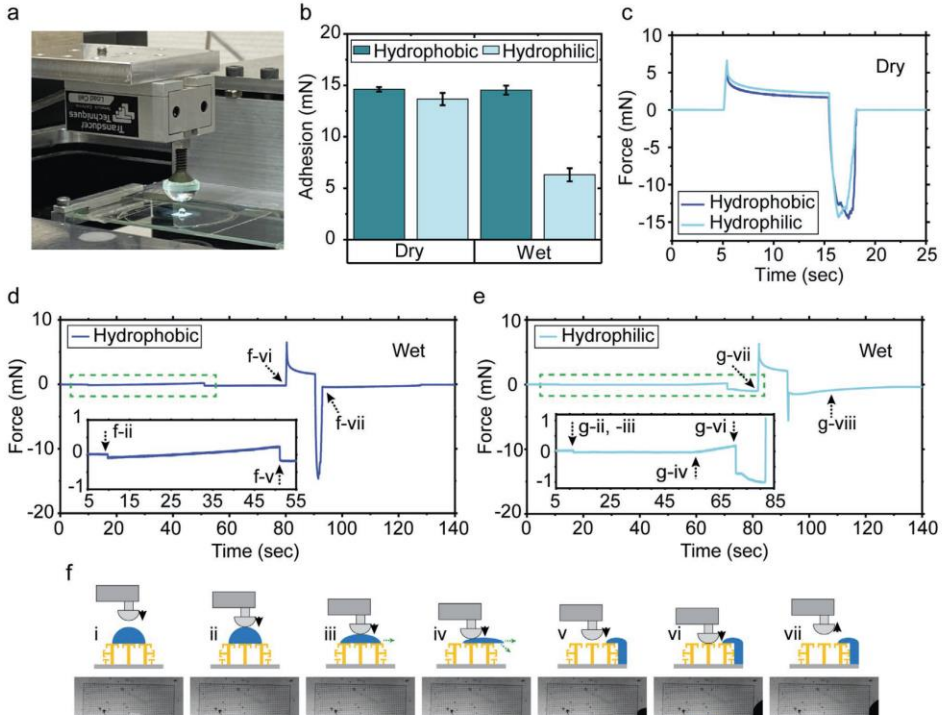

Figure 3. Adhesion characterization results of the springtail–gecko-inspired structures with side-surface liquid repellency and pitch distance of 60 µm. a) A picture of the custom adhesion set-up with a droplet on top of the sample. b) Dry and wet adhesion results using both hydrophobic and hydrophilic hemisphere glass probes. c) Representative dry adhesion force graphs with respect to time for the hydrophobic and hydrophilic probes. d,e) Representative wet adhesion force graphs with respect to time for the hydrophobic probe (d) and the hydrophilic probe (e). f,g) Schematic and experimental video snapshots during wet adhesion testing, where the side liquid repellency is observed when using the hydrophobic probe (f) and the hydrophilic probe (g). All the error bars in graphs represent standard deviations for samples ($N = 5$). Scale bars: 1 mm.

Thus, we achieved the dry adhesive strength of 115 kPa, similar to high-performance gecko-inspired microfiber adhesives in the literature.

Next, wet and dry adhesion performance of the octopus- and gecko-inspired hybrid microstructures was characterized (**Figure 4**). It is well known that the octopus patterns are

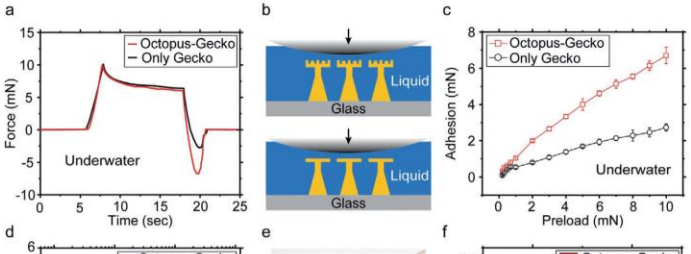

Figure 4. Adhesion characterization results of the hybrid octopus–gecko-inspired structure patch with pitch distance of 80 μm. a) Representative adhesion-force–time graphs for only-gecko-inspired and hybrid octopus–gecko-inspired structures in immersed conditions with DI-water. The applied preload was 10 mN in ambient conditions and the approaching and retraction speeds were 5 μm s^{-1} and the relaxation time was set to 10 s. b) Schematic illustrations of the only-gecko-inspired structure (bottom) and the hybrid octopus–gecko-inspired structure (top) for adhesion under water. c) Adhesion values for different preloads (0.2–10 mN) in underwater condition. d) Repeatability adhesion tests of the hybrid octopus–gecko-inspired structure more than 1000 cycles. The applied preload was 5 mN and the time interval between measurements was 5 s. e) Schematic of the hybrid structure patch adhering to the wet and rough biological skin. f) Adhesion results for only-gecko-inspired patch and hybrid structured patch in dry and underwater conditions on a synthetic skin replica with the preload of 5 mN. For measurements, the skin replica was placed into a container without or with DI- water on the stage, and then the flat end screw attached with the hybrid-structured patch was moved to contact with the skin replica. All the error bars in the graphs represent standard deviations for the samples ($N = 5$).

effective to achieve strong wet adhesion.[5,44,46,47] Specifically, the dome-like protuberance structure of the octopus suckers enhance wet adhesion due to their structural property.[5,44,48] As shown in Figure 4a, gecko-inspired microfiber adhesives showed low underwater adhesion performance due to the significant reduction of the van der Waals forces in immersed conditions.[39] This is the result of the interfacial liquid layer between the glass probe and the microfiber tip surfaces. On the other hand, inserting the octopus patterns on the microfiber tip surfaces increased the wet adhesion with an applied preload by generating a cohesive force among the liquid molecules without an insignificant energy consumption owing to the internal dome-like protuberance structure that makes the residual liquid in the chamber to pull up to both sides due to capillary force induced by deformation with vertical preload (Figure 4a,b).[5] Thus, these hybrid structures exhibited higher underwater adhesion than the gecko-inspired adhesives (Figure 4c). By increasing the preload from 0.2 to 10 mN, the adhesion performance increased around three times under water. Thus, the hybrid design improved the underwater adhesion while maintaining the dry adhesion performance of the gecko-inspired microfibers. In dry conditions, the gecko-inspired structure had stronger adhesive force than the octopus- and gecko-inspired hybrid structure because of larger contact area (Figure S6, Supporting Information). In addition, the operational reliability of adhesion performance in underwater condition was confirmed in Figure 4d. The measurements were conducted by repeatedly applying the vertical preload (5 mN) on the hybrid structures with over 1000 attachment-detachment cycles, where the approaching and retraction speeds were 5 μm s^{-1} and the relaxation time was 10 s, and the time interval between measurements was 5 s. The results show that the adhesion performance was highly robust for octopus- and gecko-inspired hybrid structures in underwater conditions. Likewise, in dry environments with the same measurement conditions (preload of 5 mN), the hybrid structure also showed a reproducible adhesion performance under 1000 loading-to-unloading cycles (Figure S7, Supporting Information) because the printed elastomer material is highly robust to preload owing to its mechanical flexibility.

Adhesion performance of the octopus–gecko-inspired patch on a synthetic soft skin replica (with a similar mechanical and structural property of a biological skin) was characterized in both dry and underwater conditions (Figure 4e,f). In the dry condition, the octopus–gecko-inspired patch presented higher adhesion than the gecko-inspired patch on the synthetic soft skin. This means that the adhesion improved due to the suction effect. Octopus patterns had a high suction force on the rough skin surface. On the other hand, gecko-inspired patches were supposed to have lower fiber tip-surface contact area on rough surfaces. This leads to lower adhesion compared to the octopus–gecko-inspired hybrid adhesives in both dry and wet conditions on the skin replica. More importantly, the gecko-inspired patch almost lost its adhesion underwater. In comparison, the octopus–gecko-inspired hybrid structure showed around three times higher adhesion and high repeatability under water. Therefore, the octopus–gecko-inspired structures

overcame the shortcomings and showed high adhesion on both wet and dry skin replica.

3. Conclusion

Our approach of the direct 3D printing of the elastomeric 3D microstructures allowed us to fabricate hybrid, bioinspired, multifunctional, and complex adhesive structures. The demonstrated two-hybrid adhesive designs improved the performance of the current structural adhesives in different real-world conditions. This approach enables to integrate many other different bioinspired or human-made, 3D and complex structural adhesives almost without considering any fabrication constraint. The first demonstrated array design showed top-surface liquid super-repellency, side-surface liquid repellency, and strong adhesion on the same patch for the first time. The second design enabled strong adhesion in both underwater and dry conditions. Low Young's modulus, high elongation, and high surface energy of the custom aliphatic urethane-acrylate-based elastomer were essential for these complex structural adhesives to have high performance. In terms of the fabrication speed and throughput, this approach may not be comparable with the molding techniques. However, the proposed approach is needed to fabricate complex 3D elastomeric structural adhesives, which cannot be molded reliably. The speed and throughput of the fabrication process will be enhanced proportionally by the advancements in the commercial two-photon lithography systems. Already, there are some two-photon-lithography systems in the market for high-throughput production for industrial use. Furthermore, there are many investigations to increase the throughput and speed of two-photon lithography in industry. The proposed approach can be also used in developing other future complex structural elastomer adhesives and other microstructured 3D materials. These complex adhesive structures can be used in robotics, biomedical device, part and tissue handling, fastener, and pick-and-place applications in dry and wet conditions. For these potential applications, the required patch areas can vary from hundreds of micrometers to several centimeters square, where large-area samples would take more fabrication time up to a day. Therefore, tissue handling, electronic device component handling, biomedical device, and robotic applications requiring only small-area adhesive patches would be a better fit for shorter fabrication times of several hours.

Table 1. The custom aliphatic urethane-acrylate-based elastomer resin material composition that was used for two-photon-polymerization-based elastomeric microstructure 3D printing.

Materials	Chemistry	Trade name	Concentration [wt%]
Oligomer	Aliphatic urethane acrylate	BASF Laromer UA 9072	92
Monomer	Bisphenol-A-ethoxylate15-dimethacrylate	–	5
Photoinitiator	Diphenyl-(2,4,6-trimethylbenzoyl)-phosphine oxide	TPO	3

4. Experimental Section

Custom-made Elastomeric Resin Material: A custom-made photocurable resin was used as an elastomeric material to be used in two-photon-lithography-based 3D printing of the hybrid structure designs. The material is made of an oligomer, a monomer, and a photoinitiator. BASF Laromer UA 9072, which is a urethane-modified acrylic resin, was used as the oligomer with 92 wt%. As the monomer, bisphenol A ethoxylate dimethacrylate 15 (BPA(EO)15DMA) was included with 5 wt%. Diphenyl (2,4,6-trimethylbenzoyl) phosphine oxide (TPO) with 3 wt% was added as the photoinitiator (**Table 1**). All these ingredients were mixed for ≈16 h with 50 rpm using magnetic stirrer (RCT basic, IKA, Germany) until the resin was homogenous.

The Young's modulus and elongation at break of the cured custom resin material were measured as 17.1 ± 2.2 MPa and 126.3 ± 19.4%, respectively using a universal tensile testing machine (model: 5942, INSTRON, Norwood, MA, USA) according to the ISO-527-2-type-5b standard.[49] The surface energy of the cured resin was calculated as 40.4 mN m^{-1}, according to the Fowkes model.

Fabrication Process of the Microstructures: For fabricating the elastomeric bioinspired hybrid adhesive microstructures, direct elastomer 3D printing using the two-photon-polymerization technique was implemented. After the printing of the desired structures using the custom-made resin, they were subjected to post-processing. The samples were immersed in a beaker containing propylene glycol methyl ether acetate (PGMEA) for 2 h to dissolve the uncured parts of the resin. Next, the samples were placed for 5 min in another beaker containing fresh PGMEA to ensure the uncured parts of the resin was dissolved completely. Then, the samples were placed in a beaker containing isopropanol alcohol (IPA) for 3 min to terminate the dissolving process. As the next step, the samples were transferred into fresh IPA and post-UV curing was done for 3 min with an external UV-curing system (Omnicure Series 2000, Excelitas Tech. Corp.). Finally, the samples were dried using a critical point dryer (Leica EM CPD300, Wetzlar, Germany).

Springtail- and Gecko-Inspired Hybrid Microstructure Geometries: The tip diameter of the double re-entrant structure's top part was 30 µm, the stamp diameter was set to 18 µm, the tip thickness was set to 3 µm, the overhang thickness was 2 µm, and the overhang height was 3 µm. For outer boundary structures of the array (double re-entrant structures with side double re-entrant branches), the top part was identical with the tip of the middle structure (there is no side branched double re-entrant structures for the middle fibers). Additionally, the patch array had outer boundary double re-entrant fibers with side double re-entrant branches to repel liquids from side. For side double re-entrant branches, the tip diameter was set to 22 µm, the stamp diameter was 10 µm, the tip thickness was 3 µm, the overhang thickness was 2 µm, and the overhang height was 3 µm. For all fibers, the structure height was 50 µm (Figure S3, Supporting Information). The pitch distance was 60 µm among fibers. Furthermore, boundary structures also had a continuous wall below their side double reentrant branches. These small continuous walls were necessary to keep liquids outside of the patch. The absence of small continuous walls below side double-reentrant branches cause liquid to proceed on the glass and penetrate inside of the patch area.[7]

Octopus- and Gecko-Inspired Hybrid Microstructure Geometries: Tip diameter of these fibrillar structures was 36 µm, the tip thickness was 10 µm, the stamp neck diameter was 20 µm, the base diameter was 30 µm, and the height of the structure was 47 µm for octopus- and gecko-inspired fiber structures and T-shape fibrils. The pitch distance among fibers was 80 µm for both structure geometries. The protuberance diameter of octopus- and gecko-inspired fiber structure geometry was 7 µm and it was shifted 1 µm downward for attaching protuberance inside of the suction cup. The suction cup diameter was 10 µm with 7 µm height. For each octopus- and gecko- inspired fiber structures, three octopus inspired suction cups were placed on top of the tip with 8 µm spacing in each (Figure S3, Supporting Information).

Direct 3D Printing of the Elastomeric Hybrid Fibrillar Microstructures: For each individual structure, computer-aided design was realized by Solidworks. Then the stereolithography file (.stl) was generated. The

generated file (.stl) was loaded into the Nanoscribe software (Photonic Professional GT2, Nanoscribe GmbH, Germany). Here, the two-photon lithography system was used in oil mode. In this mode, the resin material was placed on top of the glass and the oil was placed between the glass and the objective. As the objective lens, 63x, 1.4 NA objective was used for achieving high resolution. Galvo scan mode was preferred to print the structures layer by layer. For the resin, the ideal process parameters were found by optimizing the process parameters, especially the scan speed and laser power. The optimum parameters were 75% for the laser power and 6 mm s^{-1} for the scan speed. The fabrication duration of a single structure is between 30 s and 1 min depending on the complexity of the 3D fibril shape.

Wettability Characterization of the Springtail–Gecko-Inspired Structures: To determine the surface wettability of the springtail–gecko-inspired structures, a commercial contact angle measurement device (Drop Shape Analyzer DSA100, Krüss GmbH, Hamburg, Germany) was used. As the characterization method, the sessile drop was chosen. For each liquid, advancing and receding contact angles were measured at least 10 times. For each characterization, applied droplet volume varied between ≈2 and ≈5 µL. As the liquid dosing and aspiration speed, ≈0.2 µL s^{-1} was used. All these measurements were performed in room conditions with 23 °C temperature and 30% humidity.

Full Immersion and Only Side-Surface Liquid Repellency Characterization of the Springtail–Gecko-Inspired Structures: For full immersion and only side liquid repellency characterizations of springtail–gecko-inspired structures, the sample was placed on a glass microscope slide. The microscope slide boundary was covered by a poly(methyl methacrylate) (PMMA) wall. One side of the polymer tube was attached inside of the pool and the other end was attached to a 20 mL plastic syringe. A plastic syringe was placed on a programmable syringe pump (Legato 210p, KD Scientific, USA) to apply the liquid in a controlled and robust rate. For full immersion characterizations, the liquid was applied with a constant rate of 1 mL min^{-1} until to reach 5 mm height of liquid inside the pool. For only side-surface wetting characterizations, a flat untreated glass was placed on the patch before applying the liquid. Then, the liquid was applied with the rate of 1 mL min^{-1} until all side of the patch was covered by the liquid. The applied liquid height did not pass top part of the glass during these experiments. All these measurements were carried out in room conditions with 23°C temperature and 30% humidity.

Confocal Optical Microscopy Imaging: For the visualization of immersion, the samples were placed inside a PMMA wall and filled with water using a syringe pump (Legato 210p, KD Scientific, USA) at a rate of 1 mL min^{-1}. For fluorescence imaging, Rhodamine B fluorescent dye (0.001 mg mL^{-1} in dH_2O) was used. Samples were imaged and recorded during the immersion experiment to show liquid-structure interactions with a Leica DMi8 fluorescence inverted microscope (Wetzlar, Germany). Images, where liquid-structure interactions take place, were pseudo-colored using Adobe Photoshop software. A Leica SP8 single-point scanning confocal microscope (Wetzlar, Germany) equipped with a 20×/0.4 objective was used to obtain confocal images of structures and liquid–vapor interfaces immediately after immersion. A 3D reconstruction of the *z*-stack planes was made using LAS X software. All these measurements were carried out in room conditions with 23 °C temperature and 30% humidity.

Adhesion Characterization Setup: A custom-made adhesion characterization setup was used for the dry and wet adhesion measurements. To visualize and record the contact, the video camera (Grasshopper3, Point Grey Research Inc.) was connected to an inverted optical microscope (Axio Observer A1, Zeiss). A computer-controlled high precision piezo stage (LPS-65 2", Physik Instrumente GmbH & Co. KG) was mounted on the microscope for *z*-direction. The resolution of the motion stage was 5 nm. For alignment in the x and y directions, the manual stage (NFP-2462CC, Positionierungstechnik Dr Meierling) was used. To find adjustments for tilting was done by two goniometers (M-GON65-U, Newport, Irvine, CA, USA). A sensitive load cell (GSO-25, Transducer Techniques, Temecula, CA, USA) was mounted on the piezo motion *z*-stage to obtain force data. A signal conditioner (TMO-2, Transducer Techniques, Temecula, CA, USA) and data acquisition board (USB-6001, National Instruments, Austin, TX, USA) were connected to the load cell for computer connection. The data acquisition and motion control of the piezo stage were managed by a custom-made LabVIEW (National Instruments, Austin, TX, USA) program. Preloads, velocities, contact times, and the displacements in the z direction were controlled using the program.

Adhesion Testing: The load cell of the adhesion setup was connected to a flat end screw. A flat end screw glued on the flat side of the glass hemisphere probe (10 mm diameter, ACL108U, Thorlabs). The glass hemisphere probe was used as a contact surface during the measurements. The microfiber adhesive patches were placed on a microscope slide.

For the springtail–gecko-inspired adhesives, the approaching speed was 25 µm s^{-1}. After reaching the desired preload, the relaxation time was 10 s during all measurements. Then, until the glass probe fully detached, the probe was retracted at 25 µm s^{-1}. For wet adhesion characterizations, the amount of the DI-water droplet was 5 µL. The lower amount of the liquid was not possible to apply due to the super-liquid-repellent property of these structures.

For all octopus–gecko-inspired and gecko-inspired structure adhesion experiments, the approaching and retraction speeds were 5 µm s^{-1} and the relaxation time was set to 10 s. A representative force–time measurement (Figure 4a), dry and underwater adhesion with different preloads measurements (Figure 4c and Figure S6, Supporting Information), adhesion repeatability characterizations (Figure 4d) were conducted by using the glass hemisphere probe for different preload adhesion measurements. For the hemisphere glass probe adhesions, the glass probe approached to and retracted from the patch sample while force values were measured from the load cell. For all skin replica experiments, the hybrid or gecko-inspired adhesive patch was glued to the load cell with a tungsten connector. For dry skin adhesion measurements, the skin replica was placed on the stage without any liquid in the environment. For underwater skin adhesion measurements, the skin replica was placed on the stage into a DI-water filled container. In all skin adhesion measurements, while the force values were measuring from the load cell, the hybrid or gecko-inspired adhesive patch approached to and retracted from the skin replica.

To minimize the viscoelastic effects, approach and retraction velocities were set to low values for all adhesion experiments. After each set of measurements, the probe was cleaned with particle-free tissue and isopropyl alcohol. For each data point, experiments were repeated at least five times. All these measurements were carried out in room conditions with 23 °C temperature and 30% humidity.

Supporting Information

Supporting Information is available from the Wiley Online Library or from the author.

Acknowledgements

C.B.D. and S.C. contributed equally to this work. The authors thank Filip Podjaski for absorbance-wavelength and transmittance-wavelength measurements and Ville Liimatainen for helpful discussions. This work was funded by the Max Planck Society. The authors thank the International Max Planck Research School for Intelligent Systems (IMPRS-IS) for supporting C.B.D. and S.C. thanks the Alexander von Humboldt Foundation for the fellowship support.

Open Access funding enabled and organized by Projekt DEAL.

Conflict of Interest

The authors declare no conflict of interest.

Data Availability Statement

The data that support the findings of this study are available from the corresponding author upon reasonable request.

Keywords

bioinspired microstructures, gecko-inspired adhesives, liquid superrepellency, reversible adhesion, two-photon polymerization

Received: May 20, 2021
Revised: June 16, 2021
Published online: August 15, 2021

[1] C. Zhang, D. A. McAdams, J. C. Grunlan, *Adv. Mater.* **2016**, *28*, 6292.
[2] T. Kong, G. Luo, Y. Zhao, Z. Liu, *Adv. Funct. Mater.* **2019**, *29*, 1808012.
[3] Y. Li, J. Krahn, C. Menon, *J. Bionic Eng.* **2016**, *13*, 181.
[4] K. Autumn, M. Sitti, Y. A. Liang, A. M. Peattie, W. R. Hansen, S. Sponberg, T. W. Kenny, R. Fearing, J. N. Israelachvili, R. J. Full, *Proc. Natl. Acad. Sci. USA* **2002**, *19*, 12252.
[5] S. Baik, Y. Park, T.-J. Lee, S. H. Bhang, C. Pang, *Nature* **2017**, *546*, 396.
[6] T. Liu, C. J. Kim, *Science* **2014**, *346*, 1096.
[7] R. Das, Z. Ahmad, J. Nauruzbayeva, H. Mishra, *Sci. Rep.* **2020**, *10*, 7934.
[8] S. Arunachalam, R. Das, J. Nauruzbayeva, E. M. Domingues, H. Mishra, *J. Colloid Interface Sci.* **2019**, *534*, 156.
[9] X. Liu, H. Gu, M. Wang, X. Du, B. Gao, A. Elbaz, L. Sun, J. Liao, P. Xiao, Z. Gu, *Adv. Mater.* **2018**, *30*, 1800103.
[10] Y. Liu, X. Li, J. Jin, J. Liu, Y. Yan, Z. Han, L. Ren, *Appl. Surf. Sci.* **2017**, *400*, 498.
[11] M. Sitti, R. S. Fearing, *J. Adhes. Sci. Technol.* **2003**, *17*, 1055.
[12] E. Arzt, S. Gorb, R. Spolenak, *Proc. Natl. Acad. Sci. USA* **2003**, *100*, 10603.
[13] S. Kim, M. Sitti, *Appl. Phys. Lett.* **2006**, *89*, 261911.
[14] A. Del Campo, C. Greiner, E. Arzt, *Langmuir* **2007**, *23*, 10235.
[15] M. P. Murphy, S. Kim, M. Sitti, *ACS Appl. Mater. Interfaces* **2009**, *1*, 849.
[16] M. P. Murphy, B. Aksak, M. Sitti, *Small* **2009**, *5*, 170.
[17] W. Bin Khaled, D. Sameoto, *Bioinspiration Biomimetics* **2013**, *8*, 044002.
[18] L. Heepe, S. N. Gorb, *Annu. Rev. Mater. Res.* **2014**, *44*, 173.
[19] N. J. Glassmaker, A. Jagota, C.-Y. Hui, W. L. Noderer, M. K. Chaudhury, *Proc. Natl. Acad. Sci. USA* **2007**, *104*, 10786.
[20] H. Gao, H. Yao, *Proc. Natl. Acad. Sci. USA* **2004**, *101*, 7851.
[21] Y. Mengüç, S. Y. Yang, S. Kim, J. A. Rogers, M. Sitti, *Adv. Funct. Mater.* **2012**, *22*, 1246.
[22] M. Zhou, Y. Tian, D. Sameoto, X. Zhang, Y. Meng, S. Wen, *ACS Appl. Mater. Interfaces* **2013**, *5*, 10137.
[23] S. Kim, E. Cheung, M. Sitti, *Langmuir* **2009**, *25*, 7196.
[24] Y. Mengüç, M. Röhrig, U. Abusomwan, H. Hölscher, M. Sitti, *J. R. Soc., Interface* **2014**, *11*, 20131205.
[25] G. J. Amador, T. Endlein, M. Sitti, *J. R. Soc., Interface* **2017**, *14*, 20170134.
[26] U. A. Abusomwan, M. Sitti, *Langmuir* **2014**, *30*, 11913.
[27] D. M. Drotlef, C. B. Dayan, M. Sitti, *Integr. Comp. Biol.* **2019**, *59*, 227.
[28] H. E. Jeong, J.-K. Lee, H. N. Kim, S. H. Moon, K. Y. Suh, *Proc. Natl. Acad. Sci. USA* **2009**, *106*, 5639.
[29] R. Helbig, J. Nickerl, C. Neinhuis, C. Werner, *PLoS One* **2011**, *6*, e25105.
[30] V. Liimatainen, D. M. Drotlef, D. Son, M. Sitti, *Adv. Mater.* **2020**, *32*, 2000497.
[31] S. Arunachalam, E. M. Domingues, R. Das, J. Nauruzbayeva, U. Buttner, A. Syed, H. Mishra, *J. Visualized Exp.* **2020**, *7*, 2001268.
[32] E. M. Domingues, S. Arunachalam, J. Nauruzbayeva, H. Mishra, *Nat. Commun.* **2018**, *9*, 3606.
[33] E. M. Domingues, S. Arunachalam, H. Mishra, *ACS Appl. Mater. Interfaces* **2017**, *9*, 21532.
[34] W. Choi, A. Tuteja, J. M. Mabry, R. E. Cohen, G. H. McKinley, *J. Colloid Interface Sci.* **2009**, *339*, 208.
[35] A. Del Campo, E. Arzt, *Macromol. Biosci.* **2007**, *7*, 118.
[36] I. Hwang, H. N. Kim, M. Seong, S. H. Lee, M. Kang, H. Yi, W. G. Bae, M. K. Kwak, H. E. Jeong, *Adv. Healthcare Mater.* **2018**, *7*, 1800275.
[37] D. W. Kim, S. Baik, H. Min, S. Chun, H. J. Lee, K. H. Kim, J. Y. Lee, C. Pang, *Adv. Funct. Mater.* **2019**, *29*, 1807614.
[38] H. Jung, M. K. Kim, J. Y. Lee, S. W. Choi, J. Kim, *Adv. Funct. Mater.* **2020**, *30*, 2070280.
[39] S. Baik, H. J. Lee, D. W. Kim, J. W. Kim, Y. Lee, C. Pang, *Adv. Mater.* **2019**, *31*, 1803309.
[40] C. Pang, J. H. Koo, A. Nguyen, J. M. Caves, M. G. Kim, A. Chortos, K. Kim, P. J. Wang, J. B. H. Tok, Z. Bao, *Adv. Mater.* **2015**, *27*, 634.
[41] D. M. Drotlef, M. Amjadi, M. Yunusa, M. Sitti, *Adv. Mater.* **2017**, *29*, 1701353.
[42] A. Mahdavi, L. Ferreira, C. Sundback, J. W. Nichol, E. P. Chan, D. J. D. Carter, C. J. Bettinger, S. Patanavanich, L. Chignozha, E. Ben-Joseph, A. Galakatos, H. Pryor, I. Pomerantseva, P. T. Masiakos, W. Faquin, A. Zumbuehl, S. Hong, J. Borenstein, J. Vacanti, R. Langer, J. M. Karp, *Proc. Natl. Acad. Sci. USA* **2008**, *105*, 2307.
[43] C. T. Mitchell, C. B. Dayan, D. M. Drotlef, M. Sitti, A. Y. Stark, *Sci. Rep.* **2020**, *10*, 19748.
[44] S. Chun, D. W. Kim, S. Baik, H. J. Lee, J. H. Lee, S. H. Bhang, C. Pang, *Adv. Funct. Mater.* **2018**, *28*, 1805224.
[45] K. Autumn, Y. A. Liang, S. T. Hsieh, W. Zesch, W. P. Chan, T. W. Kenny, R. Fearing, R. J. Full, *Nature* **2000**, *405*, 681.
[46] H. Lee, D. S. Um, Y. Lee, S. Lim, H. jun Kim, H. Ko, *Adv. Mater.* **2016**, *28*, 7457.
[47] Y. C. Chen, H. Yang, *ACS Nano* **2017**, *11*, 5332.
[48] S. Chun, W. Son, D. W. Kim, J. Lee, H. Min, H. Jung, D. Kwon, A. H. Kim, Y. J. Kim, S. K. Lim, C. Pang, C. Choi, *ACS Appl. Mater. Interfaces* **2019**, *11*, 16951.
[49] ISO Standard E. N., ISO527-2:2012, https://www.iso.org/standard/56046.html (accessed: May 2021).

ADVANCED MATERIALS

Supporting Information

for *Adv. Mater.,* DOI: 10.1002/adma.202103826

3D Printing of Elastomeric Bioinspired Complex Adhesive Microstructures

*Cem Balda Dayan, Sungwoo Chun, Nagaraj Krishna-Subbaiah, Dirk-Michael Drotlef, Mukrime Birgul Akolpoglu, and Metin Sitti**

Supporting Information

3D Printing of Elastomeric Bioinspired Complex Adhesive Microstructures

Cem Balda Dayan, Sungwoo Chun, Nagaraj Krishna-Subbaiah, Dirk-Michael Drotlef, Mukrime Birgul Akolpoglu, Metin Sitti

Liquid repellency modeling:

If a liquid is repelled by structural array (a droplet in the Cassie state), the apparent contact angle (θ^*) is defined by the Cassie-Baxter model[1] as:

$$\cos\theta^* = f_s \cos\theta_Y - f_g \quad (1)$$

where θ_Y is the intrinsic contact angle (i.e., the contact angle between a smooth solid surface and a liquid), f_s is the solid fraction that is the solid-liquid contact area (solid-liquid interface) divided by the total projected area, and f_g is the gas fraction that is the air-liquid area (air-liquid interface) divided by the total projected area. In the ideal Cassie state, the solid-liquid and air-liquid interfaces are completely flat ($f_s + f_g = 1$) and this simplifies the Equation 1 as:[2]

$$\cos\theta^* = f_s (1+\cos\theta_Y) - 1 \quad (2)$$

which explains the relation between θ^*, f_s, and θ_Y. Increase in the apparent contact angle means improving the liquid repellency. If the solid fraction decreases or the intrinsic contact angle increases, the apparent contact angle rises. If the solid fraction decreases, the effect of the intrinsic contact angle on the apparent contact angle also reduces. The impact of the material's internal wettability characteristic (related to θ_Y) on liquid repellency (related to θ^*) declines if the solid fraction decreases as shown in **Figure S9**. This means that if the solid fraction has a lower value, regardless of the material, the structured surfaces can repel extremely low surface tension liquids.[2] In terms of the structure dimensions, the solid fraction can be reduced by decreasing the tip diameter, the tip thickness, the overhang height, and the overhang thickness, in contrast to increasing the pitch distance.

Not only the solid fraction, but also the shape of the structure is important for liquid repellency and this is determined by the critical angle (θ_c). The structured surfaces can repel liquids only if the critical angle is larger than 180^0. The critical angle is the summation of the edge angle (θ_0) of the structure and the intrinsic contact angle (θ_Y) where[3]

$$\theta_c = \theta_0 + \theta_Y . \quad (3)$$

The edge angle varies if the shape of the structure changes. As an example, the edge angle of the pillar structure is 90^0. This means that the intrinsic contact angle larger than 90^0 liquids can be repelled by the pillar structures. For that reason, fully wetting liquids ($\theta_Y \sim 0^0$) cannot be repelled by the pillar structures. For the T-shaped structures, the edge angle is 180^0, which means that larger than 0^0 intrinsic contact angle liquids can be repelled in theory. This value is exactly on the critical limit for fully wetting liquids. Due to just being on the limit, any imperfection can disturb the liquid repellency property in practice. However, for double re-

entrant structures, the edge angle is 270^0. This means that even fully wetting (the intrinsic contact angle 0^0) liquids can be repelled because their edge angle is much more than the critical limit (180^0). The edge angle measurements of different structures are reported in **Figure S10**. [3]

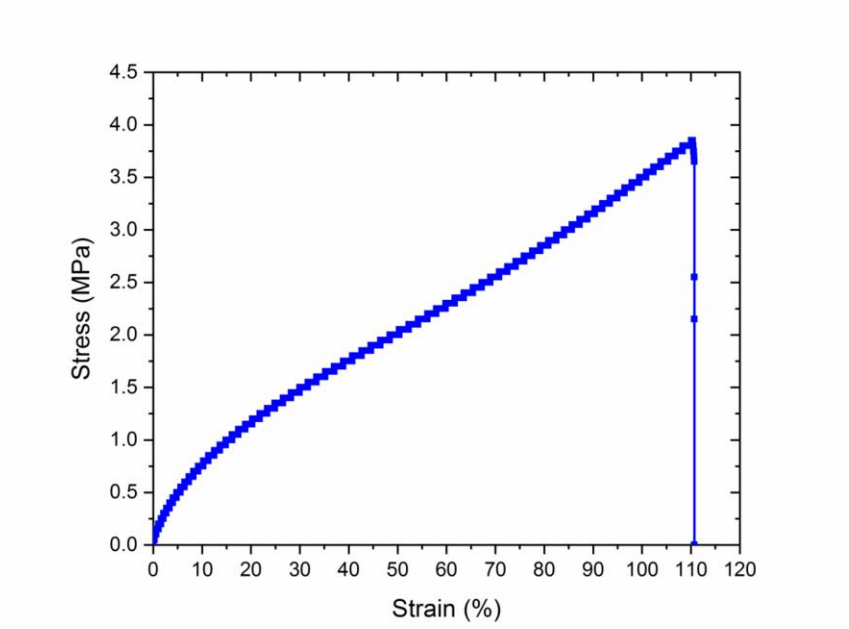

Figure S1. Stress-strain test result of the custom resin material (see Table 1 for the composition details).

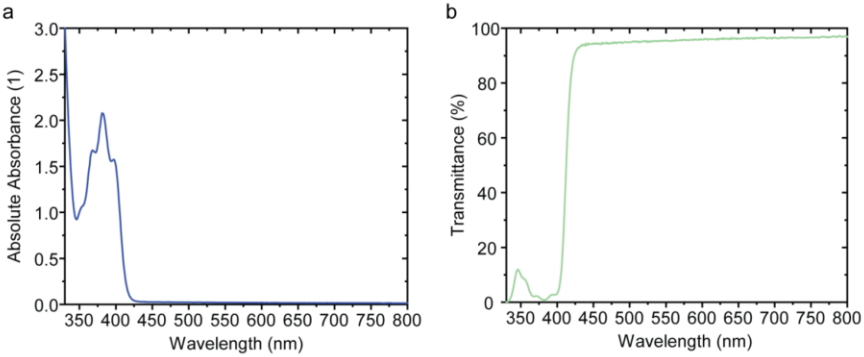

Figure S2. a) Absorbance vs. wavelength and b) transmittance vs. wavelength graphs for the custom resin.

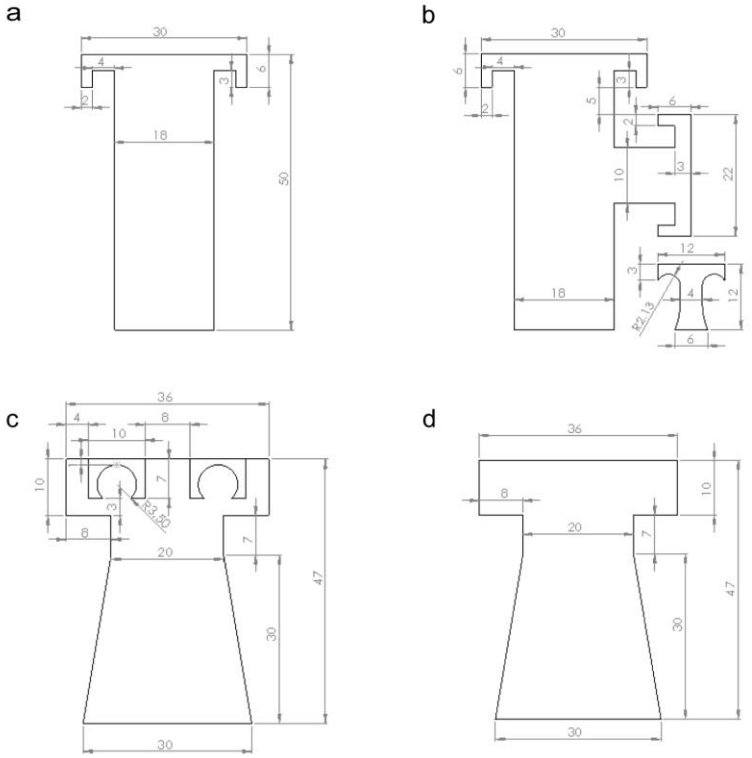

Figure S3. Dimensions of all demonstrated adhesive structures in this study: a) middle and b) side structures of the springtail-gecko-inspired array, c) the octopus-gecko-inspired and d) the gecko-inspired fibril adhesive structures.

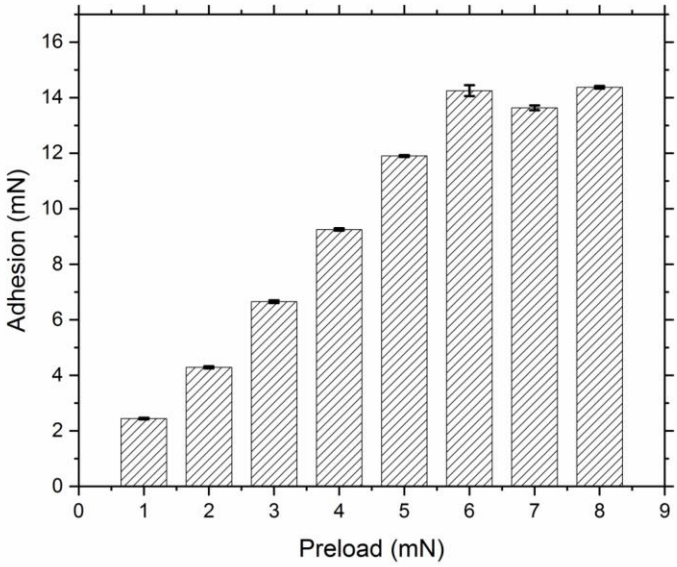

Figure S4. Saturation preload test for the double re-entrant structure adhesives on a hemispherical smooth glass indenter (approaching and retraction speed: 25 μm s^{-1}, relaxation time after preloading: 10 s). The observed saturation preload is 6 mN.

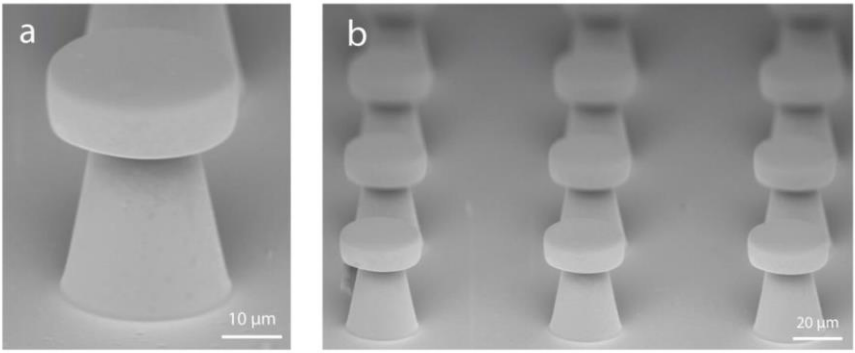

Figure S5. SEM images of the gecko-inspired fiber adhesives: a) the single fiber structure and b) the fiber array.

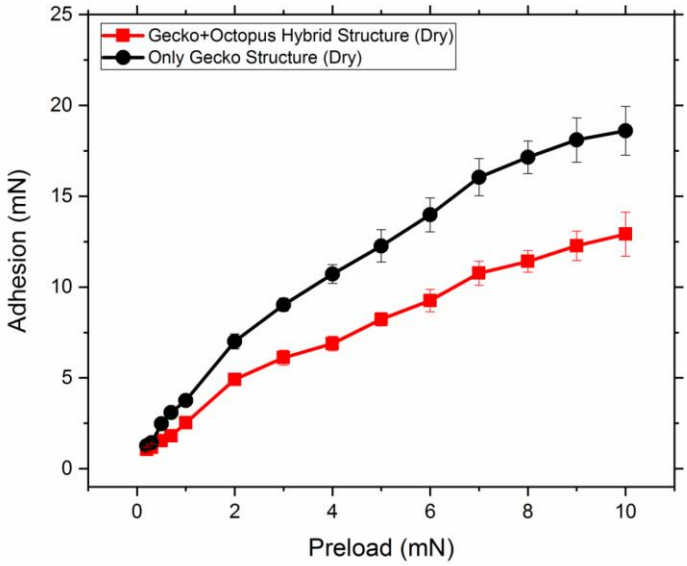

Figure S6. Dry adhesion test results of the octopus-gecko-inspired and the gecko-inspired structures under different preloads using a hemispherical smooth glass indenter.

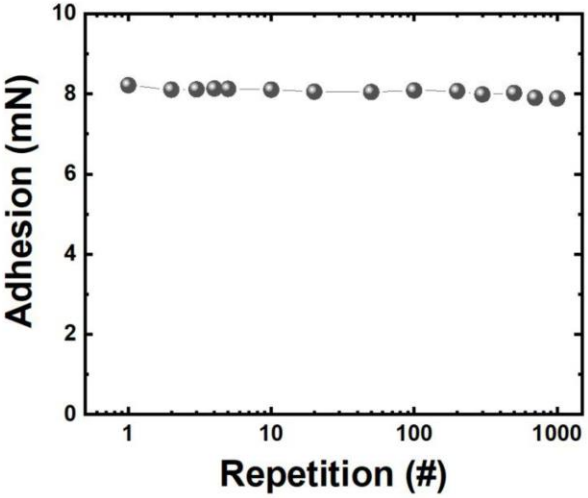

Figure S7. Reproducible adhesion performance of the hybrid octopus-gecko-inspired structures in dry conditions in more than 1,000 loading-to-unloading cycles with the preload of 5 mN, motion speed of 5 μm s^{-1}, and relaxation time of 10 s after preloading. The waiting time between each test cycle was 5 s.

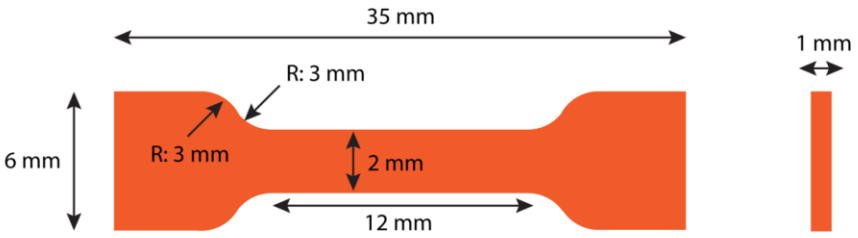

Figure S8. The specimen shape and dimensions for custom resin's mechanical characterization according to the ISO-527-2 standards.

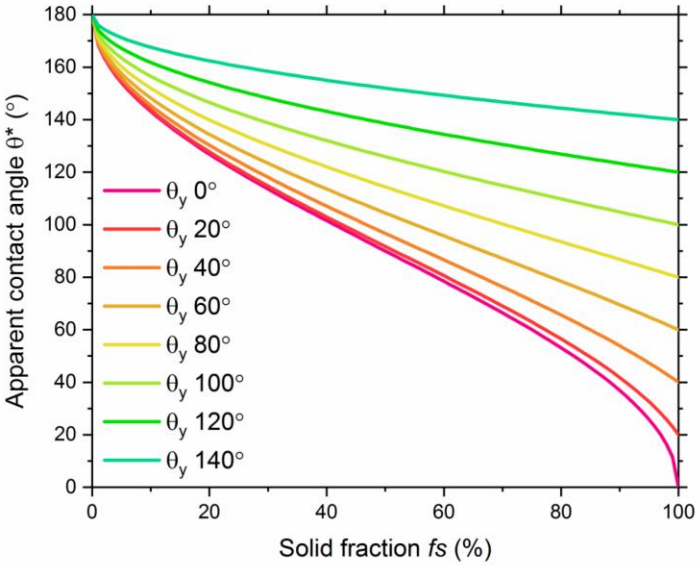

Figure S9. The effect of the solid fraction (f_s) on the apparent contact angle (θ^*) for variety of intrinsic contact angles (θ_Y). The solid fraction is determined by the structural dimensions (such as the tip diameter, the tip thickness, the overhang height, the overhang thickness, and the pitch distance).

Figure S10. The edge angle of different fibrillar structures: a) simple pillars, b) T-shaped fiber structures, and c) double re-entrant fiber structures.

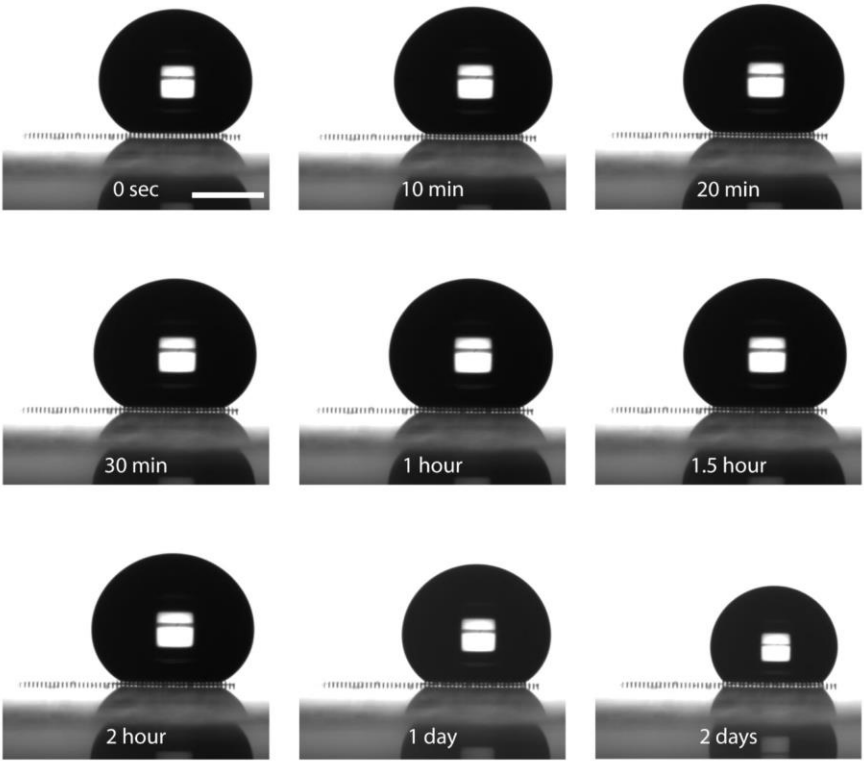

Figure S11. Liquid-repellency duration of the fabricated springtail- and gecko-inspired structures. The structures could repel a 5 µL ethylene glycol droplet for more than 2 days. After 2 days, the experiment was stopped. Scale bar: 1 mm.

References:

[1] A. Cassie, S. Baxter, *Trans. Faraday Soc.* **1944**, *40*, 546.

[2] T. Liu, C. J. Kim, *Science.* **2014**, *346*, 1096.

[3] X. Liu, H. Gu, M. Wang, X. Du, B. Gao, A. Elbaz, L. Sun, J. Liao, P. Xiao, Z. Gu, *Adv. Mater.* **2018**, *30*, DOI 10.1002/adma.201800103.

Appendix D. Machine Learning-based and Experimentally Validated Shear Optimal Fibril Adhesives

This appendix includes the following publication:

1. **Cem Balda Dayan**, Donghoon Son, Amirreza Aghakhani, Yingdan Wu, Sinan Ozgun Demir, and Metin Sitti, Machine learning-based and experimentally validated shear optimal fibril adhesives. *unpublished*, 2023.

Machine learning-based and experimentally validated shear optimal fibril adhesives

*Cem Balda Dayan, Donghoon Son, Amirreza Aghakhani, Yingdan Wu, Sinan Ozgun Demir and Metin Sitti**

C.B. Dayan, Dr. D. Son, Dr. A. Aghakhani, Dr. Wu, S.O. Demir, Prof. M. Sitti
Physical Intelligence Department, Max Planck Institute for Intelligent Systems, 70569 Stuttgart, Germany

Prof. M. Sitti
Institute for Biomedical Engineering, ETH Zürich, 8092 Zürich, Switzerland
School of Medicine and College of Engineering, Koç University, 34450 Istanbul, Turkey

*Correspondence to: sitti@is.mpg.de

Keywords. Gecko adhesives; shear; adhesive fibrils; computational design; Bayesian optimization

Abstract. Bioinspired fibrillar structures have been promising for a wide range of disruptive adhesive applications. Especially micro/nanofibrillar structures on gecko toes can have strong and controllable adhesion and shear on a wide range of surfaces with residual-free, repeatable, self-cleaning, and other unique features. Synthetic dry fibrillar adhesives inspired by such biological fibrils have been optimized in different aspects to increase their performance. Previous fibril designs for shear optimization are limited by pre-defined standard shapes in a narrow range primarily based on human intuition, which restricts their maximum performance. This study combines the Bayesian optimization and finite-element-method-based shear mechanics simulations to find shear-optimized fibril designs automatically. In addition, fabrication limitations have been integrated into the simulations to have more experimentally relevant results. The computationally discovered shear-optimized structures are fabricated, experimentally validated, and compared with the simulations. The results show that the computed shear-optimized fibrils perform better than the pre-defined standard fibril designs. This design optimization method can be used in future real-world shear-based

gripping or non-slip surface applications, such as robotic pick-and-place grippers, climbing robots, gloves, electronic devices and medical and wearable devices.

1. Introduction

Geckos have hairy micro/nanostructures on their toes to stick to diverse surfaces. These fibril adhesives have some branches and hierarchical structures called setae. Their geometry is highly complex with spatula and mushroom tip endings[1]. Such fibrillar adhesives give highly repeatable and controlled adhesion with no residual remaining on the contact surface[2]. These advantages come from the source of the adhesion, which is intermolecular interactions, such as van der Waals forces[3,4]. Such fibrillar adhesives are also investigated for their self-cleaning[5–8], contact mechanics[9,10], liquid repellency[11,12], shear[13–15] and adhesion under different environmental conditions [16]. These advantages have inspired many studies to fabricate synthetic bioinspired fibrillar adhesives for various applications[11,13,17]. In some cases, synthetic adhesives performed even better than their biological counterparts on smooth surfaces[18,19].

Many studies have investigated bioinspired non-directional vertical fibrillar adhesives with various geometries and materials[1]. Most studies have focused on maximizing the adhesion of these synthetic fibrillar adhesives using both analytical and advanced computational methods as a function of fiber stem and tip ending shape, fiber placement, spacing, and material properties. Mushroom/wedge-shaped[20], T-shaped[21–23] and three dimensionally (3D) designed[24,25] fibrils have shown the most enhanced adhesion. However, the maximized shear of these fibrils has not been investigated yet using advanced computational methods. The fibril structures should initially have high contact area and adhesion with the contact surface to obtain high shear[26]. During shear, mushroom-shaped fibrils bend after a certain critical

point and carry normal and shear stress on the tip of the fibril's circumference, and, as a result, the actual contact area decreases. It causes a reduction in shear force. Therefore, the 3D shape of the fibril stem and tip ending needs to be optimized for maximum shear.

Machine learning methods have been implemented in many different fields for optimizing the 3D design of structures in buildings[27], ships[28], aircraft[29], antennae[30], and materials[31,32]. Most of these optimizations used neural networks or genetic algorithms. However, these approaches have significant disadvantages in requiring an extensive training data set with more computational time. There are more time-effective alternatives for machine-learning-based design optimization, such as the Bayesian optimization. Moreover, these optimizations can be implemented in fibril adhesive designs as in previous studies for maximizing their adhesion[24,25]. However, no one has investigated shear-optimal 3D fibril designs using machine-learning approaches yet.

Previous studies used pre-defined limited fibril shapes to investigate their shear performance. A more general approach is needed to reduce these limitations and explore more optimal fibril shapes with higher shear performance. Therefore, we propose a machine learning-based optimization method using finite element methods (FEM)-based shear modelling to optimize the shear of 3D fibril designs. We experimentally fabricate such 3D fibril designs using two-photon polymerization (2PP) technique to validate it experimentally. This method provides the advantage of searching a vast design space relatively faster than trial-error and other optimization methods[33]. In addition, the implemented Bayesian optimization framework is highly data-efficient, and the optimization framework requires 300 iteration runs for each design to find the optimal fibril design. Moreover, the Bezier-curve-based body shape computational modelling gives high flexibility for investigating the optimal fibril design compared to standard pre-defined shapes. In each iteration, the shear results are estimated

with the FEM simulations, and the Bayesian optimizer suggests another fibril design according to the FEM-estimated results. The proposed framework saves reasonable time during shear-optimal fibril design investigation. Finally, the optimal fibril shapes are experimentally validated.

2. Results

FEM-based shear simulation and the Bayesian optimization are the two main parts of the proposed shear optimization framework (Figure 1a). FEM simulation was used for shear force estimation, and the Bayesian optimization was used for investigating the optimal estimated design. In each iteration, the Bayesian optimization suggested design parameters to evaluate the estimated shear for the simulation. This process continued until the iteration limit (300 iterations) was achieved, which gave us the optimal fibril design.

The FEM simulation was built in two dimensions (2D) for all shapes. The contact surface was assumed as smooth and locally flat. The side profile of the 3D fibril was modeled using a Bezier curve. Three different aspect ratios (1, 0.6, 0.4) and three different tip diameters (40, 60, 80) were considered to explore the fibril size effects. In addition to that, two-photon-polymerization-based 3D fibril fabrication limitation, such as the minimum achievable fillet radius of 2.7 μm at the tip of the fibrils, was integrated into the simulations.

The shear performance of a fibril was simulated with its nonlinear deformation using the Mooney-Rivlin hyperelastic model[34,35]. During the simulations, the shear force of the fibril was calculated by integrating the shear stress on the fibril tip line. After taking the line integral, the unit force was divided by the measured tip diameter of the fibril and multiplied by the tip area of the fibril. This way, we obtained the equivalent shear force from the 2D

FEM simulation. In the simulations, it was assumed that the fibril tip had contact with a smooth and locally flat surface. Initially, all the fibrils were compressed with a locally flat probe with a constant preload pressure of ~600 kPa. After compression, the fibril base was moved to the right side with small step sizes to create shear on the fibril. After reaching the preload pressure and after the shear starts, the *z*-position is kept fixed during measurements. It means that the applied normal pressure was not kept constant after shearing started, so it wasn't controlled by any feedback mechanism to keep it at the same value during measurements. During the shear, if the interfacial theoretical critical stress value [36,37] was reached on any region of the fibril's tip surface, then the simulation assumed that the fibril detached from the surface.

As an optimizer, the Bayesian optimization method was used and connected to the FEM simulation. One of the main advantages of this method was keeping the iteration number as low as possible. This optimization method could help decrease the number of simulation runs and increase our approach's efficiency. The fixed parameters were the minimum fillet radius due to the fibril fabrication limitations, the fibril tip diameter, and the fibril stem height for corresponding categories. In each iteration, the optimization framework considered the Bezier-curve control points as optimizable variables and suggested the optimal design (Figure 1b). Our method aimed to maximize the shear force. Here, all of the fibril designs were directly fabricated by a two-photon-polymerization process with an elastomeric resin material (Figure 1c, d). Before starting the optimization process, the essential parameters were experimentally measured and included in the simulations, such as the hyperelastic model parameters, the minimum fillet radius due to fabrication limitations, and the theoretical interfacial critical stress.

During shear, the interfacial stress of the optimal fibril showed that the stress distributions were changing along the fibril tip contact surface area (Figure 2). The normal stress distribution of the fibril showed that the opposite side of the shear direction of the fibril edge's interfacial stress distribution increased during shear. After reaching the critical interfacial stress, the opposite side of the shear direction of the fibril edge's interfacial stress distribution was assumed to be detached from the surface. As a result, the detachment started from the critical interfacial stress-reached part of the fibril and continued as a crack propagation to the other end of the fibril (Figures 2a-c). During shear, the interfacial shear stress distribution of the fibril also changed. The shear stress values increased along the fibril interface during shear. Especially, both ends of the fibril's interfacial stress values increased drastically (Figures 2d-f).

The optimized fibrils with various tip diameters and aspect ratios were found with the proposed optimization framework. The fibrils' three different tip diameters (40, 60, and 80 μm) were optimized for three different aspect ratios (ARs) (1, 0.6, and 0.4). All of the nine optimal fibril designs are shown in Figure 3. For high aspect ratio (AR 1) fibril designs, the stiffness of the fibrils was tried to be increased by maximizing the Bezier curve control points to obtain higher shear force.

The shear performance of the fabricated optimal fibrils was characterized by a hemispherical-smooth glass probe with a 10 mm diameter. Since the tip diameters of the fibrils were much smaller than the smooth glass probe, flat-flat contact geometry can be assumed between the fibrils and the contact probe during measurements. All 40 μm tip diameter fibril designs were printed as a tripod with three structures for measurements. The rest of the tip diameter designs (60 and 80 μm) were fabricated as a single structure. Standard shapes (flat-punch and wedge-shaped mushroom fibrils) were also fabricated and considered as a control in this study. These

structures were widely known and commonly used in the literature for high adhesion and shear.

Shear performance comparison among all possible fibril designs was shown in Figure 4 with experimental and simulation results. Machine learning-based optimal fibril designs performed better than the standard shapes in simulations and experiments in all cases. Moreover, the predicted shear forces show agreement with the experiments in all fibril designs and categories. The results show that if the fibril's tip diameter increases, the fibril's shear force also increases for a single structure. This phenomenon also applies to the aspect ratio. If the aspect ratio decreases, the fibril's shear force increases for a single fibril. This trend is related to the stiffness of the fibrils. If the stiffness of the fibril rises, then its shear performance also increases. However, there should be a limit to increasing the stiffness of the structures. If the stiffness of the made of material of the fibrils increases, then after a certain point, the conformal contact between the fibril tips and the contact surface worsens, which would reduce the shear performance.

3. Conclusion

Our approach for investigating shear-optimal fibril designs with experimental validation could compute shear-optimal fibril designs accurately and efficiently. This investigation is possible by linking the FEM shear simulation with the Bayesian optimization method instead of designing fibrils based on human intuition or analytical models. The computational machine learning approach enables us to explore a broad range of fibril designs efficiently to maximize the shear performance. Additionally, the Bezier-curve-based fibril body design gives significant flexibility to investigate broad fibril designs. Besides the simulation results, experimental results have validated the computed shear-optimal fibril designs. As a future

work, fibril designs that optimize adhesion, shear and wetting can be studied using the given computational framework. Integrated fabrication limitation in simulations makes the FEM simulation environment more realistic than other simulation approaches[25]. As a result, the computed optimal design performances matched well with the experimental ones. These findings are crucial for many real-world shear-dominated fibrillar adhesive applications in robotic grippers for pick-and-place and object manipulation[38], climbing or other mobile robots that require non-slipping limbs[39], and biomedical devices to anchor and non-slip on surfaces [40].

4. Experimental Section

FEM simulations: For FEM simulations, a commercial FEM software (COMSOL Multiphysics 5.6, COMSOL Inc.) was used. The simulations were used to estimate the shear force of the standard and optimal fibril designs. The fibril base was fixed on the substrate in the simulations, and the top part of the fibril tip ending was in touch with the contact surface. At the beginning of the simulation, the contact surface iteratively translated and compressed the fibril on the *y*-axis until reaching ~600 kPa. After that, the fibril substrate moved on the *x*-axis until the tip of the fibril's stress reached the critical interfacial normal stress. Then, the simulation terminated, and the shear force was calculated. The shear force of the fibril was calculated by integrating the shear stress on the fibril tip line, leading to unit force per length (N/m). After taking the line integral, the unit force was divided by the measured tip diameter of the fibril and multiplied by the tip area of the fibril, giving the total shear force.

For simulations, some material characterizations have been realized experimentally. Initially, all standard shapes were fabricated by the two-photon-polymerization method, and commercial IP-PDMS elastomeric resin was used as a material. The scanning electron

microscope (SEM) images were used for defining the geometrical fabrication limitation: the minimum tip edge fillet radius. For the Mooney-Rivlin two parameters, the adhesion measurements were conducted. For finding the theoretical critical stress values, shear characterizations were realized for all standard fibrils (flat-punch pillar and wedge mushroom). The shear measurements were matched with the shear simulations for all standard shapes and categories (tip diameter and aspect ratios) by minimizing the root-mean-squared relative error to find each aspect ratio's theoretical critical stress. We found that one specific theoretical critical stress exists for each aspect ratio. For aspect ratios 1, 0.6, and 0.4, the critical stresses were -264.0 kPa, -14.5 kPa, and 362.9 kPa, respectively.

The design of the fibrils includes fixed and optimizable parameters. The fixed parameters include the minimum edge fillet radius, tip diameter (for each category), aspect ratio (for each category), Mooney-Rivlin parameters, and theoretical critical stress (for each aspect ratio). The optimizable parameters include the 4^{th} degree of Bezier-curve control points with three Bezier-curve control points and a fibril base diameter. Each simulation was 2D, including more than 10,000 free triangular elements as meshes. Significantly, the meshes were extremely fine toward the tip of the fibril to catch the theoretical critical stress for detachment precisely.

Bayesian Optimization: The Bayesian optimization was implemented using a pre-built function called "bayesopt.m" on MATLAB (MATLAB R2018a, The MathWorks, Inc.). As an acquisition function, expected improvement was used. The number of iterations was set to 300. The Bayesian optimizer (implemented in MATLAB) was linked with COMSOL FEM simulation (COMSOL Multiphysics 5.6, COMSOL Inc.) via LiveLink. The Bayesian optimizer's suggested design is sent to FEM simulation in each iteration. The FEM simulation ran and calculated the estimated shear force. Afterward, the estimated shear force is returned

to the Bayesian optimizer to decide which design point should be evaluated next. All process takes approximately 5 hours to find the optimal design for one specific tip diameter and aspect ratio. This framework is implemented on a desktop computer that has Intel Xeon CPU with 20 cores (E5-2680 v2, 2.80 GHz), 192 GB RAM, and NVIDIA Quadro K5000 graphics card.

Fibril Fabrication: For each standard and optimal fibril design, the computer-aided design was implemented by Solidworks, and then a stereolithography file (.stl) was created. The generated files were uploaded into the Nanoscribe software (Photonic Professional GT2, Nanoscribe GmbH, Germany). The two-photon lithography system was used in DiLL mode. In this mode, the elastomeric resin material (IP-PDMS, Nanoscribe GmbH, Germany) was placed between the substrate glass and the objective. As the objective lens, 25x, 0.8 NA objective was used. After the printing of desired fibril structures, the post-process was applied. The fabricated fibrils were immersed in a beaker containing isopropanol alcohol (IPA) for 15 min. Next, the samples were immersed in another beaker containing fresh IPA for 2 min. Young's modulus of the material was 15.3 MPa. For material behavior on a small scale, a T-shape fibril's stress-strain curve on a smooth spherical glass was used for Mooney-Rivlin's second-order model fitting. The computed Mooney-Rivlin second-order model fitting parameters were used in all simulations. These values were C10 = 1.01e+6 Pa and C01 = 5.96e+5 Pa.

Shear and Adhesion Measurements: A custom-made shear-adhesion setup was used for tangential/shear and normal force measurements. A video camera (Grasshopper3, Point Grey Research Inc.) was mounted on an inverted optical microscope (Axio Observer A1, Zeiss) to visualize the measurements. For z-direction and y-direction, a computer-controlled high-precision stage (LPS-65 2", Physik Instrumente GmbH & Co. KG) was attached to the microscope. Two load cells (y-axis: LSB200, 100g, JR S-Beam, FUTEK, and z-axis: GSO-25,

Transducer Technique LLC) were mounted on the stage in an orientation to measure the forces on the *y*-axis and *z*-axis. The motion of the piezo stages was controlled, and a custom-made program processed the data acquisition by a LabVIEW (National Instruments, Austin, TX, USA). A smooth spherical glass probe with a 10 mm diameter was used as a contact surface. The load-drag tests were done for shear. Before applying shear, the normal pressure (~600 kPa) was exerted on the fibril. After reaching the desired preload, 60 seconds of relaxation time waited. Tangential displacement was applied for 1 mm after relaxation time. During the measurements, all speeds (approaching speed on the *z*-axis, shear speed on the *y*-axis, and retraction speed on the *z*-axis) were set to 5 $\mu m\ s^{-1}$. Each measurement was repeated five times.

Supporting Information

Supporting Information is available from the Wiley Online Library or from the author.

Acknowledgements

This work was funded by the Max Planck Society. The authors thank the International Max Planck Research School for Intelligent Systems (IMPRS-IS) for supporting C.B.D.

Received: ((will be filled in by the editorial staff))
Revised: ((will be filled in by the editorial staff))
Published online: ((will be filled in by the editorial staff))

References

[1] R. D. O'Rorke, T. W. J. Steele, H. K. Taylor, *J. Adhes. Sci. Technol.* **2016**, *30*, 362.

[2] R. Ruibal, V. Ernst, *J. Morphol.* **1965**, *117*, 271.

[3] K. Autumn, M. Sitti, Y. A. Liang, A. M. Peattie, W. R. Hansen, S. Sponberg, T. W. Kenny, R. Fearing, J. N. Israelachvili, R. J. Full, *Proc. Natl. Acad. Sci. U. S. A.* **2002**, *99*, 12252.

[4] K. Autumn, Y. A. Liang, S. T. Hsieh, W. Zesch, W. P. Chan, T. W. Kenny, R. Fearing, R. J. Full, *Nature* **2000**, *405*, 681.

[5] S. Kim, E. Cheung, M. Sitti, *Langmuir* **2009**, *25*, 7196.

[6] Y. Mengüç, M. Röhrig, U. Abusomwan, H. Hölscher, M. Sitti, *J. R. Soc. Interface* **2014**, *11*, 20131205.

[7] G. J. Amador, T. Endlein, M. Sitti, *J. R. Soc. Interface* **2017**, *14*, 20170134.

[8] U. A. Abusomwan, M. Sitti, *Langmuir* **2014**, *30*, 11913.

[9] N. J. Glassmaker, A. Jagota, C. Y. Hui, W. L. Noderer, M. K. Chaudhury, *Proc. Natl. Acad. Sci. U. S. A.* **2007**, *104*, 10786.

[10] H. Gao, H. Yao, *Proc. Natl. Acad. Sci. U. S. A.* **2004**, *101*, 7851.

[11] C. B. Dayan, S. Chun, N. Krishna-Subbaiah, D. M. Drotlef, M. B. Akolpoglu, M. Sitti, *Adv. Mater.* **2021**, *33*, 31.

[12] V. Liimatainen, D. M. Drotlef, D. Son, M. Sitti, *Adv. Mater.* **2020**, *32*, 2000497.

[13] M. P. Murphy, B. Aksak, M. Sitti, *Small* **2009**, *5*, 170.

[14] Y. Mengüç, S. Y. Yang, S. Kim, J. A. Rogers, M. Sitti, *Adv. Funct. Mater.* **2012**, *22*, 1246.

[15] M. Zhou, Y. Tian, D. Sameoto, X. Zhang, Y. Meng, S. Wen, *ACS Appl. Mater. Interfaces* **2013**, *5*, 10137.

[16] C. T. Mitchell, C. B. Dayan, D. M. Drotlef, M. Sitti, A. Y. Stark, *Sci. Rep.* **2020**, *10*, 1.

[17] M. P. Murphy, S. Kim, M. Sitti, *ACS Appl. Mater. Interfaces* **2009**, *1*, 849.

[18] D.-M. Drotlef, C. B. Dayan, M. Sitti, *Integr. Comp. Biol.* **2019**, *59*, 227.

[19] H. E. Jeong, J.-K. Lee, H. N. Kim, S. H. Moon, K. Y. Suh, *Proc. Natl. Acad. Sci.* **2009**, *106*, 5639.

[20] B. Aksak, K. Sahin, M. Sitti, *Beilstein J. Nanotechnol.* **2014**, *5*, 630.

[21] G. Carbone, E. Pierro, *Small* **2012**, *8*, 1449.

[22] R. G. Balijepalli, M. R. Begley, N. A. Fleck, R. M. McMeeking, E. Arzt, *Int. J. Solids Struct.* **2016**, *85–86*, 160.

[23] G. Carbone, E. Pierro, S. N. Gorb, *Soft Matter* **2011**, *7*, 5545.

[24] D. Son, V. Liimatainen, M. Sitti, *Small* **2021**, *17*, 2102867.

[25] Y. Kim, C. Yang, Y. Kim, G. X. Gu, S. Ryu, *ACS Appl. Mater. Interfaces* **2020**, *12*, 24458.

[26] M. Piccardo, A. Chateauminois, C. Fretigny, N. M. Pugno, M. Sitti, *J. R. Soc. Interface* **2013**, *10*, 20130182.

[27] P. Geyer, S. Singaravel, *Appl. Energy* **2018**, *228*, 1439.

[28] H. Cui, O. Turan, P. Sayer, *CAD Comput. Aided Des.* **2012**, *44*, 186.

[29] O. Hennigh, in *6th Int. Conf. Learn Represent ICLR 2018 - Work. Track Proc*, **2018**, pp. 1–12.

[30] D. Linden, G. Hornby, A. Globus, *Am. Inst. Aeronaut. Astronaut. Reston, VA* **2006**, 7242.

[31] N. O. Dogan, U. Bozuyuk, P. Erkoc, A. C. Karacakol, A. Cingoz, F. Seker-Polat, M. A. Nazeer, M. Sitti, T. Bagci-Onder, S. Kizilel, *Adv. NanoBiomed Res.* **2022**, *2*, 2100033.

[32] G. Dogan, S. O. Demir, R. Gutzler, H. Gruhn, C. B. Dayan, U. T. Sanli, C. Silber, U. Culha, M. Sitti, G. Schütz, C. Grévent, K. Keskinbora, *ACS Appl. Mater. Interfaces* **2021**, *13*, 54503.

[33] C. B. Dayan, F. Afghah, B. S. Okan, M. Yıldız, Y. Menceloglu, M. Culha, B. Koc, *Mater. Des.* **2018**, *148*, 87.

[34] M. Mooney, *J. Appl. Phys.* **1940**, *11*, 582.

[35] R. S. Rivlin, *Philos. Trans. R. Soc. A* **1948**, *241*, 379.

[36] B. Aksak, C. Y. Hui, M. Sitti, *J. R. Soc. Interface* **2011**, *8*, 1166.

[37] T. Tang, C. Y. Hui, N. J. Glassmaker, *J. R. Soc. Interface* **2005**, *2*, 505.

[38] A. Koivikko, D.-M. Drotlef, C. B. Dayan, V. Sariola, M. Sitti, *Adv. Intell. Syst.* **2021**, *3*, 2100034.

[39] D. Son, H. Gilbert, M. Sitti, *Soft Robot.* **2020**, *7*, 10.

[40] J. Klein, *Polym. Adv. Technol.* **2012**, *23*, 729.

Figures

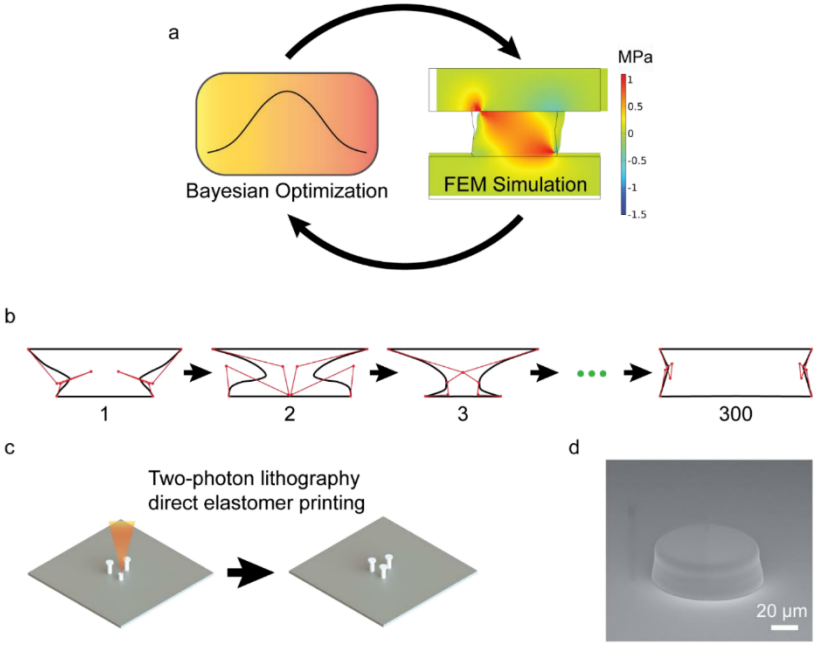

Figure 1. Overall summary for investigating the Bayesian optimization-based friction/shear-optimized microfibril designs. a) Optimization framework for investigating the machine learning-based (ML-based) optimal microfibril designs. b) Starting from a random shape, the fibril design changes in each iteration until obtaining the maximum shear force. c) Fabrication procedure of the optimal fibrils using two-photon lithography technique using an elastomeric resin material. d) Scanning electron microscope (SEM) image of a sample fabricated optimal microfibril with a 80 µm tip diameter and 0.4 aspect ratio.

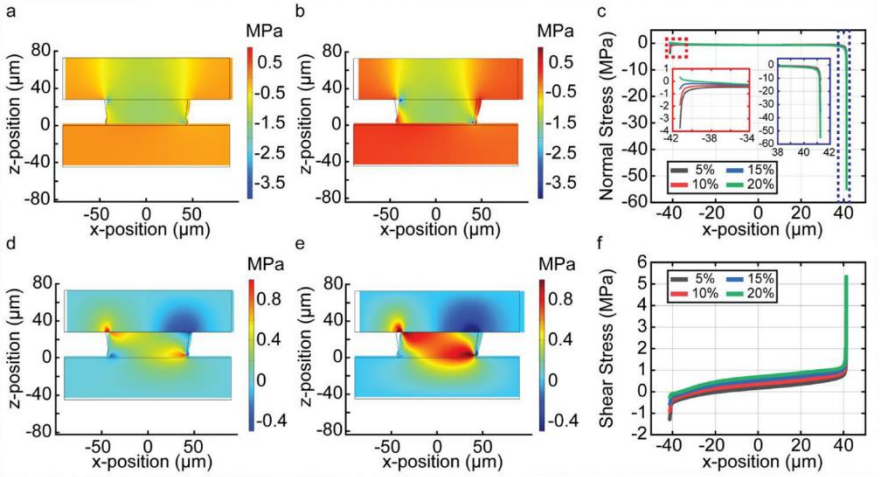

Figure 2. Normal and shear stress distribution under different shear strains for a 80 μm tip diameter and aspect ratio 0.4 ML-found optimal design. Normal stress distribution a) under 10% shear strain, b) under 20% shear strain, c) on a tip-contact surface interface for four different shear strains (5%, 10%, 15%, 20%) for 80 μm tip diameter and aspect ratio 0.4 ML-found optimal design are shown, respectively. Shear stress distribution d) under 10% shear strain, e) under 20% shear strain, f) on a tip-contact surface interface for four different shear strains (5%, 10%, 15%, 20%) for 80 μm tip diameter and aspect ratio 0.4 ML-found optimal design are shown, respectively.

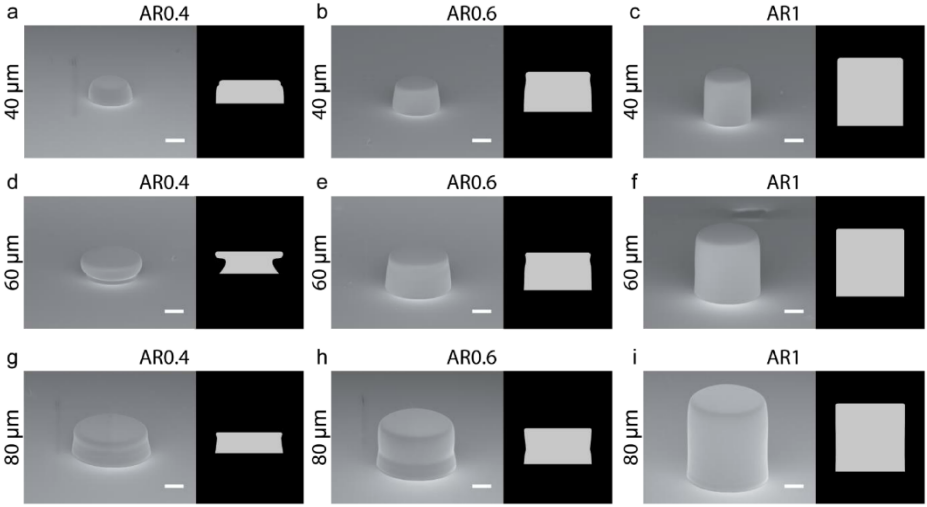

Figure 3. SEM images of the fabricated ML-found optimal elastomeric fibril structures for three different tip diameters (40 µm, 60 µm, and 80 µm) and three different aspect ratios (ARs) (0.4, 0.6, and 1). The tip diameter 40 µm, 60 µm, and 80 µm designs are [a), b) and c)], [d), e) and f)], [g), h), and i)], respectively. The aspect ratio 0.4, 0.6, and 1 designs are [a), d) and g)], [b), e) and h)], [c), f), and i)], respectively. All scale bars are 20 µm.

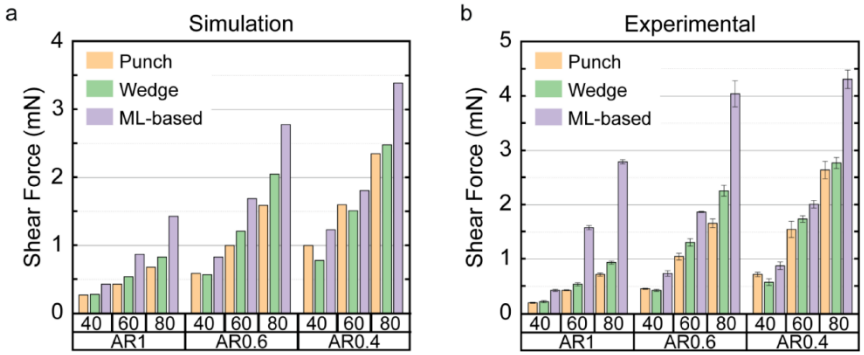

Figure 4. Shear results in FEM simulations and experiments for a single fibril using a flat punch, wedge-shaped, and ML-based optimal designs. a) The FEM simulation results show that ML-based optimal designs have better shear performance than the standard flat punch and wedge-shaped fibril designs. b) The experimental results agree with the FEM simulation results, proving that the ML-found designs give higher shear/friction forces than the standard shapes in all cases.

References

[1] J. B. Puthoff, M. S. Prowse, M. Wilkinson, K. Autumn, *J. Exp. Biol.* **2010**, *213*, 3699.

[2] M. S. Prowse, M. Wilkinson, J. B. Puthoff, G. Mayer, K. Autumn, *Acta Biomater.* **2011**, *7*, 733.

[3] A. Koivikko, D.-M. Drotlef, C. B. Dayan, V. Sariola, M. Sitti, *Adv. Intell. Syst.* **2021**, *3*, 2100034.

[4] M. P. Murphy, M. Sitti, *IEEE/ASME Trans. Mechatronics* **2007**, *12*, 330.

[5] N. M. Pugno, *Nano Today* **2008**, *3*, 35.

[6] T. Kim, J. Park, J. Sohn, D. Cho, S. Jeon, *ACS Nano* **2016**, *10*, 4770.

[7] D. M. Drotlef, M. Amjadi, M. Yunusa, M. Sitti, *Adv. Mater.* **2017**, *29*, 1.

[8] R. D. O'Rorke, T. W. J. Steele, H. K. Taylor, *J. Adhes. Sci. Technol.* **2016**, *30*, 362.

[9] K. Autumn, Y. A. Liang, S. T. Hsieh, W. Zesch, W. P. Chan, T. W. Kenny, R. Fearing, R. J. Full, *Nature* **2000**, *405*, 681.

[10] K. Autumn, M. Sitti, Y. A. Liang, A. M. Peattie, W. R. Hansen, S. Sponberg, T. W. Kenny, R. Fearing, J. N. Israelachvili, R. J. Full, *Proc. Natl. Acad. Sci. U. S. A.* **2002**, *99*, 12252.

[11] R. Ruibal, V. Ernst, *J. Morphol.* **1965**, *117*, 271.

[12] S. Kim, E. Cheung, M. Sitti, *Langmuir* **2009**, *25*, 7196.

[13] Y. Mengüç, M. Röhrig, U. Abusomwan, H. Hölscher, M. Sitti, *J. R. Soc. Interface* **2014**, *11*, 20131205.

[14] G. J. Amador, T. Endlein, M. Sitti, *J. R. Soc. Interface* **2017**, *14*, 20170134.

[15] U. A. Abusomwan, M. Sitti, *Langmuir* **2014**, *30*, 11913.

[16] N. J. Glassmaker, A. Jagota, C. Y. Hui, W. L. Noderer, M. K. Chaudhury, *Proc. Natl. Acad. Sci. U. S. A.* **2007**, *104*, 10786.

[17] H. Gao, H. Yao, *Proc. Natl. Acad. Sci. U. S. A.* **2004**, *101*, 7851.

[18] C. B. Dayan, S. Chun, N. Krishna-Subbaiah, D. M. Drotlef, M. B. Akolpoglu, M. Sitti, *Adv. Mater.* **2021**, *33*, 31.

[19] V. Liimatainen, D. M. Drotlef, D. Son, M. Sitti, *Adv. Mater.* **2020**, *32*, 1.

[20] M. P. Murphy, B. Aksak, M. Sitti, *Small* **2009**, *5*, 170.

[21] Y. Mengüç, S. Y. Yang, S. Kim, J. A. Rogers, M. Sitti, *Adv. Funct. Mater.* **2012**, *22*, 1246.

[22] M. Zhou, Y. Tian, D. Sameoto, X. Zhang, Y. Meng, S. Wen, *ACS Appl. Mater. Interfaces* **2013**, *5*, 10137.

[23] C. T. Mitchell, C. B. Dayan, D. M. Drotlef, M. Sitti, A. Y. Stark, *Sci. Rep.* **2020**, *10*, 1.

[24] M. P. Murphy, S. Kim, M. Sitti, *ACS Appl. Mater. Interfaces* **2009**, *1*, 849.

[25] D. M. Drotlef, C. B. Dayan, M. Sitti, *Integr. Comp. Biol.* **2019**, *59*, 227.

[26] H. E. Jeong, J.-K. Lee, H. N. Kim, S. H. Moon, K. Y. Suh, *Proc. Natl. Acad. Sci.* **2009**, *106*, 5639.

[27] H. Shahsavan, B. Zhao, *Macromolecules* **2014**, *47*, 353.

[28] H. K. Minsky, K. T. Turner, *Appl. Phys. Lett.* **2015**, *106*, 201604.

[29] S. C. L. Fischer, E. Arzt, R. Hensel, *ACS Appl. Mater. Interfaces* **2017**, *9*, 1036.

[30] S. Gorumlu, B. Aksak, *R. Soc. Open Sci.* **2017**, *4*, 161105.

[31] G. Huber, H. Mantz, R. Spolenak, K. Mecke, K. Jacobs, S. N. Gorb, E. Arzt, *Proc. Natl. Acad. Sci. U. S. A.* **2005**, *102*, 16293.

[32] W. Sun, P. Neuzil, T. S. Kustandi, S. Oh, V. D. Samper, *Biophys. J.* **2005**, *89*, L14.

[33] T. W. Kim, B. Bhushan, *J. R. Soc. Interface* **2008**, *5*, 319.

[34] A. M. Bauer, D. A. Good, *J. Zool.* **1996**, *238*, 635.

[35] B. E. R. Pianka, L. J. Vitt, *Can. Field-Naturalist* **2004**, 141.

[36] T. Lamb, A. M. Bauer, *Proc. R. Soc. B Biol. Sci.* **2006**, *273*, 855.

[37] T. Gamble, E. Greenbaum, T. R. Jackman, A. P. Russell, A. M. Bauer, *PLoS One* **2012**, *7*, e39429.

[38] C. E. Collins, A. P. Russell, T. E. Higham, *Funct. Ecol.* **2015**, *29*, 66.

[39] J. N. Israelachvili, D. Tabor, *Nat. Phys. Sci.* **1972**, *236*, 106.

[40] P. H. Niewiarowski, S. Lopez, L. Ge, E. Hagan, A. Dhinojwala, *PLoS One* **2008**, *3*, 1.

[41] P. Y. Hsu, L. Ge, X. Li, A. Y. Stark, C. Wesdemiotis, P. H. Niewiarowski, A. Dhinojwala, *J. R. Soc. Interface* **2012**, *9*, 657.

[42] D. Jain, A. Y. Stark, P. H. Niewiarowski, T. Miyoshi, A. Dhinojwala, *Sci. Rep.* **2015**, *5*, 1.

[43] L. Alibardi, *J. Morphol.* **2012**, *273*, 1272.

[44] L. Alibardi, *J. Exp. Zool. Part A Ecol. Genet. Physiol.* **2013**, *319*, 166.

[45] A. Y. Stark, C. T. Mitchell, *Integr. Comp. Biol.* **2019**, *59*, 214.

[46] Z. Peng, Y. Yang, S. Chen, *J. Phys. D. Appl. Phys.* **2017**, *50*, 315402.

[47] B. Aksak, K. Sahin, M. Sitti, *Beilstein J. Nanotechnol.* **2014**, *5*, 630.

[48] G. Carbone, E. Pierro, *Small* **2012**, *8*, 1449.

[49] R. G. Balijepalli, M. R. Begley, N. A. Fleck, R. M. McMeeking, E. Arzt, *Int. J. Solids Struct.* **2016**, *85–86*, 160.

[50] G. Carbone, E. Pierro, S. N. Gorb, *Soft Matter* **2011**, *7*, 5545.

[51] D. Son, V. Liimatainen, M. Sitti, *Small* **2021**, *17*, 2102867.

[52] Y. Kim, C. Yang, Y. Kim, G. X. Gu, S. Ryu, *ACS Appl. Mater. Interfaces* **2020**, *12*, 24458.

[53] M. Piccardo, A. Chateauminois, C. Fretigny, N. M. Pugno, M. Sitti, *J. R. Soc. Interface* **2013**, *10*, 20130182.

[54] P. Geyer, S. Singaravel, *Appl. Energy* **2018**, *228*, 1439.

[55] H. Cui, O. Turan, P. Sayer, *CAD Comput. Aided Des.* **2012**, *44*, 186.

[56] O. Hennigh, in *6th Int. Conf. Learn Represent ICLR 2018 - Work. Track Proc*, **2018**, pp. 1–12.

[57] D. Linden, G. Hornby, A. Globus, *Am. Inst. Aeronaut. Astronaut. Reston, VA* **2006**, 7242.

[58] N. O. Dogan, U. Bozuyuk, P. Erkoc, A. C. Karacakol, A. Cingoz, F. Seker-Polat, M. A. Nazeer, M. Sitti, T. Bagci-Onder, S. Kizilel, *Adv. NanoBiomed Res.* **2022**, *2*, 2100033.

[59] G. Dogan, S. O. Demir, R. Gutzler, H. Gruhn, C. B. Dayan, U. T. Sanli, C. Silber, U. Culha, M. Sitti, G. Schütz, C. Grévent, K. Keskinbora, *ACS Appl. Mater. Interfaces* **2021**, *13*, 54503.

[60] C. E. Rasmussen, C. K. I. Williams, *Lect. notes Comput. Sci.* **2004**, *3176*, 63.

[61] J. Mockus, V. Tiesis, A. Zilinskas, *Towar. Glob. Optim.* **1978**, *2*, 117.

[62] B. Shahriari, K. Swersky, Z. Wang, R. P. Adams, N. De Freitas, *Proc. IEEE* **2016**, *104*, 148.

[63] C. B. Dayan, F. Afghah, B. S. Okan, M. Yıldız, Y. Menceloglu, M. Culha, B. Koc, *Mater. Des.* **2018**, *148*, 87.

[64] J. Y. Chung, M. K. Chaudhury, *J. Adhes.* **2005**, *81*, 1119.

[65] M. Mooney, *J. Appl. Phys.* **1940**, *11*, 582.

[66] R. S. Rivlin, *Philos. Trans. R. Soc. A* **1948**, *241*, 379.

[67] B. Aksak, C. Y. Hui, M. Sitti, *J. R. Soc. Interface* **2011**, *8*, 1166.

[68] T. Tang, C. Y. Hui, N. J. Glassmaker, *J. R. Soc. Interface* **2005**, *2*, 505.